Universidade de Évora - Escola de Ciências e Tecnologia

Mestrado em Química

Dissertação

Structural study of aqueous solutions of amphiphilic ionic liquids capable of forming hydrogels - a contribution to understanding gelation mechanisms.

Meerab

Orientador(es) | Luís Filipe Martins

Évora 2025

Universidade de Évora - Escola de Ciências e Tecnologia

Mestrado em Química

Dissertação

Structural study of aqueous solutions of amphiphilic ionic liquids capable of forming hydrogels - a contribution to understanding gelation mechanisms.

Meerab

Orientador(es) | Luís Filipe Martins

Évora 2025

A dissertação foi objeto de apreciação e discussão pública pelo seguinte júri nomeado pelo Diretor da Escola de Ciências e Tecnologia:

Presidente	|	Isabel Pestana da Paixão Cansado (Universidade de Évora)
Vogais	|	Alfredo Jorge Palace Carvalho (Universidade de Évora) (Arguente) Luís Filipe Martins (Universidade de Évora) (Orientador)

Évora 2025

Acknowledgment

First and foremost, I thank God for granting me the strength, wisdom, and perseverance to reach this important stage of my life.

I owe my deepest gratitude to my beloved family, whose love and support have been the foundation of my journey. My heartfelt thanks go to my parents, Shazia Ashfaq and Ashfaq Ahmed, for their unconditional love, sacrifices, and constant encouragement. Their faith in me has always been my greatest motivation. I am equally thankful to my dear siblings — Aleena Mohad and her husband Mohad Gillani, Shahab Ahmed, and Fatima Ashfaq — for their endless love, prayers, and inspiration. Their belief in me has given me the courage to overcome challenges and stay focused on my goals.

I would like to express my sincere appreciation to my supervisor, Professor Luís Filipe Guerreiro Martins, for his continuous guidance, patience, and invaluable advice throughout my studies and during the completion of this thesis. His expertise, encouragement, and thoughtful insights have greatly contributed to my academic development and to the success of this research.

I am also deeply grateful to the Department of Chemistry, School of Science and Technology, University of Évora, for providing me with an excellent learning environment and the opportunity to grow both academically and personally. My special thanks go to all the professors and staff of the Chemistry Master's program for their dedication, knowledge, and kindness, which have inspired me throughout my studies.

To all of you — thank you sincerely for your guidance, encouragement, and belief in me.

Abstract

In this work, a detailed investigation was performed on the structural and aggregation behavior of a series of aqueous solutions of 1-decyl-3-methyl alkylimidazolium salts with the capability of forming gels. The study contains experimental and molecular simulation approaches to explain the self-assembly, microscopic structure, and rheological behavior of these ionic systems.

Dynamic light scattering (DLS) experiments were conducted at various concentrations to determine the hydrodynamic diameters, aggregation numbers, and size distributions of the micellar and pre-micellar structures. Molecular dynamics simulations were carried out to obtain molecular insights on the macroscopic behaviour observed in experimental determinations.

In addition to the solution behavior, the rheological properties of the gel phase of one the systems studied were examined in detail.

Overall, this work provides an integrated understanding of the structure–property relationships of alkylimidazolium-based ionic liquids, highlighting how subtle variations in molecular architecture and counter-anion identity dictate aggregation, phase behavior, and rheology.

Resumo

Estudo estrutural de soluções aquosas de líquidos iónicos anfifílicos capazes de formar hidrogéis – uma contribuição para a compreensão dos mecanismos de gelificação

Neste trabalho, foi realizada uma investigação detalhada sobre o comportamento estrutural e de agregação de soluções aquosas de sais de 1-decil-3-metil alquilimidazólio com capacidade de formar géis. A abordagem é simultaneamente experimental e de simulação molecular, para explicar a agregação, a estrutura microscópica e o comportamento reológico desses sistemas.

Foram realizadas experiências de espalhamento dinâmico de luz (DLS) em várias concentrações para determinar diâmetros hidrodinâmicos, números de agregação e distribuições de tamanho das estruturas supramoleculares. Recorreu-se a simulações de dinâmica molecular para estudar os detalhes moleculares sobre o comportamento macroscópico observado nas determinações experimentais.

As propriedades reológicas da fase gel de um dos sistemas estudados foram também examinadas em detalhe.

Este trabalho tenta contribuir para o conhecimento integrado das relações estrutura-propriedade dos líquidos iónicos à base de alquilimidazólio, destacando como variações subtis na arquitetura molecular e na identidade do anião determinam a agregação, o comportamento de fase e a reologia.

Table of Contents

Table of Contents for Figure

Contents for Tables

Abbreviations

IL	Ionic Liquid
RTILs	Room Temperature Ionic Liquids
C_{10}mimCl	1-decyl-3-methylimidazolium chloride
C_{10}mimBr	1-decyl-3-methylimidazolium bromide
C_8mimCl	1-octyl-3-methyimidazolium chloride
C_8mimBr	1-octyl-3-methyimidazolium bromide
C_{12}mimCl	1-dodecyl-3-methyimidazolium chloride
C_{10}mimNO_3	1-decyl-3-methyimidazolium nitrate
PILS	Protic Ionic Liquids
APILs	Aprotic Ionic Liquids
DLS	Dynamic Light Scattering
MD	Molecular Dynamics
CMC	Critical Micelle Concentration
NMR	Nuclear Magnetic Resonance
ATR-FTIR	Attenuated Total Reflectance – Fourier Transform Infrared Spectroscopy
k	Boltzman Constant
R_H	Hydrodynamic Radius
D_i	Diffusion coefficient of the particles
η	Solvent Viscosity
ε_{ii}, ε_{jj} σ_{ii}, σ_{jj}	Energy and the diameter between atoms of the same type

GROMACS	Groningen Machine for Chemical Simulations
PDI	Polydispersity Index
ω	Omega for Frequency
x_{IL}	Mole fraction of Ionic Liquid
γ	Shear strain
n	Shear-thinning character
RDF	Radial Distribution Function
HAR	Hydrogen Attached with Ring
VOCs	Volatile Organic Compounds

1. Introduction

Ionic liquids (ILs) are, by definition, salts that are made up of ions showing melting points below 100^0C. The utilization of such kind of liquids in physical, chemical and biological systems made a lot of progress in variety of fields granting to ILs a broad range of applications in chemistry, chemical engineering, biochemistry, materials science and environmental chemistry. ILs show a great diversity in their structure and properties, because they can be obtained using different classes of cations like those based on imidazolium, ammonium, phosphonium, pyrolidinium, pyridinium structures and anions like halides, tetrafluoroborate, acetates, carboxylates and hexafluorophosphates. ILs caught the attention of scientists because of their excellent characteristics such as their ability to dissolve in organic and inorganic substances, strong polarity, weak coordination, simultaneous hydrophilicity and hydrophobicity, extremely low vapour pressure and excellent thermal and electrochemical stability. Because of their broad range of properties, ILs are used in reaction media, as formulation components in drug delivery systems, as green solvents in a variety of applications, as electrolytes in batteries, in gas separation, carbon dioxide capture, liquid-liquid chromatography and in many other fields [1].

1.1. History of ILs

Paul Walden was the first person who introduced the designation of ionic liquid named for ethylammonium nitrate in 1914, far from being able to anticipate the importance of this area in the future. Since then, hundreds of thousands of different ionic liquids have been obtained and studied over the last decades. According to the Scopus, almost 27000 papers have been published during the last 5 years in which the term ionic liquids were mentioned. It means that every year a great number of papers has been published which indicates ionic liquids necessity in future [2].

1.2. Types of IL

ILs are usually categorized based on their chemical structure. The structural properties of ionic liquids show resemblance with the molecular liquids, ionic surfactants, molten salts, and ionic crystals. Considering the diversity of cations, anions and functional groups possibly attached to both ions, classifying ILs can be a little bit difficult task. For instance, if the donating and non-donating proton ability ILs is considered, they can be classified as protic and aprotic ILs [3].

Protic ionic liquids (PILs) are in general obtained by hydrogen ion exchange within the stoichiometric equivalent amounts of a blend of a Bronsted acid and base. Making such types of ILs is easy because no

side products are obtained in their formation, reducing their cost of formation. Proton donation is a process that attains equilibrium very quickly and based on it PILs prepared are free from impurities being, as long as the acid-base reaction is extensive, chemically pure. Hydrogen ion transfer in PILs influences their properties of volatility, heat resistance, catalysis strength, charge mobility, biomolecule stabilization and its explosive potential [3].

The structural properties of aprotic ionic liquids (APILs) are different from PILs. They have non-transferable protons. APILs are more costly than PILs because their preparation requires many steps in a sophisticated framework involving the breakdown and the formation of covalent bonds. In general APILs have more resistance and stability than the PILs [3].

Various other groups of ILs have been described in the literature depending on their different chemical composition, structure and geometric configuration such as chiral ILs (with a chiral center), magnetic ILs (containing paramagnetic atoms or groups), divalent ILs, polymeric ILs and fluorous ILs, etc. With these various varieties of ILs, scientists have different fields for future research work and development [3].

Ionic liquids whose melting point is below the room temperature are called Room Temperature Ionic Liquids (RTILs) and are of great importance because they show the exact resemblance in characteristics with organic liquids and can be easily used as solvents salts. They are made up of an organic cation (imidazolium, pyridinium, pyrolidinium, ammonium, phosphonium, sulfonium and morpholinium) and an inorganic (fluorinated anions, halides, sulfonates, nitrate hydroxides) or organic (carboxylates, tosylates) anion [1].

In the past few years ionic liquids have gained a great importance both in scientific research and process design because of its versatile properties (low vapour pressure, high heat resistivity, greater ionic conductivity, design flexibility etc.). Many research groups are trying to make more developments in ionic liquids so that their functionalities can be enhanced. At industrial scale, ILs have been used in replacing volatile organic compounds (by this reducing VOC emission) and as thermal fluids with the ultimate objective of saving energy [4].

1.3. Properties of Ionic Liquids

ILs have low melting points because of larger size of their ions, their low charge density and mainly because of the asymmetry of their cations. Due to the high number of cations and anions that can compose the ILs and the extremely high number of possible combinations between them, their properties can be fine tunable by changing the chemical composition, the size, the structure of ions and the nature

and size of alkyl side groups connected mainly to the cation. They are good solvents for both polar and non-polar substances which allow their application in extraction processes and chemical reactions as reaction media. Task specific ionic liquids have special applications in CO_2 capturing, catalysis and in other processes by giving them special functional groups that helps to perform different task in specific ways. The wide range of applications of ILs is mainly due to their low vapour pressures and high stability [1].

Due to their flame retardant properties and low volatility, ILs have found vast applications in making high power storage electrochemical capacitors that helps in more safety and energy boosting. To store high power in batteries they are used as electrolytes. RTILs showed more stability and conductivity compared to other non-aqueous electrolytes. Its conductivity ranges from 0.1 to 20 mS cm^{-1} and some key properties are involved behind its high range of conductivity like viscosity, density, ion size and mobility as well as the structure [5].

ILs are used as electrolyte alternatives in energy storage systems like lithium-ion and lithium-metal batteries (Fig 1.1) providing several benefits due to their non-flammability and low volatility. Some specific acyclic ammonium base ILs with azepanium or 3-methylpiperidinium cations can be used to make reversible lithium metal batteries with the power of 6V. Besides producing safe batteries, water-free proton-conducting membranes have been created by using ILs [6].

Fig 1.1. Lithium Ion Batteries

On the other hand, ILs play a significant role in the production of compounds and supramolecular systems in medicine, including drug synthesis and delivery. Depending on the structure, amount of water and the organism type with which they are going to interact, ILs have a wide range of biological activities. Their

interactions are different depending on the single-cell organism to the complex organism. For instance, specific ILs can enter the cell by passing or disrupting the lipid bilayer membrane and can damage the whole cell or even cause its death. Some of the specific ionic liquids can show resistance against bacteria and fungi by presenting their antimicrobial properties, which can also affect useful microbes. Cancer cells can also be destroyed by ILs but here loss of normal ones also occurs and its anticancer properties are still being under study. The introduction of the active pharmaceutical ingredient ionic liquid (API-IL) concept gives high demands to ILs in the field of pharmaceutical formulations and drug delivery [6].

IL-drug systems, when introduced in the body tend to provide a stable chemical environment for the drug so that it travels safely to its target place without being decomposed, helping in the control and slow release of drugs making them more effective. ILs increases the drug solubility and makes it more bioavailable and helps the drug to pass easily from the skin and enable it to work. Thus, drug delivery process becomes easier by reducing size of drug in the form of nanocrystals. The other approach is to reduce crystal lattice by using salts or cocrystals. By using different processes, the solubility of drug increases by maintaining the active ingredient. Targeted drugs are released into specific tissues (Fig 1.2) as prodrugs containing peptides, antibodies and specific enzymes to release the drug into specific tissues. ILs helps these drugs to pass through the membrane to work properly by enhancing its solubility such it can even help drugs to pass through the brain membranes that helps in treatment of tumor [6].

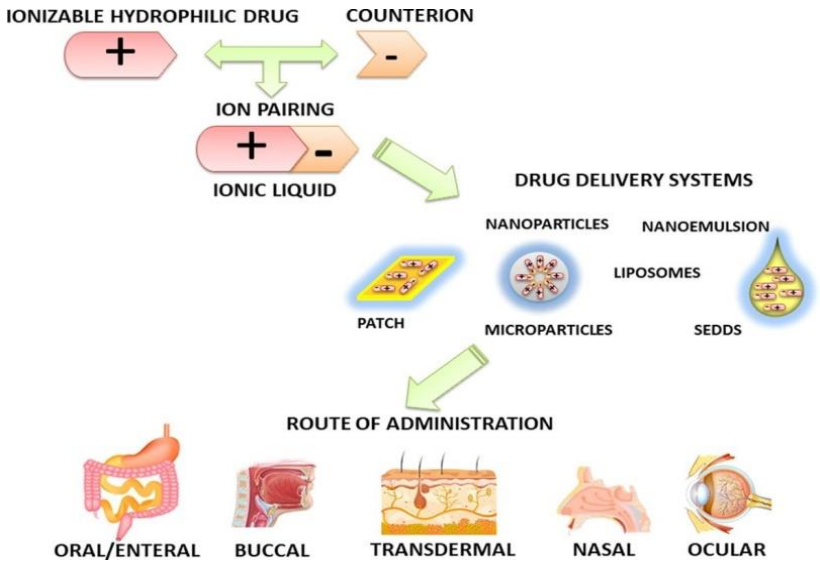

Fig 1.2. ILs in Drug Delivery

On the other hand, the unique properties of ILs allow them to behave as catalysts and also provide reaction media for the preparation of compounds to minimize metal catalyst contaminations and reduce volatile solvent use.

1.4. Applications in Separation Chemistry and Catalysis

Ionic liquids (ILs) have found broad applications in organic synthesis, electrochemistry, liquid-phase extraction, green catalysis, and polymerization but they are used first most in liquid-liquid extraction because of their adjustable and valuable properties. Using ILs as mobile phase in liquid chromatography minimizes tailing, and increases peak symmetry and resolution by covering the silanol groups on silica and retention time can be changed by changing the ILs concentration and alkyl group length. Instead of using organic solvents which are not much friendly to nature, ILs are able to separate organic compounds, metal ions and biologically active compounds from water-based solutions. ILs have important applications in separation by gas chromatography and liquid chromatography. Chemically attachment of ILs with the stationary phase enhances the separation of both non-polar and polar compounds. In the case of gas separation processes, ILs are embedded on the solid supports that are porous. By using these impregnated membranes, removal of acidic gases and CO_2 helps in purification processes and CO_2 can be separated and stored in this way. Ionic liquids are also used in reversed-phase chromatography and capillary electrophoresis to enhance separation [7].

In the field of catalysis, ILs are used for instance in the process of biotransformation where they work as catalyst and solvents for converting lignocellulosic material into useful and valuable chemicals like furfural and levulinic acid. ILs are also used in the form of a thin layer as heterogeneous catalyst in Supported Ionic Liquids Catalysts and in Supported Catalysts with Ionic Liquid Layer (SCILL) reducing the required quantity and cost. At first, ILs was used as a green solvent but later more work and research enhanced its applicability in many fields as a catalyst. They are used in acid catalysis because ILs have important functional groups on their cationic and anionic part that help them to behave as Bronsted acids [8]. For instance, ILs are widely used in acid catalysis processes like Aldol condensation, Aza-Michael addition, Beckmann rearrangement etc. ILs as basic catalysts has attracted great attention because they have the ability to be recycled as compared to inorganic bases. They are used efficiently in Michael additions involving active methylene compounds, condensations of aldehydes or ketones with hydroxylamine, and the synthesis of heterocycles such as quinolines and pyrroles [9].

1.5. Application to CO_2 Absorption

Carbon dioxide is the main contributor to the global warming, making its reduction or capture essential to the future of the planet. Membrane-based gas permeation is widely used for separating CO_2 from atmospheric gases like nitrogen. Ionic liquids (ILs) are effective in CO_2 selective membranes due to their high permeability and selectivity. Many supported IL-based membranes (SILMs), polymerized ILs, blended, and IL gel membranes have been developed, each with specific benefits and limitations. These kinds of membranes can be used to separate CO_2 from other gases. In the Fig 1.3 it is shown that 1-ethyl-3-methylimidazolium ethylsulfate is used for the physical and chemical absorption of CO_2. CO_2 is then removed from the surface by the pressure of 17 bar. This kind of achievement is helpful for the capturing of CO_2. This application enables ILs to dissolve high CO_2 in it [10].

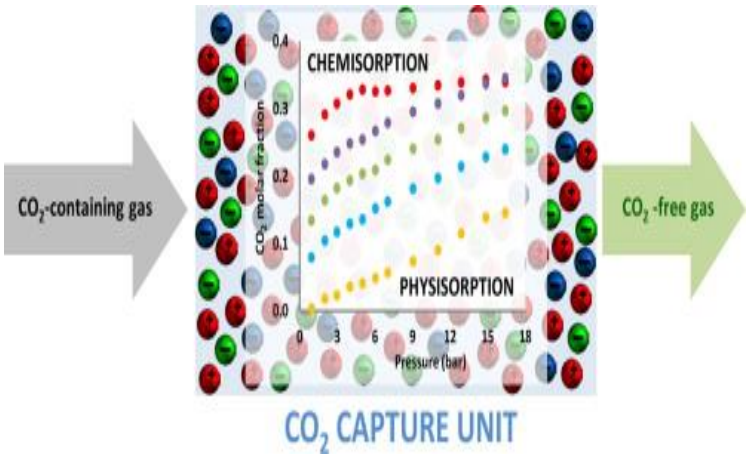

Fig 1.3. Absorption of CO_2 from the Medium Containing IL

1.6. Other Applications

Because of their low vapour pressure, high viscosity, solubility in organic solvents and high heat stability, ionic liquids have a great significance in lubrication processes. By using some ILs as lubricants the friction and energy wastage are reduced, which increases the life span of the equipment and improves its performance. ILs are still considered environmentally friendly in this particular context, since they are less volatile and less toxic compared to other organic compounds used as lubricants. They adsorb themselves on the solid surface and give a thick layer because of long alkyl chains. The thickness of layer

depends on the type of alkyl chain. The straight chain give thick surface and the branched chains give porous surfaces. In this way the oxidation of surface is reduced and it is safer and long lasting [11].

ILs can also be used as water based and oil based mixtures that help to make corrosion free surfaces. In fact, they have a great potential to be employed as corrosion inhibitors in many kinds of metal surfaces. It is also possible to prepare IL-based nanoparticles and nanostructures that are used to make many devices such as nano chips for brain in order to increase the functionality of neurons. ILs are also being used in these days in biotechnology for many applications like enzyme stabilization, protein solubility and in biomolecule extraction process. There are a lot of applications of ILs but their complexity and price brings a problem for their extensive use. However in these days scientists are trying to achieve cost effective ILs for future progress and development in human life, as well as trying to develop alternatives for the same uses, being one of them deep eutectic solvents. In the last decades, some ILs obtained from natural sources, such as amino acids and sugars have also been prepared and tested in order to alleviate the cytotoxic character of some IL.

1.7. Gels

Gels can be defined as small particle arrangements that cannot be seen with the naked eye but can easily be observed with a microscope. Gels can be soft (silica gels) or hard (gelatin). From 1991 to now thousands of articles have been published on gels and their different types. According to the intermolecular interactions gels can be physical or chemical. Chemical gels have covalent linkages and it cannot be reversed. They can be seen as extremely viscous materials containing a 3D geometry made by reticulate polymers whose voids are able to retain the solvent molecules, giving to the gel its known consistency. On the other hand, physical gels are formed by non-covalent bonding, which may be van der Waals or hydrogen bonding interactions and they can easily be reversed to the solution by heating. In this case, the reticulate structure that retains solvent molecules is formed through delicate intermolecular interactions rather than covalent bonds. In general, physical gels are able to produce sol-gel transitions by increasing/decreasing temperature, which is much more difficult to occur in chemical gels [12].

1.7.1 Hydrogels

Hydrogels are gels whose solvent (or one of the solvents, if more than one) is water. Chemical hydrogels are frequently composed by 3D polymer networks that can retain large amounts of water without losing their structure. Depending on their composition, they are classified into static and dynamic hydrogels. They have the characteristic of self-arrangement and change their shapes. Physical hydrogels are

composed by water and some kind of surfactant (amphiphilic) molecules, whose dual character towards water is the main reason for the formation of 3D structures around water, governed by non-covalent forces that made up the gels. Hydrogels are widely used in drug delivery, healing of wounds and tissue repair because of their property of retaining large amounts of water. They are also used in electronic and environmental sensors as well as in robotics [13].

1.7.2 Gels from ILs

Ionic liquid based gels are called Ionogels and different types of gels can be obtained from ILs combined with other materials (that can be organic, inorganic and hybrid). The organic source of ionic gels is, in most cases, gelling materials that can be added in small quantities yet able to form gels. These gelators can be carbohydrates, proteins and polypeptides, lipid base gelators like cholesteryl ester and cholesteryl chlorides and synthetic polymers. Such kinds of ionic gels are used in solar panels and heat resistive materials. IL gels that contain biopolymers like starch and cellulose used in high-capacity materials suggest more renewable alternatives [14].

Some ionogels are obtained by using inorganic matrices, such as those impregnated by silica particles whose density and viscosity depends on the fraction and size of these particles. The smaller the size of the silica particles, the larger is the contact area between silica and the ionic liquid and more intense is their mutual interaction. Special arrangements of this type of gels were studied using vibrational spectroscopy showing the hydrogen bonding between ionic liquid and water molecules that gives stable structure to the gel. ILs like $C_n$mimBF_4 and C_4mimPF_6 can create gels by mixing with silicon alkoxide using HCl as a catalyst. In these gels, their structure, pore size and stability can be influenced by the IL-like long carbon chains in imidazolium, giving more arranged formations while the anionic part also affects gel appearance and properties. Metal alkoxide gels are also obtained from ionic liquids like tin dioxide gel, alumina gels, vanadium oxide gels, and mixed oxide gels. ILs used in the formation of this kind of gels help ordered structure by forming hydrogen bonding [15].

Hybrid ionic liquid gels contain both organic and inorganic materials. This increases the functionality of these gels, like in Li-ion batteries addition of silica (Fig 1.4) improves the working of batteries [14].

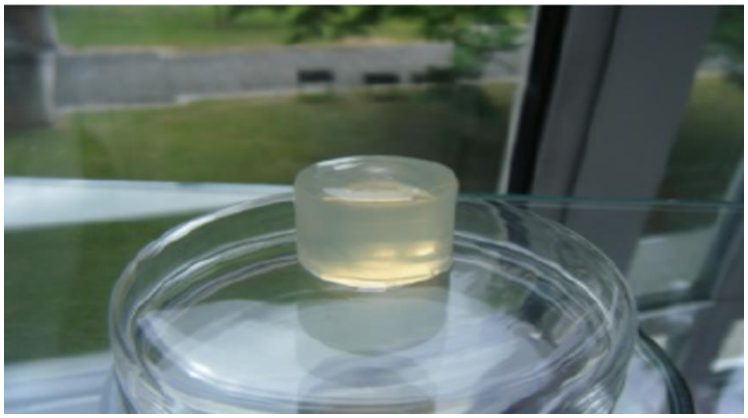

Fig 1.4. Ionic Liquid Gel produced by the method of sol-gel with ionic liquid

1.7.3 Mechanism of Gel Formation

As stated above, ionic liquids are salts that are liquid at or slightly above room temperature, composed by an inorganic or organic anion and an organic cation, some of the cations used to obtain IL having amphiphile properties- that's why some ILs, when mixed with water, within certain composition ranges, spontaneously form gels. Here our systems consist of simple gels having just water and ionic liquid (binary mixture), taking the form of water induced structures that lock up the alkyl chains within it [16].

Most ionic liquids don't form gels with water but a few of them are able to do that. These gels are strong, rigid and they can be used to make membranes (gas permeation / gas separation) that filter gases. The imidazolium based IL that form gels in a wide concentration range are 1-decyl-3-methylimidazolium chloride (C_{10}mimCl) and 1-decyl-3-methylimidazolium bromide (C_{10}mimBr). C_8mimCl (1-octyl-3-methyimidazolium chloride), C_8mimBr (1-octyl-3-methyimidazolium bromide) and $C_{10}mimNO_3$ (1-decyl-3-methyimidazolium nitrate) also form gels in a slightly narrow concentration range. C_{12}mimCl (1-dodecyl-3-methyimidazolium chloride) was also studied in this work.

The reason why C_{10}mimCl and C_{10}mimBr form gels is that there is the right balance between hydrophobicity and hydrophilicity in IL molecular structures. This amphiphilic nature traps the solvent molecules and give it a structure almost similar to surfactants. The imidazolium and the halide part is water loving (hydrophilic) and the tail part (C10) is hydrophobic. Their interaction with water creates three dimensional structures that are stable and form gels. These self-assembled structures are called

micelles whose size and shape are thought to change with composition and temperature, producing tri-dimensional structures. On the contrary, C_6mimCl is not able to form gels because of its short alkyl chain that doesn't allow it to make self-assembled structures and doesn't have strong hydrophobic interactions that helps in the formation of gels. So it shows itself more like ionic liquid than a gel. On the other hand, both C_8mimCl and C_8mimBr are able to form gels in a narrow range. It forms gels in a specific concentration and if the concentration, temperature and few other conditions are not precise and fixed then no gel is formed. Thus the gel formation strongly depends on the alkyl chain length that is imidazolium. Cl^- and Br^- also effects how strongly molecules bound to form van der Waal interaction. Cl^- forms stronger hydrogen bond interactions than the Br^- because chloride has smaller size and more negative charge density while bromide is bigger in size are less electronegative [16].

There is a clear connection between ionic liquid hydrogels and liquid crystals mesophase character because of similar molecular forces like amphiphilic interactions, hydrogen bonding, and van der Waals forces that help in the arrangement and formation of liquid crystals and ionogels [17]. C_{12}mimCl is a liquid crystal itself (presents mesophases in a large temperature range) without water because of its long alkyl chain, while the C10mimCl and C10mimBr need water to become liquid crystals [16].

1.7.4 Applications of Gels formed by Ionic Liquids

Ionogels are used in batteries composed of lithium and silica components, increasing the capacity and life span of these batteries. The silica material is very important in the excellent functioning of solar cells. Ionic gels used in optical instruments enhance the functionality of photoelectric devices by giving their components an environment similar to liquids. Ionic liquids do not show the problem of leaching so the ionogels give effective metal-catalyzed reactions. In the process of biocatalysts, ionic gels give a safe environment to enzymes and increase their sustenance under drastic conditions [14]. Ionic gels act as sensors and biosensors because they perform their function properly without disturbing the composition of media in electrochemical and optical sensing processes. They increase the sensitivity and detection of specific chemicals on a minimum amount like the determination of H_2O_2 on electrodes using ionic gel having an immobilized enzyme. By having such kind of advantages from ionic gels new paths become open for designing new materials with better efficiency and working capacity [18].

Objectives of the work

In order to be able to design useful gel systems composed only by ionic liquids and water, it is important to gain a systematic knowledge on the mechanisms of gelation within this kind of systems at molecular

level. Given the amphiphile character of the ionic liquids that are able to spontaneously form gels, it is undoubted that micelle formation occurs when solute and solvent are mixed together at concentrations above critical micelle concentration (CMC). Chemical structure of surfactant is highly important to decide the shape and size of micelle. It is expectable that, as the solute concentration increases, the number of micelles inside the solution also increases and probably also the average size of these micelles. One possible way for these systems to form gels is the gradual change of the shape of micelles as the solute concentration increases, in which they become elongated as they grow. These worm-like aggregates tend to present an entanglement and, in the limit, to form three dimensional structures by enrapturing the water molecules in them that leads to the formation of gel. This work intends to explore the mechanisms of gelation by investigating the possible changes of structure, size and shape of the aggregates formed by the solutes in water as a function of concentration. In order to do that, a two-fold approach (both experimental and theoretical) was adopted by studying binary IL/water mixtures at different proportions using the experimental technique Dynamic Light Scattering (DLS) and computer simulations using Molecular Dynamics (MD) method. Since the concentration highly matters in these systems and within a narrow range in concentration the formation of gel can happen and some dramatic changes can occur in a pre-gelation stage, a step by step approach is adopted concerning the concentration change, starting with more dilute solutions (yet always above CMC).

In this work, binary mixtures containing an ionic liquid and water, which have the capacity to form gels, have been studied in three different ways. In one hand, the gelation process has been investigated by studying IL/water mixtures with increasing concentrations, by evaluating the evolution of size and shape of IL aggregates in water as the solute concentration increases, using DLS and molecular dynamics simulations. In the case of DLS study, not only the diameter of the aggregates was determined, but also the zeta potential of the mixtures. On the other hand, the gels obtained by one of these mixtures have been studied within the gel concentration range, by obtaining its main rheological properties.

The ionic liquids used to prepare their aqueous mixtures were 1-decyl-3-methyimidazolium chloride (C_{10}mimCl), 1-decyl-3-methyimidazolium bromide (C_{10}mimBr), 1-octyl-3-methyimidazolium chloride (C_8mimCl), 1-octyl-3-methyimidazolium bromide (C_8mimBr), 1-decyl-3-methyimidazolium nitrate (C_{10}mimNO_3) and 1-dodecyl-3-methyimidazolium chloride (C_{12}mimCl). These systems were studied by Dynamic Light Scattering (DLS) and with Molecular Dynamic (MD) simulations as a function of IL concentrations at 298.15 K. The rheological properties of the hydrogel obtained from C_{10}mimCl (two different concentrations) were also studied at 298.15 K.

2. Experimental Section

2.1 Materials and solutions

All the ionic liquids used had high purity levels when purchased. 1-decyl-3-methyimidazolium chloride (C_{10}mimCl), 1-octyl-3-methyimidazolium chloride (C_8mimCl) and 1-octyl-3-methyimidazolium bromide (C_8mimBr) were purchased from Iolitec with purities of 0.98 (mole fraction), 0.98 and 0.99 respectively; 1-decyl-3-methyimidazolium bromide (C_{10}mimBr) and 1-dodecyl-3-methyimidazolium chloride (C_{12}mimCl) were purchased from BLD Pharm with purities of 0.98 and 0.99, respectively.

$C_{10}mimNO_3$ was not purchased but synthesized in the lab by the reaction of C_{10}mimBr with $AgNO_3$, following the procedure described by Benjamin T. Nebgen et al [18]. C_{10}mimBr was dried for few days under vacuum and then it was treated with silver nitrate and stirred overnight in a round bottom flask containing C_{10}mimBr and water, under dry nitrogen gas, protected from sunlight. Mixture filtration was done to remove AgBr using a Whatman filter. The liquid part of the mixture was centrifuged under 4500rpm to remove extra AgBr until the solution was completely clear. The centrifuged liquid solution was stored for 5 days in the dark and after that that the solution was centrifuged again to extract bromide completely. Water was then evaporated at 100^0 C in an open beaker in dark. The residue of the evaporation was mixed with CH_2Cl_2 to remove traces of precipitated $AgNO_3$. The solution was then filtered and CH_2Cl_2 was removed by evaporation under normal pressure. The product was dried for 1 week and the $C_{10}mimNO_3$ obtained as a pale yellow liquid. The procedure did not lead to darkening of the product upon exposure to sunlight, which is an indication that the Ag salts have been removed. The purity of the product was checked by ^1H and ^{13}C NMR and ATR-FTIR and the three spectra (shown in Supporting Information) present the characteristic peaks of $C_{10}mimNO_3$ in accordance with Nebgen *et al* [18].

All the ionic liquids were dried for a week on a heating plate in a water bath, and the heating temperature for all of them was set to 70-75C. After drying, the water content of ILs was measured in a coulometer (Karl Fisher Coulometer with the model KF831 from Metrohm) and this water content was taken into account for the calculation of the concentration of solutions and the water contents of ILs were always in the range of 300-3000ppm. The IL solutions with different concentrations were prepared by mass, under dry nitrogen, using ultra-pure MiliQ water with a resistivity of 18.2 MΩcm.

For DLS analysis, these solutions were previously filtered with PTFE membrane filters with the pore size of 0.20 μm.

2.2. Experimental procedure

2.2.1 Dynamic Light Scattering

A Zetasizer Nano ZS Malvern Instrument Ltd. was used for the determination of hydrodynamic diameter and the zeta potential of all the solutions at 298 K. In order to obtain the hydrodynamic diameter of the aggregates inside the solutions, a scattering angle of 173º was used and the wavelength of the radiation was 540 nm. The average intensity autocorrelation functions were analyzed using the cumulant analysis method and also a multi-modal approach (CONTIN algorithm) allowing the determination of size distribution of the particles in each sample.

The calculated autocorrelation function allows the determination of the diffusion coefficient of the particles of the samples, being the average hydrodynamic diameter automatically obtained from the Stokes-Einstein equation:

$$D_i = \frac{kT}{6\pi\eta R_H} \quad \text{..... (2.1)}$$

where D_i is the diffusion coefficient of the particles, T is temperature, k is the Boltzmann constant, η is the solvent viscosity and R_H is the hydrodynamic radius of the particles, from which the hydrodynamic diameter is obtained.

The measurements were done with the solutions contained in disposable folded capillary Malvern cells. These cells are equipped with a pair of plane electrodes making it possible to obtain zeta potential of each sample by measuring the electrophoretic mobility of the particles in the solution. All the samples were kept in the cells to rest for one whole day before the measurement, so that aggregates got time for its formation and then on the next day were run in the DLS apparatus. In the size determination, 20 measurements with 20 runs each were carried out for each sample studied, with a temperature equilibration time of 300s at 298 K. The value of the viscosity of water was considered equal to 0.8901 cP (at 298 K). The refractive index values of all solutes were different, while a fixed refractive index value of 1.330 was used for water. The refractive index of the solutions was estimated as the mole fraction weighted average between solute and solvent.

The concentrations of all the solutions studied by DLS for all the systems are presented in table 2.1 and the refractive indexes of all the solutes at 298 K are presented in table 2.2.

Table 2.1 Concentration of all the aqueous solutions studied by DLS

Concentrations of Solutions for all ILS					
No.	C10mimCl (mM)	C10mimBr (mM)	C8mimCl (mM)	C8mimBr (mM)	C12mimCl (mM)
1	69.88711	49.9819703	298.512014	199.89766	19.34011073
2	120.7855	98.5476618	507.660285	505.107838	70.31110142
3	249.7583	200.14028	1005.2967	751.975599	103.1801367
4	499.4073	499.798578	1970.86056	1000.27073	201.6591083
5	748.2071	689.553753	3022.71292		504.7405618
6	999.036	997.681177	3236.73986		748.3057292
7	1241.391	1491.34811			1005.967527
8		1975.97757			1496.827123

Table 2.2 Refractive index for all the ILs at 298 K

Refractive Index Values Used In DLS		
No.	**Name of compounds**	**Values**
1	C10mimCl	1.499
2	C10mimBr	1.517
3	C8mimCl	1.510
4	C8mimBr	1.522
5	C12mimCl	1.480

For zeta potential determination (which was carried out at the same temperature, 298 K), all the properties and operation parameters used, such as refractive index, viscosity and equilibration time, were the same as for diameter determination. However the dielectric constant of the solvent is an additional parameter and the value used was 78.3. 20 zeta potential measurements were carried out for each sample with between 10 and 100 runs per measurement.

2.2.2 Rheology

Binary system C_{10}mimCl+H_2O was studied in gel phase (using two different concentrations), by obtaining its main rheological properties. Rheological measurements were conducted using a Kinexus Pro rotational rheometer from Malvern, equipped with cone and plate geometry (20 mm diameter plate, 0° angle, and a 1 mm gap). The temperature of the experiments was precisely controlled by a Peltier element at the base of the fixed plate, with an accuracy of 0.01 °C.

The rheological studies included viscometry measurements in rotational shear rate-controlled mode (with shear rates ranging from 0.0001 to 100 s^{-1}) and viscoelastic tests in oscillation mode using strain sweeps (to determine the linear viscoelastic region – LVER), frequency sweeps (ranging from 0.0001 to 100 s^{-1}), and temperature sweeps at single values of frequency and strain (with temperatures ranging from 10 to 80 °C). The hydrogels were analysed at the temperature of 298.15 K.

2.2.3. Simulation Details

CL&P force field [19] and TIP4P-2005 [20] (both based on OPLS-AA [21]) were used to model all of our ionic liquids and water, respectively. Cross interaction parameters for vdW pair interaction energy and site diameter were obtained by geometrical mean rules:

$$\varepsilon_{ij} = \sqrt{\varepsilon_{ii}\varepsilon_{jj}} \quad \text{..... (2.2)}$$

$$\sigma_{ij} = \sqrt{\sigma_{ii}\sigma_{jj}} \quad \text{..... (2.3)}$$

where ε_{ii}, ε_{jj} and σ_{ii}, σ_{jj} are, respectively, the energy and the diameter between atoms of the same type.

Non-bonded interactions are considered between pairs of atoms within the same molecule, provided that they are further apart from each other more than 3 chemical bonds. For pairs of atoms far apart by exactly 3 bonds (1-4 interactions), the interaction energy is calculated by summing the dihedral and non-bonded, both multiplied by 0.5. Bonds involving hydrogen atoms were considered rigid, and the algorithm LINCS was used to constrain these bonds to their equilibrium length.

GROMACS program with the version 2016.1 was used for all the simulations. A total of 6 IL/water binary systems have been studied, with different IL/water proportions for each system. The number of molecules in each simulation box is given in the table 2.3. For each box (with side lengths between 8 to 20 nm), periodic boundary conditions were applied in three directions of space.

Table 2.3 Number of molecules of each component for all the mixtures studied by simulation

C10mimCl+H_2O				
No.	N (C10MimCl)	N (H2O)	N (total)	x (C10MimCl)
Box 1	40	15960	16000	0.0025
Box 2	90	9910	10000	0.009
Box 3	80	15920	16000	0.005
Box 4	180	9820	10000	0.018
Box 5	320	9680	10000	0.032
Box 6	580	9420	10000	0.058
C10mimBr+H_2O				
No.	N (C10MimBr)	N (H2O)	N (total)	x (C10MimBr)
Box 1	90	9910	10000	0.009
Box 2	80	15920	16000	0.005
Box 3	180	9820	10000	0.018
Box 4	320	9680	10000	0.032
Box 5	580	9420	10000	0.058
C8mimCl+H_2O				
No.	N (C8MimCl)	N (H2O)	N (total)	x (C8MimCl)
Box 1	120	9880	10000	0.012
Box 2	100	14900	15000	0.006666667
Box 3	300	9820	10120	0.029644269
Box 4	300	4700	5000	0.06
Box 5	500	4500	5000	0.1
C8mimBr+H_2O				
No.	N (C8MimBr)	N (H2O)	N (total)	x (C8MimBr)
Box 1	120	9880	10000	0.012
Box 2	100	14900	15000	0.006666667
Box 3	300	9820	10120	0.029644269
Box 4	300	4700	5000	0.06
Box 5	500	4500	5000	0.1
C12mimCl+H_2O				
No.	N (C12MimCl)	N (H2O)	N (total)	x (C12MimCl)

Box 1	90	9910	10000	0.009
Box 2	80	15920	16000	0.005
Box 3	180	9820	10000	0.018
Box 4	320	9680	10000	0.032
Box 5	580	9420	10000	0.058
$C10mimNO_3+H_2O$				
No.	N ($C10MimNO_3$)	N (H2O)	N (total)	x ($C10MimNO_3$)
Box 1	40	15960	16000	0.0025
Box 2	90	9910	10000	0.009
Box 3	80	15920	16000	0.005
Box 4	180	9820	10000	0.018
Box 5	320	9680	10000	0.032
Box 6	580	9420	10000	0.058

The protocol used for running simulations includes:

1) Box formation with specific number of molecules and then the dimensions were set to every box separately, according to the experimental density of the solutions.
2) An energy minimization run using the steepest descent method with $1x10^6$ steps.
3) A first NpT equilibration run during 10 ns using a time-step of 0.5 fs
4) A second NpT equilibration run using a time-step of 1 fs during a simulation time between 20 and 60 ns, depending on the system and the concentration. The attainment of equilibrium was ensured by the constancy of some key properties as energy and density.
5) A 50 ns production run in the same NpT ensemble, using also a time-step of 1 fs. The properties of the system and all the structural analysis were done from the trajectory obtained in this last simulation.

Both the van der Waals and charge interactions were calculated using 1.6 nm cut-offs. Particle Mesh Ewald sum was used for calculating the interaction energies beyond the Coulomb cut-off and analytical corrections to pressure and energy were used to correct the van der Waals interactions. Temperature for all simulations was kept at 298.15 K. From the simulation trajectories, radial distribution functions (RDFs) and the occurrence probability of aggregates as a function of the aggregate dimension are obtained, compared, and discussed. RDFs were calculated with the gmx rdf tool from GROMACS and the aggregation analyses were performed with the AGGREGATES program by Bernardes [22][23].

3. Results and discussion

3.1 Dynamic Light Scattering – size measurements

The size distribution of the aggregates presented in all the studied binary systems has been obtained using DLS technique, as a function of composition at 298 K.

3.1.1. C_{10}mimCl+H_2O

The size distributions obtained both by intensity and by volume for the system C_{10}mimCl+H_2O are shown in figure 3.1 for just one concentration as an example. The size distributions for the remaining concentrations of this system are presented in Supporting Information. As can be seen in the figures, the mixtures studied, despite being polydisperse, have aggregates whose diameter is mostly centred around single values, as can be seen from the volume-based size distribution graphs.

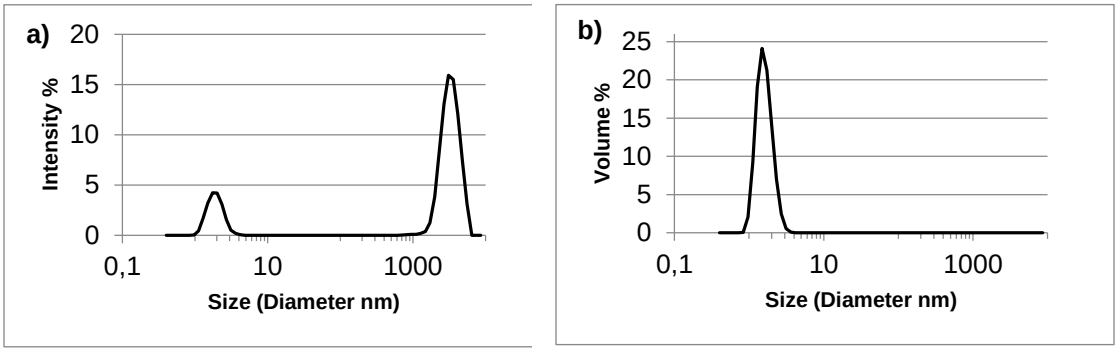

Fig 3.1. Intensity (a) and Volume (b) based size distribution results for C_{10}mimCl+H_2O with a solute concentration of 120mM

From graphs (a) and (b) of figure 3.1, we can conclude that, for the solute concentration of 120mM, the micelle diameter for all micelles has its maximum probability from 1-2 nm and the bigger peak in intensity from 1000-10000nm may be some dust or impurity.

For this system, the diameters corresponding to the maximum of the size intensity-based distribution (most likely average diameter of the aggregates) as a function of concentration are presented in table 3.1 and shown in figure 3.2. In table 3.1, the intensity percent of the chosen peak and the polydispersivity index (PDI) which reflects the uniformity of the aggregates, are also presented. If the value corresponding to the lowest concentration (close to the CMC) is disregarded, the size of the aggregate seems to decrease with the increasing concentration until around 1000 mM and tends to stabilize or even slightly increase

above that concentration. This is a surprising behaviour because it is legitimate to think that, as the concentration increases, approaching the gel limit, the size of the solute aggregates would tend to increase in a way to form complex structures that are capable to trap the solvent molecules. This result probably means that the gel formation as the concentration exceed a given value is a more sudden process and the slight increase in the aggregate size in the concentration range 1000-1600 mM indicates that de gelling process would occur at higher concentrations that those tested in this work and in a narrow range.

Table 3.1 Peak values and PDI values for all concentrations for C_{10}mimCl

Concentration (mM)	Peak		PDI
	Size	%	
70	4.060	18.8	1
120	1.011	64.5	0.667
250	1.898	87.8	0.163
500	1.458	68.4	0.858
750	1.431	97.1	0.1
1000	1.212	80.3	0.645
1241	1.27	89.7	1
1250	1.237	51.2	0.966
1600	1.369	97.4	0.061
Average Diameter = 1.4451			

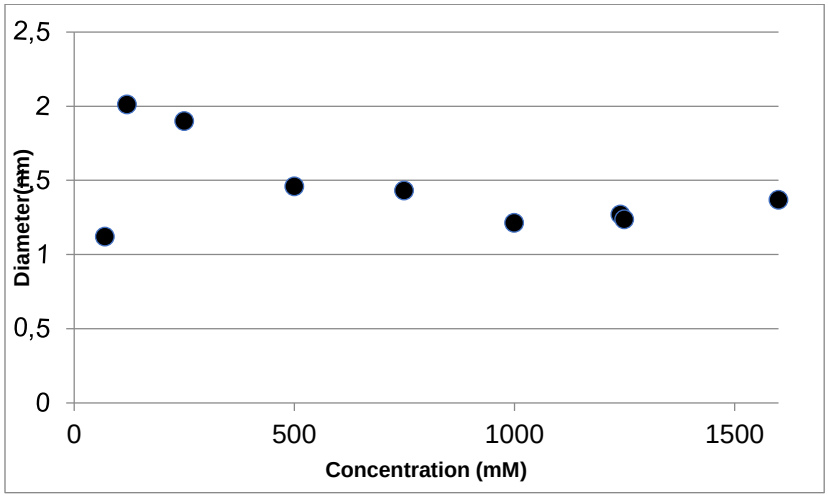

Fig 3.2. Aggregate size for maximum of intensity-based distribution for the system of C_{10}mimCl + H_2O for all concentrations tested by DLS

3.1.2 C_{10}mimBr+H_2O

For this system, the size distributions obtained both by intensity and by volume are also presented for just one concentration (50 mM) as an example (in figure 3.3) and the results for the remaining concentrations are shown in Supporting Information. The profile shown by these figures is identical of the preceding system, where it is obvious the predominance of one type of aggregates (centered in a single size value, between 1 and 3 nm) despite polydispersivity of the system.

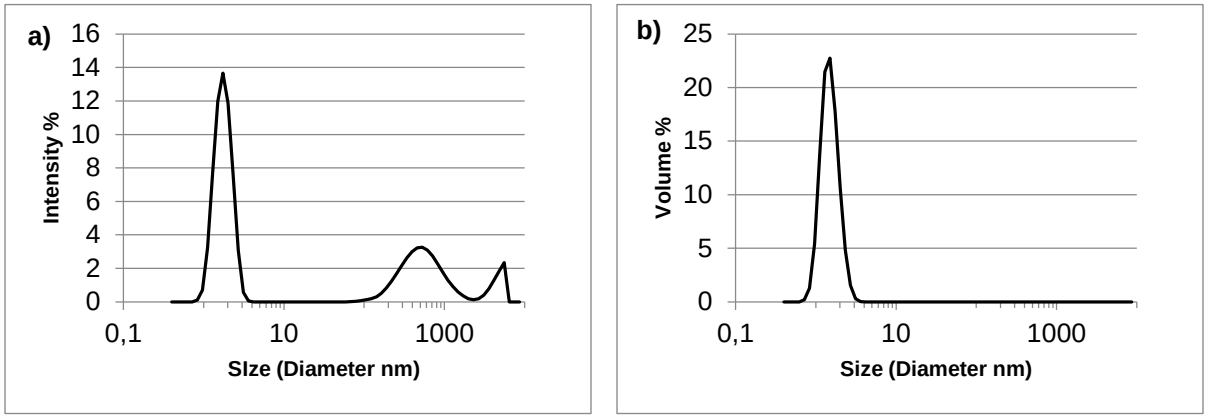

Fig 3.3. Intensity (a) and Volume (b) based size distribution results for C_{10}mimBr+H_2O with concentration of 50mM

The values of most likely average diameter of the aggregates as a function of concentration are presented in table 3.2 and shown in figure 3.4. As can be seen in the figure 3.4, there is a significant level of the dispersion in the size results and a clear trend of the dependence of the aggregate diameter with the concentration was not found. It seems that size of the aggregates doesn´t change with the concentration of the solutions within the studied range. This is a quite different behaviour than that observed for C_{10}mimCl+H_2O solutions, but there is an important characteristic in common: it is not possible to find, by analysing these results, any change of size or shape of the aggregates in the solutions as approaching the gel limit.

However, it is clear that, on average, the aggregate sizes of this system are higher than those obtained for C_{10}mimCl. This can be due to the size difference of in the anion — bromide is larger than chloride — which probably means that the anion is able to insert in a certain extent in the micelles formed essentially by the cations.

Table 3.2 Peak values and PDI values for all concentrations for C10mimBr

Concentration (mM)	Peak		PDI
	Size	%	
50	1.715	49.2	0.714
99	2.455	91	0.162
200	2.974	100	0.149
500	2.366	100	0.172
690	1.794	83.3	0.203
1998	2.846	100	0.169
1491	1.714	98.7	0.459
Average Diameter = 2.26629			

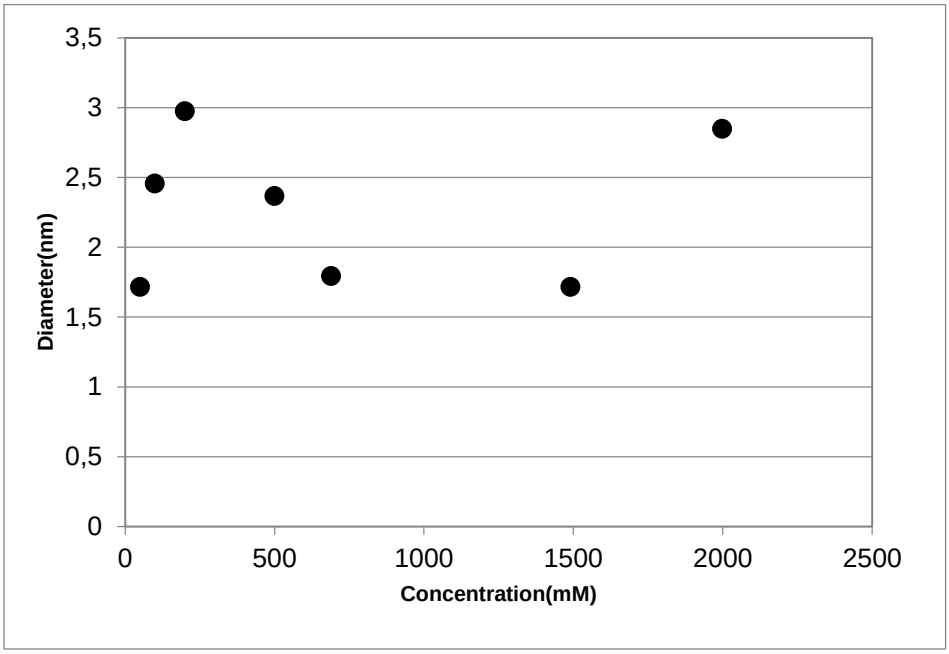

Fig 3.4. Aggregate size for maximum of intensity-based distribution for the system of C_{10}mimBr + H_2O for all concentrations tested by DLS

3.1.3. C_8mimCl+H_2O

In figure 3.5 the intensity and volume-based size distributions of the aggregates are shown for just one concentration (298 mM), for this system, being the graphs for the remaining concentrations presented in Supporting Information. As can be seen, this seems to be a more complex system, with higher levels of polydispersivity, but still a peak as the most important (as evidenced by volume-based graph).

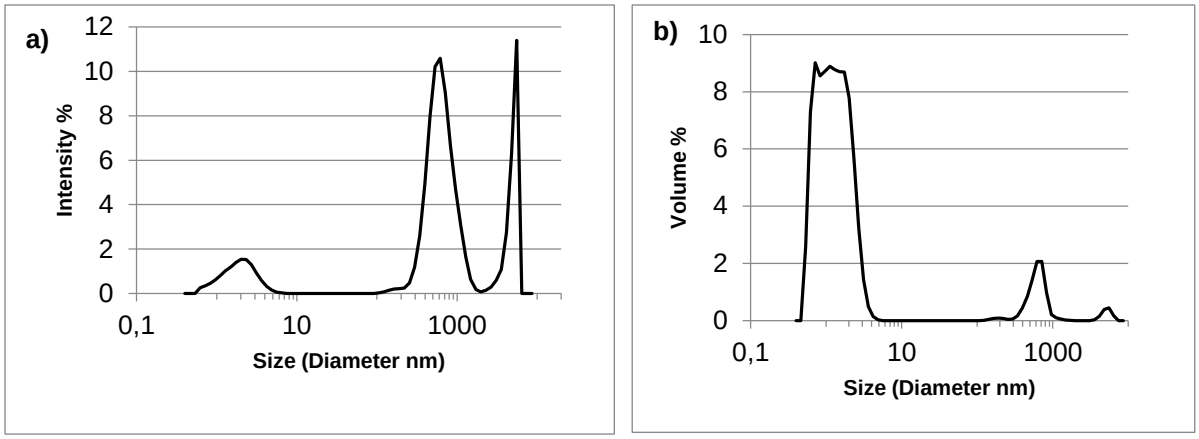

Fig 3.5: Intensity (a) and Volume (b) based size distribution results for C_8mimCl+H_2O with a solute concentration of 298mM

The values of the most likely average diameter of the aggregates as a function of concentration are presented in table 3.3 and shown in figure 3.6. The average diameter of the aggregates seems to present an interesting trend with the increasing concentration: decreases to a minimum value and then increases, which resembles the behaviour observed for C_{10}mimCl+H_2O. The size increase observed for the highest concentrations studied can indicate some structural changes in the aggregates that anticipate the gelling process.

Table 3.3 Peak values and PDI values for all concentrations for C8mimCl

Concentration (mM)	Peak		PDI
	Size	%	
304	1.856	66	0.402
500	1.716	87.7	0.146
507	1.853	81.2	0.204
1005	1.278	6.7	0.34
2005	0.9715	76.9	0.449
3022	1.635	88.3	0.159
3236	1.786	82.6	0.207
Average Diameter = 1.585071			

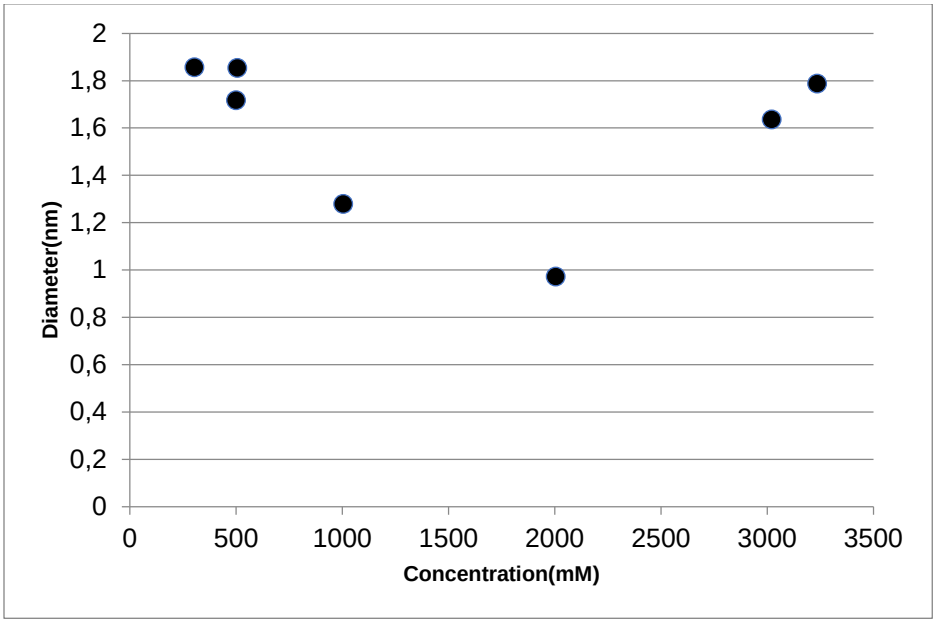

Fig 3.6. Aggregate size for maximum of intensity-based distribution for the system of C_8mimCl + H_2O for all concentrations tested by DLS

3.1.4 C_8mimBr+H_2O

For this system, the same size distribution graphs are presented for the concentration of 200 mM as an example (figure 3.7) and the values of most likely average diameter of the aggregates as a function of

concentration are presented in table 3.4 and shown in figure 3.8. The size distribution graphs for the remaining concentrations are shown in Supporting Information. These solutions seem to be less polydisperse than those for the preceding system, being the results more peaked around a single value (between 1.2 and 2.3 nm). Apart from the value for the lowest concentration, a slight decrease in aggregate size with the increasing concentration is observed, which is the same trend that has been registered for C_8mimCl+H_2O system until 1000 mM. On average, the aggregate size is higher than that for C_8mimCl+H_2O, probably for the same reason that was suggested for the systems based on $C_{10}mim^+$ cation: the higher dimension of bromide anion and its probable insertion in the micelles made of cations.

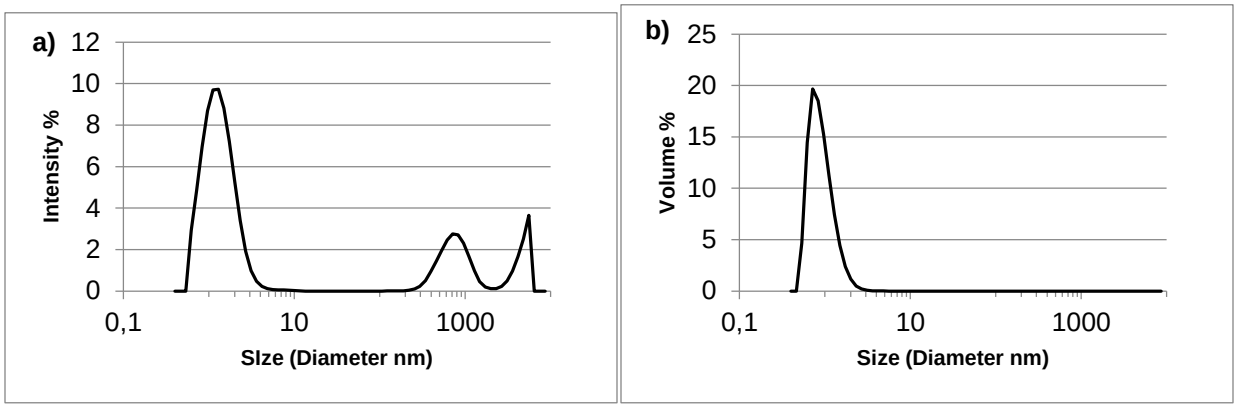

Fig 3.7. Intensity (a) and Volume (b) based size distribution results for C_8mimBr+H_2O with a solute concentration of 200mM

Table 3.4 shows the peak values and PDI values for all concentrations for C_8mimBr

Concentration (mM)	Peak		PDI
	Size	%	
200	1.291	60.7	0.535
505	2.255	97.9	0.175
751	1.933	91	0.146
1000	1.884	100	0.09
1503	1.935	100	0.162
2000	1.651	91.1	0.214
2993	1.617	82.2	0.295
Average diameter = 1.795143			

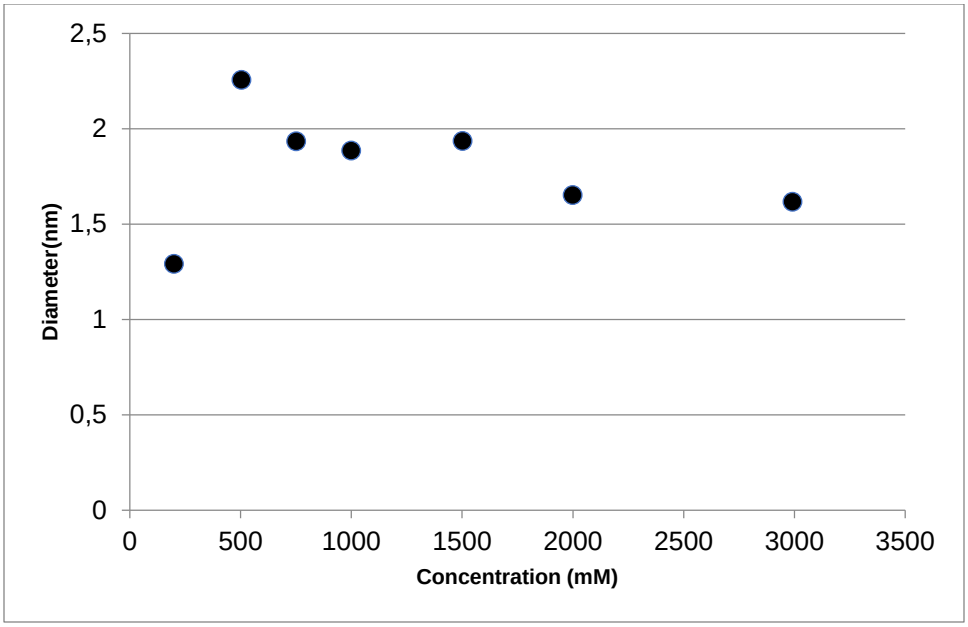

Fig 3.8. Aggregate size for maximum of intensity-based distribution for the system of C_8mimBr + H_2O for all concentrations tested by DLS

3.1.5 C_{12}mimCl+H_2O

Intensity and volume-based size distributions for just one concentration (103 mM) for this system are shown in figure 3.9, where it can be seen a clear tendency of the distributions to be peaked around 1-2 nm. The size distribution for the rest of concentrations can be found in Supporting Information. The average diameters as a function of solute concentration are presented in table 3.5 (where PDI values are also presented) and shown in figure 3.10. As can be seen, the most probable diameter of the aggregates in this system is constant with increasing concentration until a certain value (around 1000 mM) and for higher concentrations seems to present an increasing trend, which may indicate the beginning of a structural change associated to the gel formation. It must be stressed that C_{12}mimCl usually form mesophases (liquid crystal phases) even in pure state, without any water.

In figure 3.11 the average aggregate diameters (*d*), over the whole composition ranges covered, for C_8mimCl+H_2O, C_{10}mimCl+H_2O and C_{12}mimCl+H_2O systems are shown as a function of the alkyl side chain length of the cation [number of carbon atoms, *n*(C)], considering only systems with the same anion. Surprisingly, the average aggregate diameter decreases as the side chain length increases. Different possible explanations for this observation can be anticipated. The concentration ranges considered are not exactly the same, especially in the case of C_8mimCl+H_2O, for which the CMC is considerably higher and

the gel concentration windows is narrower. On the other hand, thinking about the aggregates as spherical micelles, it can be considered that larger cations (such as $C_{10}mim^+$ and specially $C_{12}mim^+$) may prefer more bent conformations, with some gauche defects, because their enhanced flexibility, becoming shorter for geometrical reasons. However, it is also possible that most of the aggregates formed are not spherical micelles, but much more complex entities instead, and C_8mimCl as a solute, with a smaller alkyl chain length in a more concentrated solutions, are more prone to form more disordered aggregates with large diameters. This hypothesis is somehow validated by the results from computer simulations, as will be mentioned below.

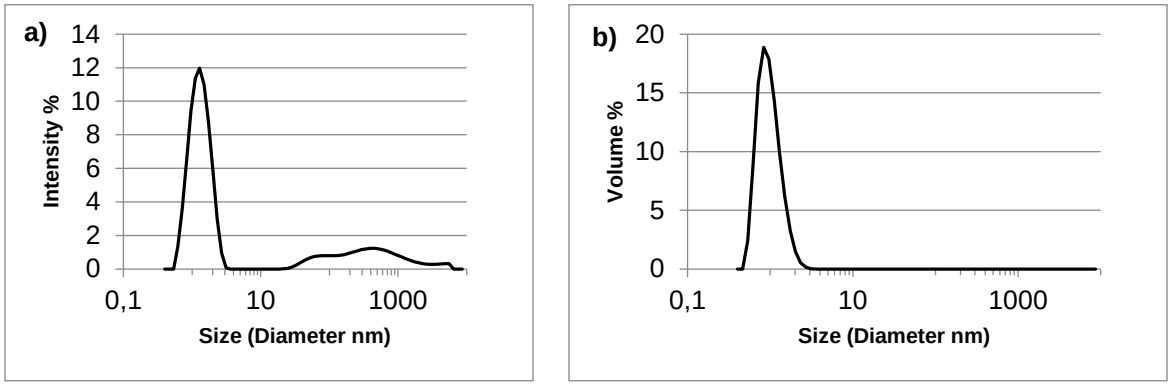

Fig 3.9. Intensity (a) and Volume (b) based size distribution results for C_{12}mimCl+H_2O with a solute concentration of 103mM

Table 3.5 Shows the peak values and PDI values for all concentrations for C12mimCl

Concentration (mM)	Peak 1		PDI
	Size	%	
103	1.291	75.9	0.264
202	1.159	9.7	0.448
505	1.143	44.2	0.965
748	1.28	9.6	0.496
1006	1.271	73.4	1
1497	1.761	90	0.282
Average diameter = 1.3175			

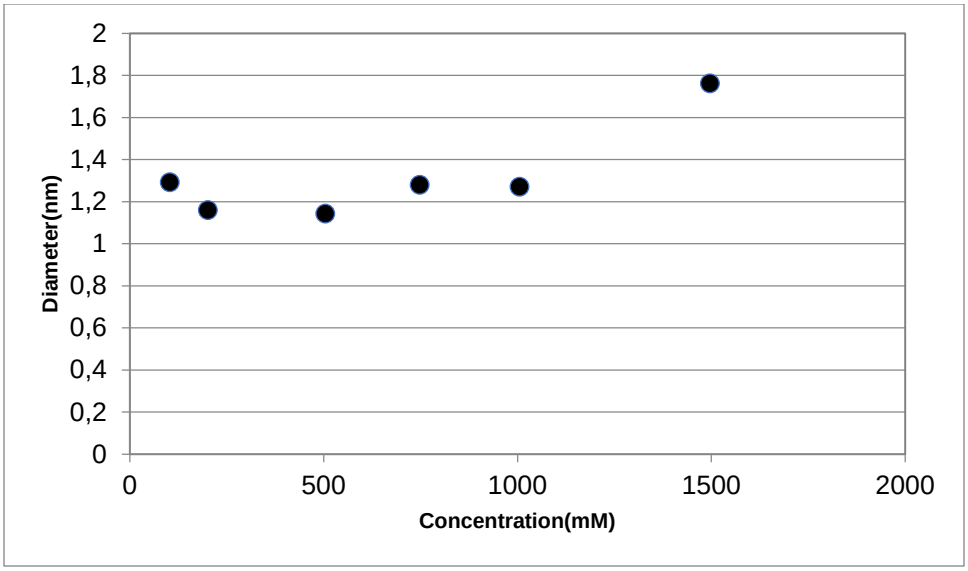

Fig 3.10. Aggregate size for maximum of intensity-based distribution for the system of C_{12}mimCl + H_2O for all concentrations tested by DLS

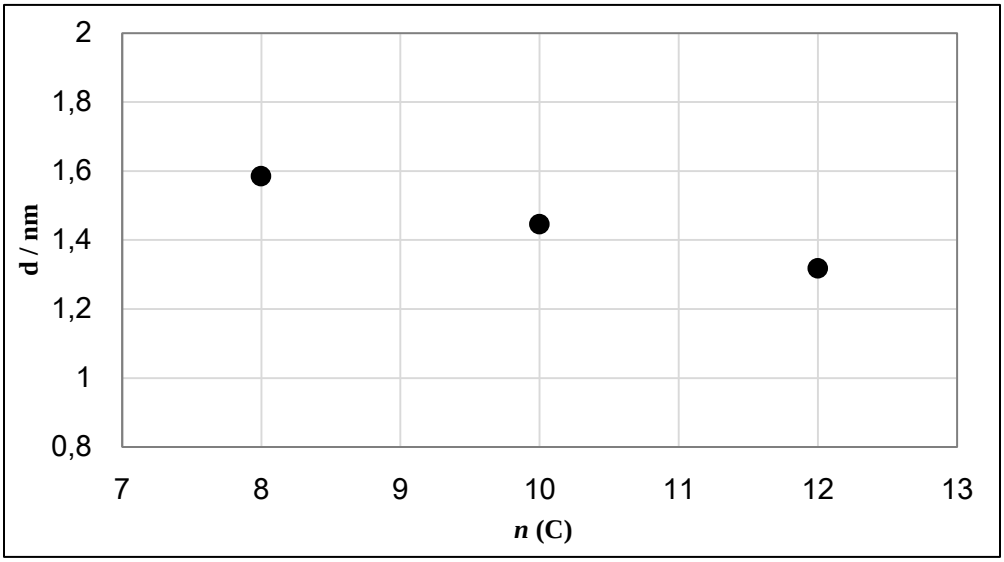

Fig. 3.11. Most probable aggregate diameter averaged over all the concentration range studied for systems including chloride as a function of the alkyl side chain length.

3.1.6 $C_{10}mimNO_3+H_2O$

Finally, the same set of results is presented for system $C_{10}mimNO_3+H_2O$. Size distributions peaked around a narrow range are visible in figure 3.12 (for just one solute concentration), corresponding to relatively low PDI values (as presented in table 3.6), which is an indication of almost monodisperse systems. Figure 3.13 shows that the most probable diameter of the aggregates in this system doesn't present any clear monotonic variation with solute concentration, with an average diameter (over the whole concentration range) of 2.09 nm, which is an intermediate value between those found for $C_{10}mimCl+H_2O$ (1.45 nm) and $C_{10}mimBr$ (2.27 nm), yet closer to the latter. This is due to the size of the anion. The radius of chloride and bromide are 181 pm 196 pm respectively [24]. The accepted radius for Nitrate is 179 pm for crystalline solid [25] (which is smaller than chloride) but a value of 316 pm has been reported for the solvated form of the anion [26]. Considering that nitrate should be partially hydrated in this system, the radius of nitrate can be in fact of the same order of magnitude than bromide, or, being prone to be solvated; it probably has a lower tendency to be inserted in the micelles, despite its large hydrated size.

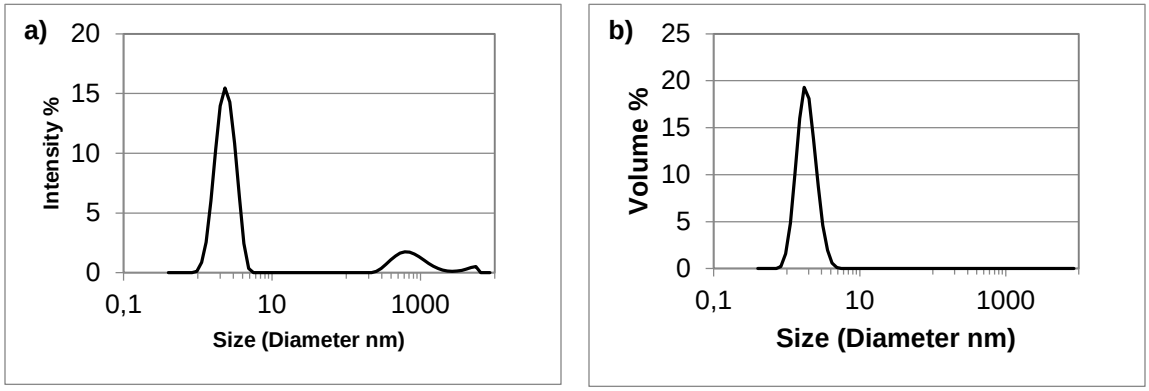

Fig 3.12. Intensity (a) and Volume (b) based size distribution results for $C_{10}mimNO_3+H_2O$ with a solute concentration of 119mM

For rest of all compounds with all concentration the graphs can be found in Supporting Information.

Table 3.6 Peak values and PDI values for all concentrations for $C10mimNO_3$

Concentration (mM)	Peak		PDI
	Size	%	
70	2.841	64.8	0.375
119	2.459	76.2	0.258
247	1.885	84.2	0.172
507	1.472	85.7	0.169
744	1.716	94.8	0.105
980	2.176	97.9	0.175
1257	2.332	84.8	0.208
1958	1.833	83.1	0.397
Average diameter = 2.08925			

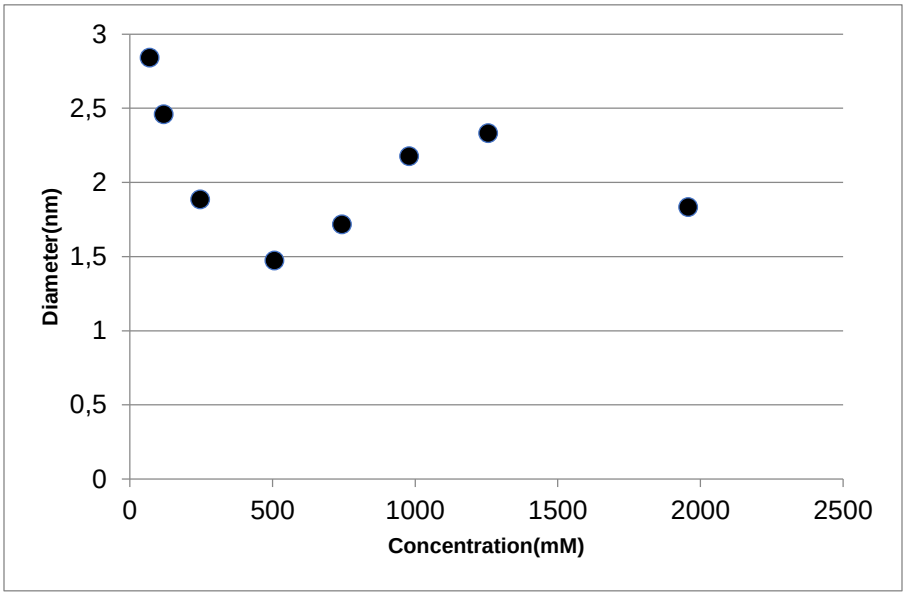

Fig 3.13. Aggregate size for maximum of intensity-based distribution for the system of $C_{10}mimNO_3 + H_2O$ for all concentrations tested by DLS

3.2 Zeta potential

The values of zeta potential obtained for all the systems and concentrations are collected in table 3.7.

Table 3.7 Zeta Potential Values for all Compounds

C_{10}mimCl+H_2O		**C_{10}mimBr+H_2O**		**C_8mimCl+H_2O**	
Concentration (mM)	Zeta potential	Concentration (mM)	Zeta potential	Concentration (mM)	Zeta potential
70	19	50	22	298	10.5
120	24.1	99	17.2	304	6.2
250	15	200	2.89	507	8.4
500	13.9	500	3.73	1005	15.7
750	-1.09	690	9.72	1970	-1.37
1000	33.3	998	3.97	3022	-10.3
1013	13.1	1491	12.1	3236	-0.00972
1241	27				
1250	0.981				
1600	20.9				
C_8MimBr+H_2O		**C_{12}mimCl+H_2O**		**C_{10}mimNO_3+H_2O**	
Concentration (mM)	Zeta potential	Concentration (mM)	Zeta potential	Concentration (mM)	Zeta potential
200	10.5	19	46.5	70	20.7
505	12.5	70	32.3	119	17.7
751	11.2	103	27.4	247	10.8
1000	15.5	202	26	502	8.9
1503	-12.8	505	26.2	744	8.57
2000	10.6	748	22.4	980	10.9
2993	0.0825	1006	17.8	1257	4.81
		1497	-19.8	1958	17.6

Almost all zeta potential values are positive which is expectable since the surfactant component of the solutes are the cations and it is expected that the outer surface of the micelles formed should be positive, with an appreciable mobility of the corresponding anions. On the other hand, almost all of the zeta potential values are below 30 which means that they are not stable; they have some tendency to form larger aggregates. However, the system C_{12}mimCl seems to have the most stable aggregates. In general,

zeta potential decreases as the solute concentration increases, which may indicate some tendency to form larger aggregates and/or more complex aggregates for higher concentrations of IL.

3.2 Rheology results

Only one system was studied (C_{10}mimCl+H_2O) in the gel region at two different concentrations (x_{IL} = 0.0802 and x_{IL} = 0.1423). The results for oscillation experiments as a function of shear strain (γ) for fixed frequency (ω = 1 Hz) are shown in figure 3.14 for both concentrations. As can be seen, complex and elastic moduli are approximately constat over an extended range of shear strain values, which is a typical behaviour of gel systems. Within this range, elastic modulus is higher than viscous modulus, producing a phase angle much lower than 45 º (around 20º), which is an indication that the sample has a predominant solid character. Both loss and storage moduli are higher for the mixture with x_{IL} = 0.0802 than for the one with x_{IL} = 0.1423, indicating that the former is more rigid than the latter. Furthermore, the phase angle of the mixture with x_{IL} = 0.0802 is higher, which means that it has a more solid character. For shear strain values above about 0.1 %, all the moduli tend to decrease steadily indicating a breakdown of the gel structure and a non-linear response of the rheological stimuli. In this particular, the mixture with x_{IL} = 0.0802 was found to be more stable than that with x_{IL} = 0.1423. For the rest of the oscillation experiments a value of shear strain of 0.04 % was used, comfortably within the linear viscoelastic region (LVER).

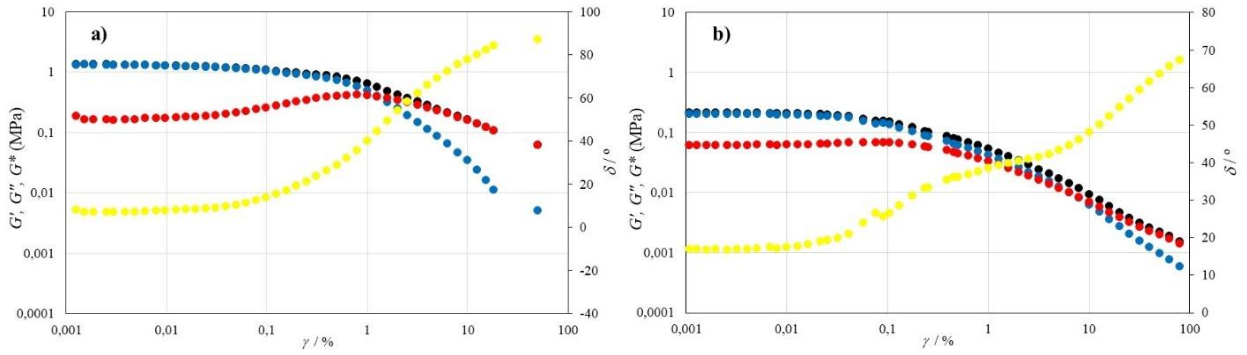

Fig 3.14. Oscillation moduli and phase angle for C_{10}mimCl+H_2O systems as a function of shear strain at fixed frequency for: a) x_{IL} = 0.0802; b) x_{IL} = 0.1423. Complex (black), elastic (blue) and viscous (red) moduli are shown, as well as phase angle (yellow, right axis).

The results for oscillation experiments as a function of frequency (ω) for fixed shear strain (γ = 0.04 %) are shown in figure 3.15, also for both concentrations. As can be seen, both loss and storage moduli increases and phase angle decreases as the frequency increases at lower frequencies, revealing that the samples becomes more rigid and solid with the increasing frequencies as usually happens with gels and,

for higher frequencies, the moduli and phase angle stabilize. The behaviour is very similar for both concentrations.

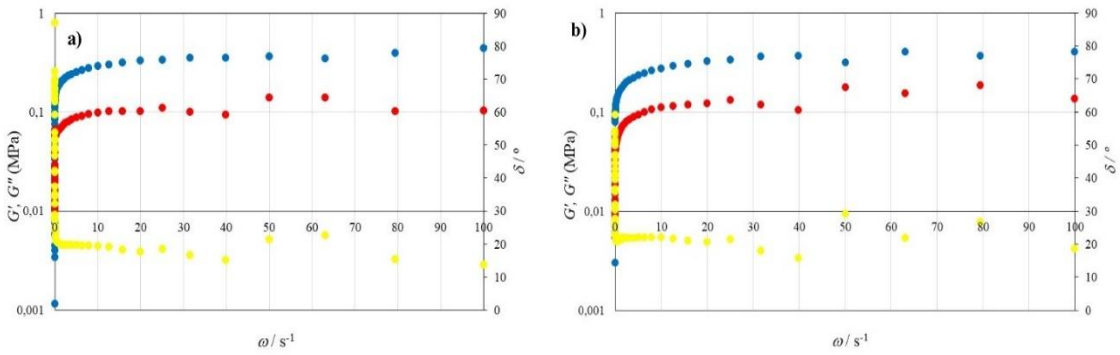

Fig 3.15. Oscillation moduli and phase angle for C_{10}mimCl+H_2O systems as a function of frequency at fixed shear strain for: a) x_{IL} = 0.0802; b) x_{IL} = 0.1423. Elastic (blue) and viscous (red) moduli are shown, as well as phase angle (yellow, right axis).

The results for oscillation experiments as a function of temperature (between 10 and 80 ºC) for fixed frequency and shear strain are presented in figure 3.16. It is clear that for the sample with x_{IL} = 0.0802, all the moduli abruptly drops between 30 and 40 ºC (about two orders of magnitude for complex and storage moduli), meaning that a reorganization of the gel structure should occur within this temperature range, probably a gel-sol transition. Only an analytical method based on thermal analysis can confirm this hypothesis. However, it is important to notice that even at temperatures above this transition the sample keeps its solid (elastic) character with a phase angle around 30º. Interestingly the sample with x_{IL} = 0.1423 shows a completely different behaviour with all the moduli gradually decreasing over an extended range of temperature. It is also clear that all the moduli are lower for the solution with x_{IL} = 0.1423 than for the solution with x_{IL} = 0.0802, as was stressed above. However a gel-sol transition seems to occur for the solution with x_{IL} = 0.1423 at a temperature around 70 ºC, leading to a sample that ultimately (at 80 ºC) has a more liquid character, evidenced by a phase angle around 50º.

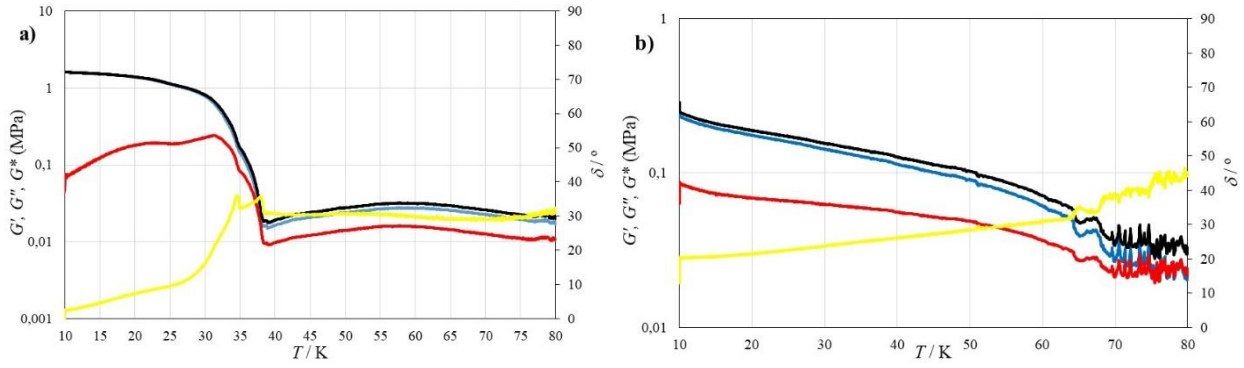

Fig 3.16. Oscillation moduli and phase angle for C_{10}mimCl+H_2O systems as a function of temperature at fixed frequency (1 Hz) and shear strain (0.04 %) for: a) x_{IL} = 0.0802; b) x_{IL} = 0.1423. Complex (black), elastic (blue) and viscous (red) moduli are shown, as well as phase angle (yellow, right axis).

The results of viscometry (viscosity as a function of shear rate) for both solutions studied are presented in figure 3.17 at a fixed temperature (25 ºC). Both samples show a marked shear thinning (pseudoplastic) behaviour with the viscosity decreasing by about five orders of magnitude over the range of shear rates imposed. As can be seen, viscosity is considerably higher for the mixture with x_{IL} = 0.0802 than for the mixtures with x_{IL} = 0.1423, seeming that, in this concentration range, viscosity decreases with the increasing solute mole fraction.

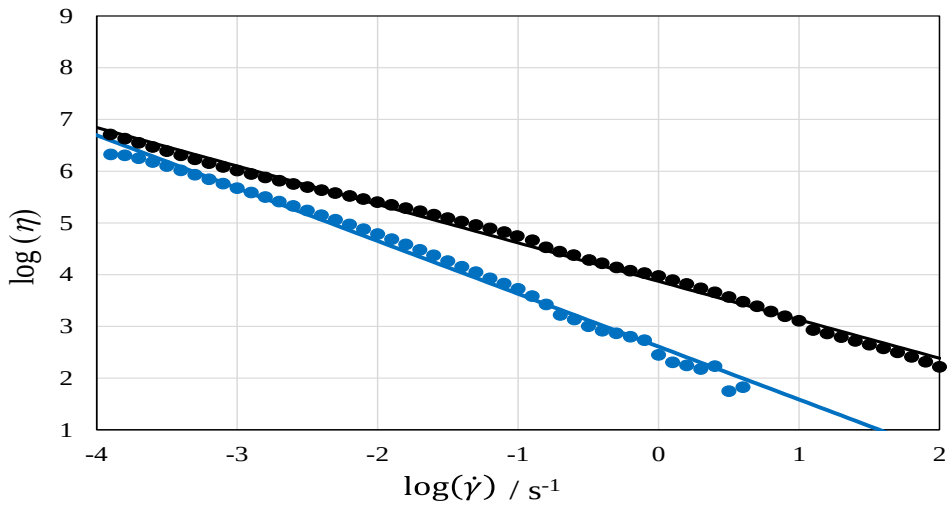

Fig 3.17. Viscosity as a function of shear rate for the C_{10}mimCl+H_2O system at 25 ºC for the compositions: x_{IL} = 0.0802 (black) and x_{IL} = 0.1423 (blue). Points: experimental results; lines: fitting to the Ostwald–de Waele relationship.

Both viscosity curves can be described by the Ostwald-de Waele model, whose version written in order of viscosity is:

$$\eta = K\dot{\gamma}^{n-1} \text{..... (3.1)}$$

or in its log version:

$$\log_{10}(\eta) = \log_{10}(K) + (n-1)\log_{10}(\dot{\gamma}) \text{ .....(3.2)}$$

where *K* is the flow consistency index and *n* is the flow behaviour index.

In table 3.8 the results of fitting viscosity values as a function of shear rate to Ostwald-de Waele model are shown for both concentrations. The very low values of *n* express the shear-thinning character of the mixtures, especially for the one with higher solute mole fraction (presenting a flow behaviour index around zero). The flow consistency index of the mixture with the lower solute mole fraction is considerably higher than that with the higher solute mole fraction, confirming that the former is a more consistent and stronger gel than the latter.

Table 3.8. Fitting Viscosity Values as Function of Shear Rate

x_{IL}	K / Pa s^n	n
0.0802	7421	0.256
0.1423	404.0	-0.022

3.3 Simulation results

The analysis of the simulation results was done based on the calculation of the average aggregation number as a function of their occurrence frequency (aggregate analysis) and radial distribution functions between relevant pairs of atoms.

3.3.1 Aggregate analysis

The aggregate analysis (occurrence frequency of aggregates as a function their number of molecules) at different concentrations studied and 298.15 K for the system C_{10}mimCl+H_2O is shown in figure 3.18. The same representations for the system C_{10}mimBr+H_2O are very similar to the previous one and are shown in

Supporting Information. As can be seen in the figure, for the lowest solute concentrations (x_{IL} = 0.0025) few aggregates are formed and the majority of the molecules are yet isolated from other ones. Increasing slightly the concentration (x_{IL} = 0.005), the probability of the occurrence of aggregates also increases, especially with dimensions around 8 and 14 molecules, but the isolated molecules still have the highest probability of occurrence. For x_{IL} = 0.009, isolated molecules have also a high occurrence probability, but it is clearly seen the formation of aggregates at two different sizes at around 12 and around 20 molecules. As the concentration increases to x_{IL} = 0.018, it is clearly observed that the two types of aggregates are formed, with dimensions around 14 and 25 molecules. At x_{IL} = 0.032 (corresponding approximately to 1780 mM, which is higher than the concentrations used in the experimental studies) the system appears to become polydisperse, with a slight increase of the aggregate dimension. This trend is reinforced at the highest concentration (x_{IL} = 0.058, corresponding to 3200 mM, well within the experimental gel region), where aggregates with several dimensions are observed, also with higher number of molecules (a maximum of 79). However, even within the concentration range for experimental gel formation, any percolation phenomenon was observed (by obtaining higher occurrence probabilities for aggregates containing all the molecules in the box).

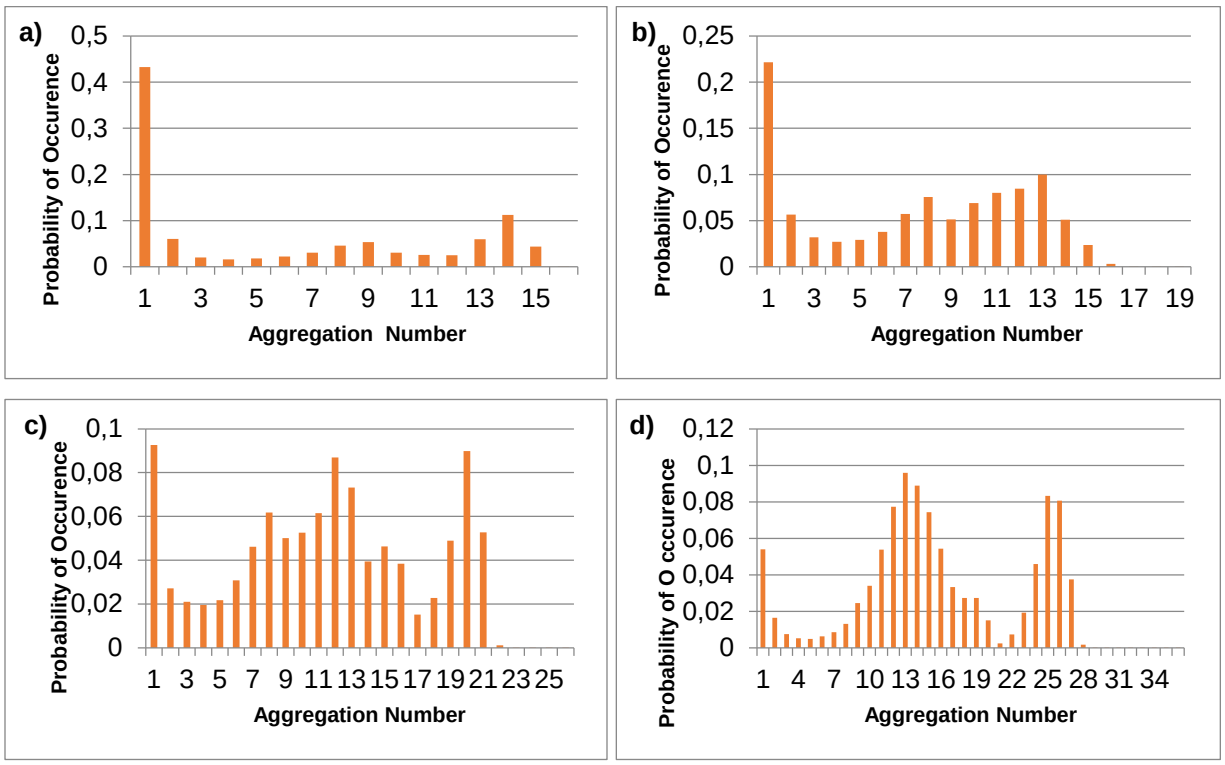

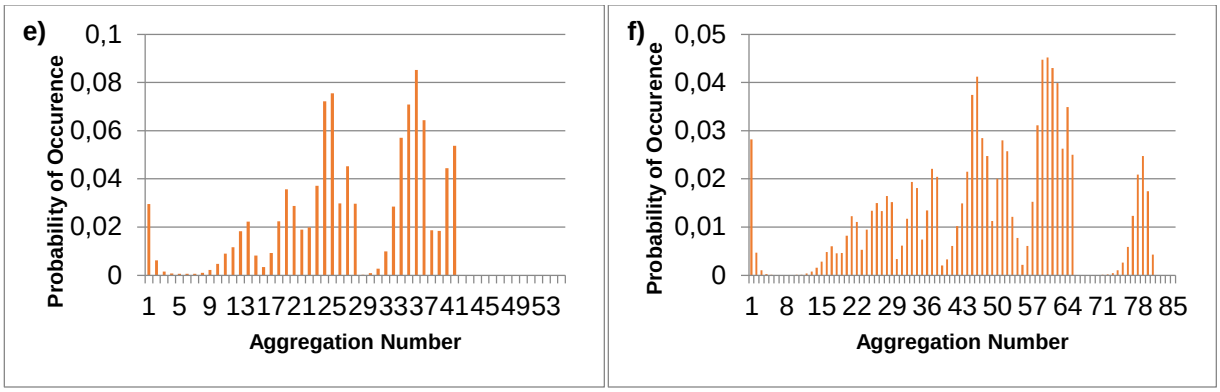

Fig 3.18. Aggregate analysis of C_{10}mimCl+H2O with all concentrations (a) 0.0025, (b) 0.005, (c) 0.009, (d) 0.018, (e) 0.032, (f) 0.058

The aggregate analysis for C_8mimCl+H_2O system is shown in figure 3.19, while the same results for C_8mimBr are shown in Supporting Information because they are quite similar to the system involving chloride. First of all, it is important to note that although the solute concentration studied is considerably higher than for systems involving $C_{10}mim^+$, for the lowest mole fractions (x_{IL} = 0.0067 and x_{IL} = 0.012), the majority of the molecules are yet isolated from other ones, following the experimental trend when these pair of systems are compared. Thus, simulation is able to describe the tendency of C_8mim^+ based systems of forming aggregates at much higher concentrations compared to $C_{10}mim^+$ ones. However, for x_{IL} = 0.012, it is also clear that aggregates tend to form with a distribution peaked around 7 molecules each. By further increasing the solute concentration (to x_{IL} = 0.0296) many aggregates are observed, keeping a monodisperse character of the solution with a most probable number of molecules per aggregate around 18. This monodispersivity is broken for x_{IL} = 0.06, where three different types of aggregates are observed and the tendency is again reinforced for the highest concentration (x_{IL} = 0.1) where five types of aggregates have been detected. As in the case of C_{10}mim halides, for C_8mimCl and C_8mimBr, by increasing the solute concentration, both the number, the average size and diversity (polydispersivity) of aggregates increase. However, again as in $C_{10}mim^+$ based systems, there is no signs of percolation, since even for the highest concentration (corresponding to 6000 mM, almost reaching the gel limit) an aggregate comprising all the solutes molecules in the simulation box was not observed.

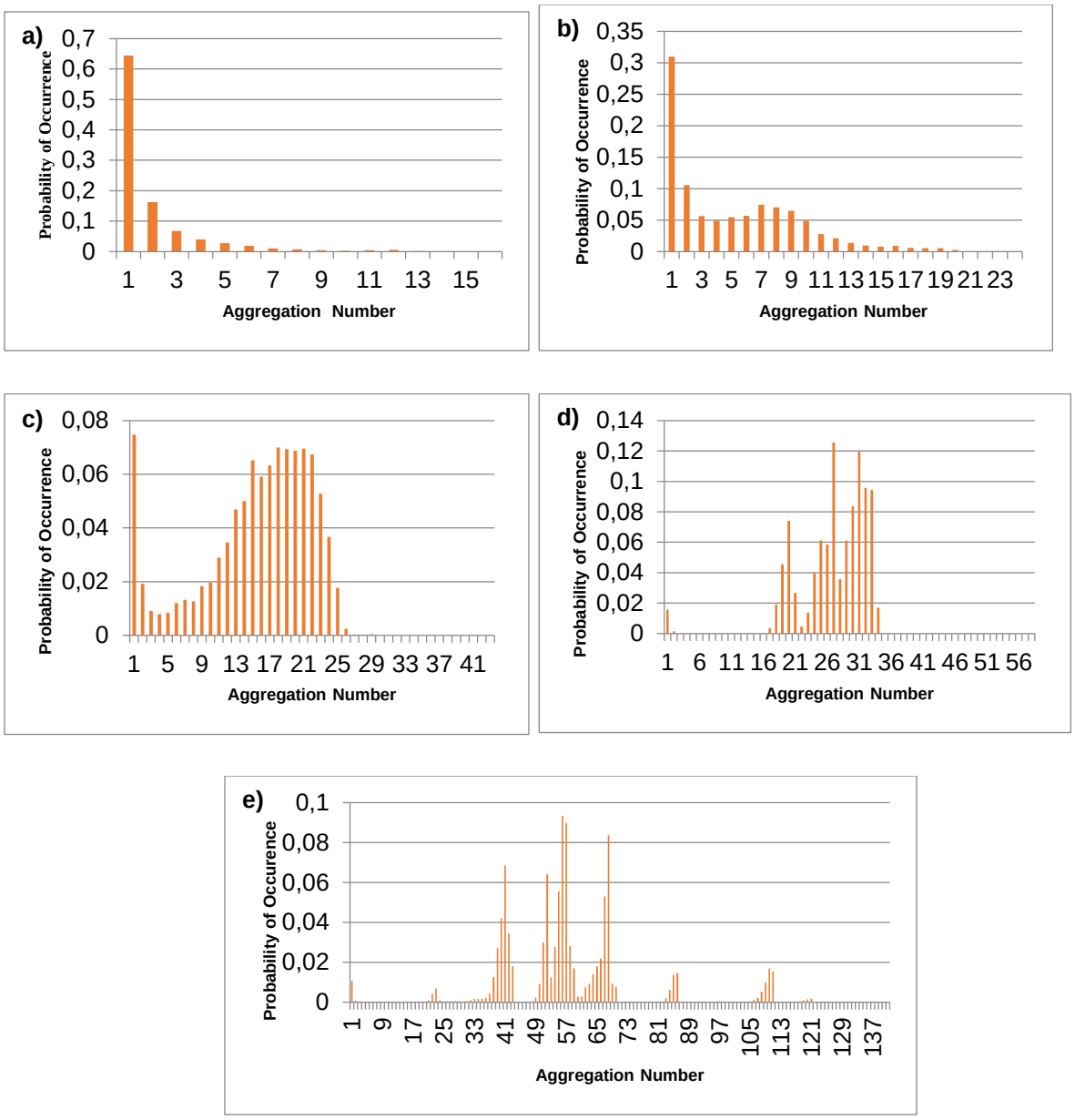

Fig 3.19. Aggregate analysis of C_8mimCl+H2O with all concentrations (a) 0.0067, (b) 0.012, (c) 0.0296, (d) 0.06, (e) 0.1

The aggregate analysis for the system C_{12}mimCl+H_2O is shown in figure 3.20 and some characteristics quite different from the other systems can be detected. Some aggregates are observed at the lowest concentrations competing with isolated molecules. The polydisperse character of the system is observed at a lower concentration (x_{IL} = 0.018) than for $C_{10}mim^+$ based mixtures and reinforced as the solute mole fraction increases to x_{IL} = 0.032. Surprisingly and unlike the previous systems, C_{12}mimCl+H_2O seems to tend to a monodisperse character at the highest concentration studied (x_{IL} = 0.058), as the distribution

obtained, although showing various possible aggregate dimensions is highly peak around 57 molecules per aggregate.

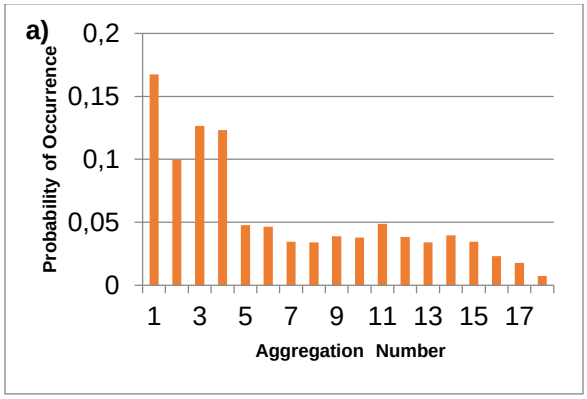

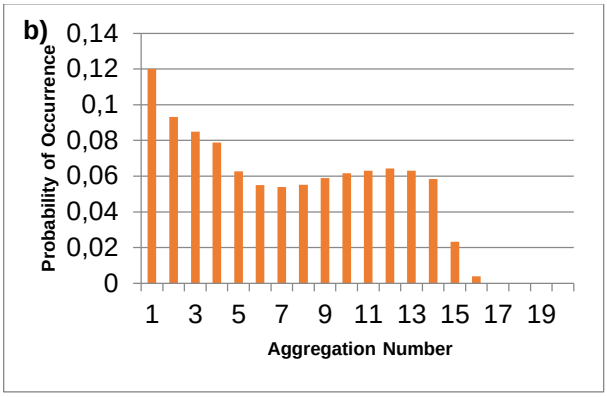

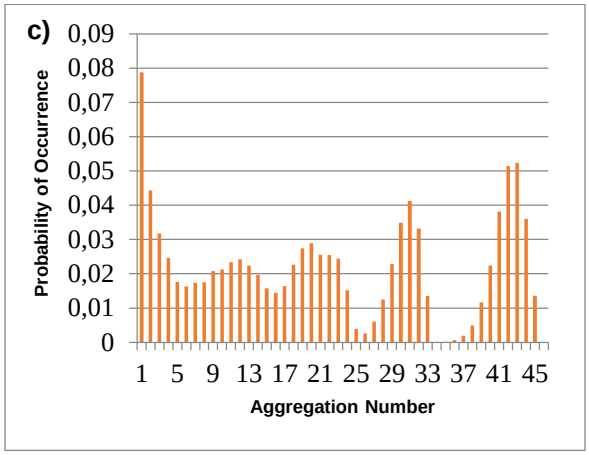

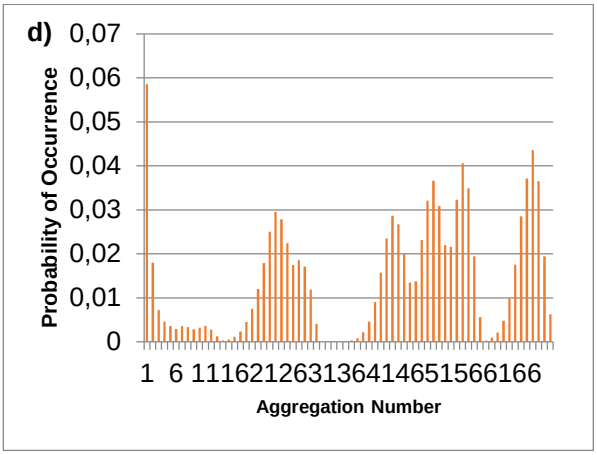

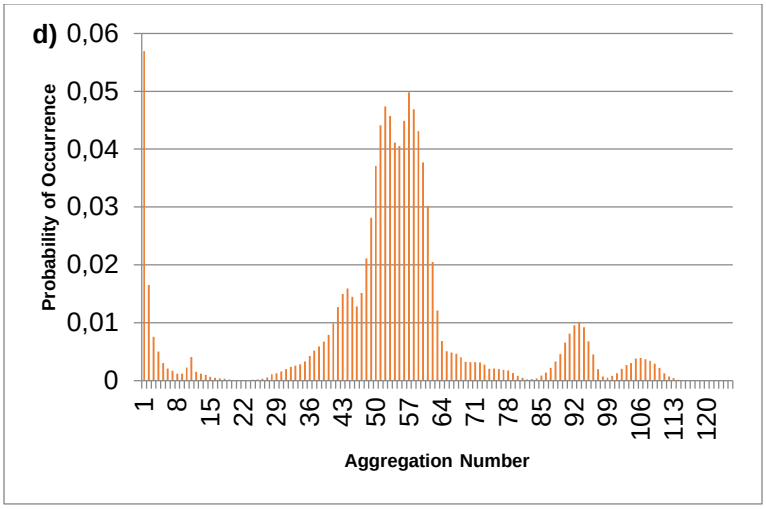

Fig 3.20. Aggregate analysis of C_{12}mimCl+H_2O with all concentrations (a) 0.005, (b) 0.009, (c) 0.018, (d) 0.032, (e) 0.058

Finally, the aggregate analysis for C_{10}mimNO_3+H_2O is shown in figure 3.21 and the results are quite similar to C_{10}mimCl and C_{10}mimBr with the predominance of isolated molecules at the lowest concentrations, the emergence of a monodisperse aggregate profile, the evolution to a distribution comprising two peaks and, for higher solute concentrations, a polydisperse distribution, confirming the increase in number, dimension and diversity of the solution aggregates as the solute concentration increases. The anion effect is only subtle and it seems that the aggregates tend to be smaller (with less molecules) for C_{10}mimNO_3+H_2O than for C_{10}mimCl+H_2O and these seem to be smaller than those for C_{10}mimBr+H_2O. The dimension order between the systems involving halides is expectable given the fact that the radius of bromide is larger than the radius of chloride. However, the position of C_{10}mimNO_3+H_2O seems to contradict the aggregate size obtained from DLS experiments. Both the anion size (in its bare or solvated form) and its tendency to dissolved in solution should be important to determine the size of the number of molecules of the aggregates.

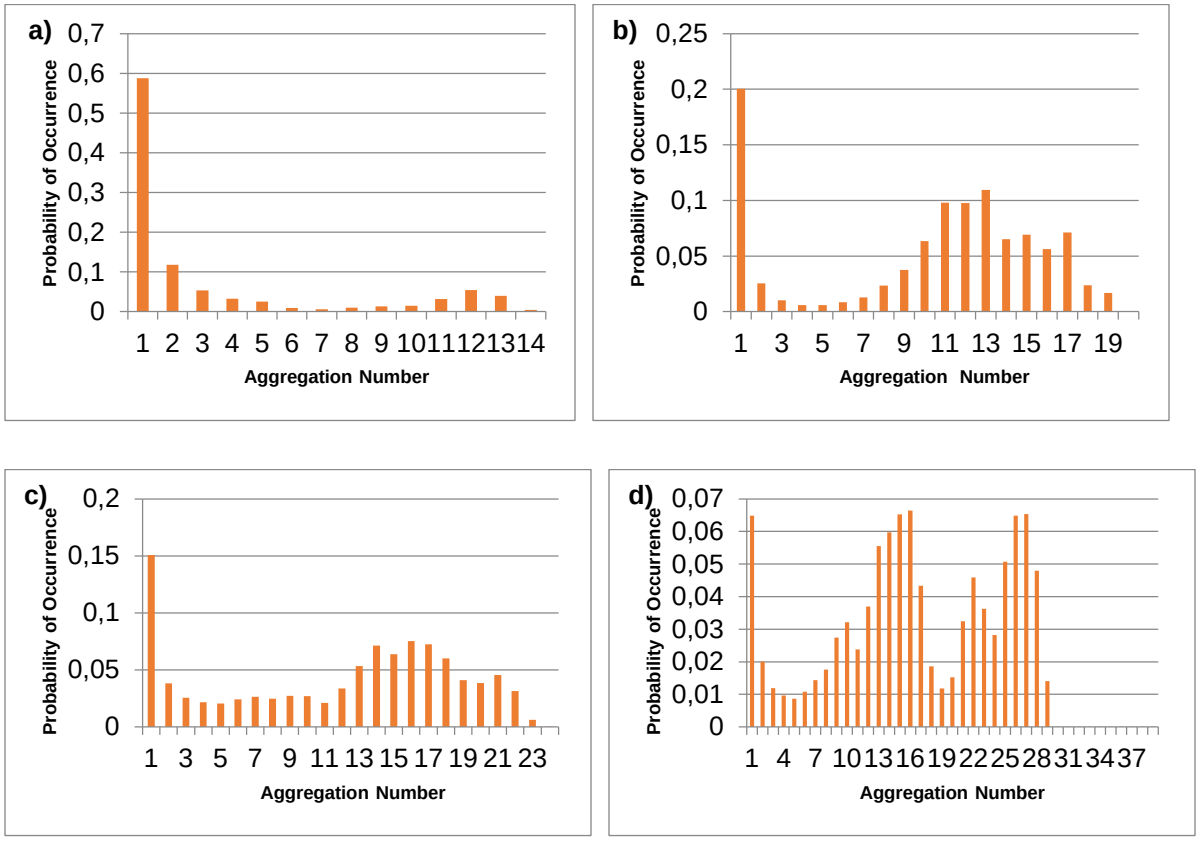

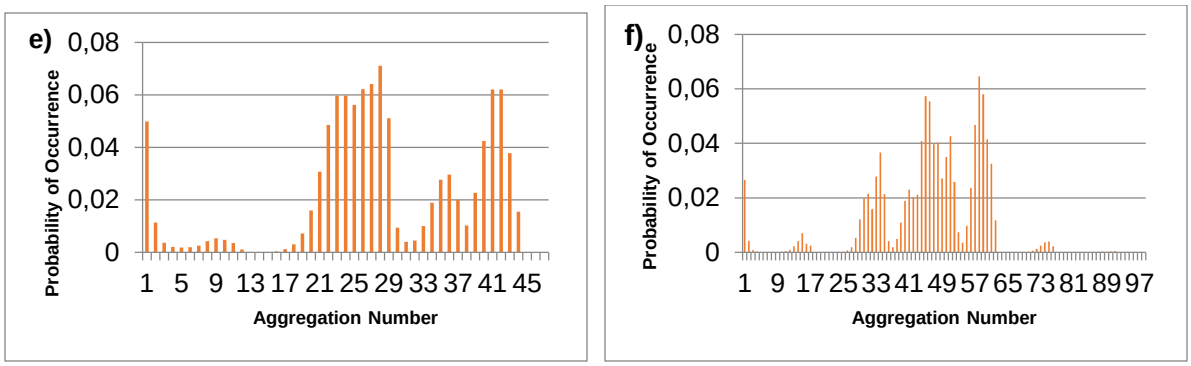

Fig 3.21. Aggregate analysis of C_{10}mimNO_3+H2O with all concentrations (a) 0.0025, (b) 0.005, (c) 0.009, (d) 0.018, (e) 0.032, (f) 0.058

By using Aggregate program, it was also possible to carry out a volumetric analysis of the solutions studied. In table 3.9 the aggregate size as a function of the number of molecules per aggregate is presented for solutions where aggregates other than isolated molecules were detected but were not clearly polydisperse. In this case, by size is meant the distance between the most distant pair of atoms in the aggregate.

In case of C_{10}mimCl+H_2O system, the aggregate analysis shows that one type of aggregates for moderate concentrations –500 mM (x_{IL} = 0.009) and 1000mM (x_{IL} = 0.018) – before the system become polydisperse, contains around 12-13 molecules (the aggregate number of the other one is approximately twice the former and tends to increase with concentration). Using the volumetric analysis (table 3.9) this corresponds to aggregate sizes between 1.734 and 1.778 nm (depending on the concentration). As it was seen above, the average diameter of the aggregates for this system obtained by DLS was between 1.458 and 1.212 for the same concentration range. The simulation values are higher than the experimental ones but not so much higher, especially considering the different concepts involved: DLS experimental results give the diameter of an equivalent sphere with the same volume as the aggregate and the size obtained by this volumetric analysis on the simulation data is the distance between the most distant atoms in the aggregate. These two values should be different provided that the aggregates present significant deviations to sphericity, which is probably the case, and the maximum distance between atoms is expected to be larger than the hydrodynamic diameter. We can conclude that there is a close relation between experimental and simulation results and the simulation is able to capture the formation of aggregates of one particular diameter. These kind of judgement of finding relation between experimental and theoretical values for higher concentrations are very difficult because of complex aggregate system.

For C_{10}mimBr+H_2O at the same of concentrations as the preceding system, the most prevalent type of aggregates has an aggregation number of 18-19 molecules (before becoming polydisperse), which corresponds to a size between 2.043 nm and 2.066 nm. Due to the high dispersion of the results, we should compare these values with the average diameter of the aggregates over the whole concentration range, which was found to be 2.266 nm. Experimental and simulated values are very close to each other, considering the characteristic dispersion of both determinations, despite their relative magnitude is the opposite of the expected. Again, the values correspond with a deviation in part explained by the concept difference.

In the case of C_8mimCl+H_2O, the maximum number for aggregation is 20 molecules for a solute concentration of 1640 mM (x_{IL} = 0.0296), a solution with monodisperse character. The average DLS value 1.585 nm (average because the dispersion of the values) can be compared with the simulation value of 2.059 nm, obtained by volumetric analysis. Again, the values correspond being the deviation explained in part by the concept difference. . For C_8mimBr with 1500mM (x_{IL} = 0.0296) concentration having maximum aggregation number was 19, which corresponds to a size of 2.008 nm, while the experimental diameter obtained using DLD was 1.935nm which is close to and smaller than the simulation value.

For C_{10}mimNO_3+H_2O the most relevant peak of aggregate analysis has a maximum aggregation number of 16 (at x_{IL} = 0.009), corresponding to a size of 1.939 nm and DLS value for this particular concentration was 1.472 nm, but a value of 2.089 nm is obtained as an average of all the concentrations, confirming the closeness between experimental and simulation results. The C_{12}mimCl+H_2O system becomes polydisperse at low concentrations and, at the emergence of aggregate formation, a maximum aggregation number of 12 is obtained for the concentration of 500 mM (x_{IL} = 0.009), which corresponds to a size of 1.856 nm, while the DLS size value is 1.143 nm for this particular concentration, which is the largest deviation obtained between experimental and simulation results.

Table 3.9. Aggregate size as Function of the Number of Molecules per Aggregate for Selected Solutions for all the Systems.

C_{10}mimCl+H_2O				**C_{10}mimBr+H_2O**			
X_{IL} = 0.009		**X_{IL} = 0.018**		**X_{IL} = 0.009**		**X_{IL} = 0.018**	
Number of molecules per aggregate	**Size of the aggregate, *D* / Å**	**Number of molecules per aggregate**	**Size of the aggregate, *D* / Å**	**Number of molecules per aggregate**	**Size of the aggregate, *D* / Å**	**Number of molecules per aggregate**	**Size of the aggregate, *D* / Å**
1	0	1	0	1	0	1	0

2	5.24732	2	5.13202	2	5.34119	2	5.17674
3	8.25082	3	8.13635	3	8.3619	3	8.17947
4	10.51858	4	10.34829	4	10.79063	4	10.42003
5	11.97733	5	11.99591	5	12.08472	5	11.94567
6	12.99741	6	12.99813	6	13.0954	6	13.10824
7	13.96799	7	13.96949	7	14.09888	7	13.96552
8	14.69486	8	14.58575	8	14.8365	8	14.66991
9	15.4145	9	15.32243	9	15.51443	9	15.46573
10	16.11081	10	15.96224	10	16.26628	10	16.05233
11	16.82389	11	16.59649	11	16.80786	11	16.54722
12	17.3372	12	17.15344	12	17.93566	12	17.23241
13	18.06426	13	17.77656	13	18.32638	13	17.78595
14	18.73664	14	18.2211	14	18.42334	14	18.37731
15	19.05095	15	18.64596	15	18.92594	15	18.89625
16	19.52224	16	19.45063	16	19.52108	16	19.44969
17	20.29466	17	19.88639	17	20.05682	17	19.82333
18	20.27307	18	20.14307	18	20.42767	18	20.2182
19	20.70092	19	20.41623	19	20.65776	19	20.66071
20	21.05453	20	20.76056	20	21.35435	20	21.04782
21	21.30858	21	21.57573	21	26.5388	21	21.47361
22	22.12884	22	21.81225	22	34.79042	22	22.30021
23	38.86323	23	22.25577	23	34.80162	23	25.59299
24	38.99803	24	22.58273	25	67.20172	24	23.85096
26	36.74379	25	22.96266	27	69.70148	25	23.74587
28	35.53505	26	23.21856			26	23.42098
		27	23.43946			27	23.60585
		28	23.32706			28	24.00368
		29	43.545			29	24.52905
		30	43.48976			30	35.68264
		31	43.67442			31	40.23939
		32	44.06244			32	36.85671
		33	45.8408			33	40.47204
		41	46.88051			34	44.69655
		43	48.048			35	43.0709
		44	46.39421			36	43.18985
$C_8mimCl+H_2O$		**$C_8mimBr+H_2O$**		**$C_{10}mimNO_3+H_2O$**		**$C_{12}mimCl+H_2O$**	
X_{IL} = 0.0296		**X_{IL} = 0.0296**		**X_{IL} = 0.009**		**X_{IL} = 0.009**	
Number of	**Size of the aggregate, *D* / Å**	**Number of molecules**	**Size of the aggregate, *D* /**	**Number of molecules**	**Size of the aggregate, *D***	**Number of molecules per**	**Size of the aggregate, *D* /**

molecules per aggregate		per aggregate	Å	per aggregate	/ Å	aggregate	Å
1	0	1	0	1	0	1	0
2	5.15102	2	5.21291	2	5.20432	2	5.24459
3	7.72705	3	7.82275	3	8.153	3	8.47485
4	9.53612	4	9.53329	4	10.29192	4	10.52922
5	10.88916	5	10.88315	5	11.80567	5	12.47027
6	11.81753	6	11.83712	6	12.87615	6	13.9815
7	12.73554	7	12.81599	7	13.91069	7	15.0508
8	13.74724	8	13.694	8	14.63003	8	15.9651
9	14.2561	9	14.34703	9	15.35308	9	16.65218
10	15.06687	10	14.95471	10	15.99805	10	17.41516
11	15.60207	11	15.66774	11	16.59001	11	18.04806
12	16.28661	12	16.4762	12	17.24994	12	18.56089
13	16.71389	13	16.91248	13	17.85359	13	19.14611
14	17.18735	14	17.54737	14	18.49422	14	19.51344
15	17.92411	15	18.1616	15	18.99423	15	19.97973
16	18.52843	16	18.65847	16	19.39203	16	20.68746
17	19.0089	17	19.04362	17	19.7142	17	31.34526
18	19.50396	18	19.50682	18	20.04332	19	36.37871
19	19.99509	19	20.07524	19	20.47469	20	37.14694
20	20.58728	20	20.63299	20	20.99894	22	40.23968
21	21.33416	21	21.15698	21	21.33631		
22	21.52011	22	21.48529	22	21.43682		
23	21.79798	23	22.56874	23	21.97129		
24	21.89427	24	23.15268	24	24.19002		
25	22.5598	25	24.07393				
26	26.12708	26	23.83925				
27	33.33157	27	24.90423				
28	34.62898	28	25.12721				
29	33.5755	29	33.7687				
30	37.21166	30	36.60676				
31	39.25722	31	40.51156				
32	43.62878	32	40.04601				
33	57.94612	33	40.61034				
34	60.56217	34	43.07922				
35	71.50765	35	40.04025				
36	71.74128	36	56.23353				
37	70.11931	37	72.0203				
38	50.91519	38	58.01732				
40	72.25571	40	41.07563				

41 43 44 45	56.01881 41.61959 45.81402 44.48251	41	42.70488				

3.3.2. Radial Distribution Function

Radial distribution functions (rdf) have been calculated for all the systems and all the concentrations from the final trajectory files obtained in the simulation protocol. rdf were obtained using different species (water, chloride, bromide, nitrate) and IL moieties (head and tail) as reference sites on a center of gravity basis. The hydrogen atom connected to the carbon between to nitrogen atoms in the imidazolium ring was also used as reference site. The definition of the moieties "head" (essentially the imidazolium ring) and "tail" (alkyl side chain), as well as the hydrogen atom mentioned above, are explained in figure 3.22.

The rdfs for system C_{10}mimCl+H_2O are shown in the figure 3.23, 3.24 and 3.25 for different groups of pairs.

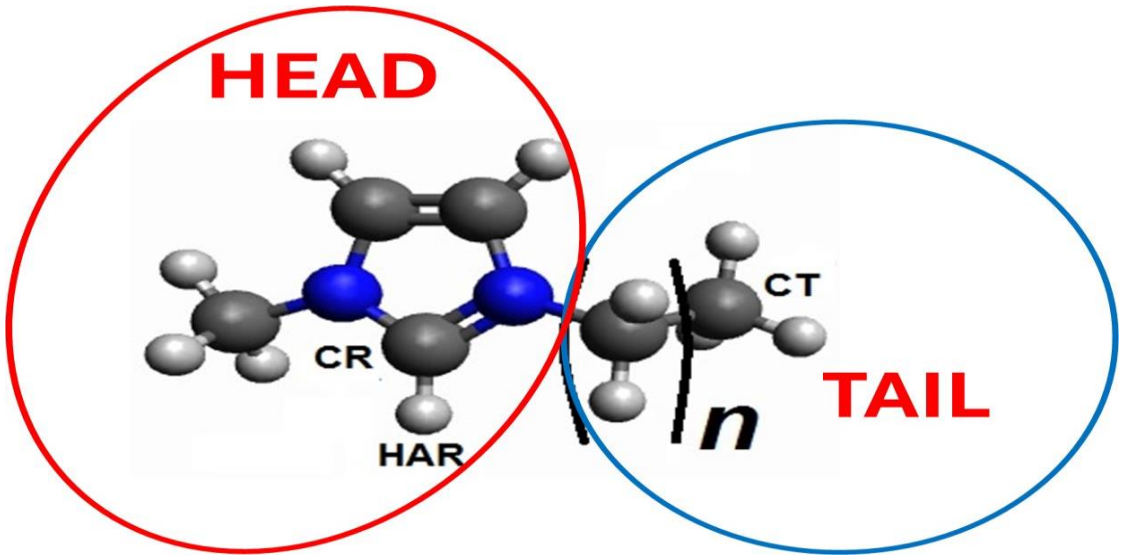

Fig. 3.22 Scheme showing a generic 1-alkyl-3-methyl imidazolium cation

In figure 3.23 rdfs involving head moiety of IL are presented and some important observations should be stressed. The Head-head interaction is increasingly intense as the concentration decreases and the same happens with head-tail interaction. Organic cations prefer each other in comparison with water and that is more obvious when fewer IL molecules exist in solution.

Head-Cl^- interaction [figure 3.23 b)] seems to be less intense than head-head, because of the freedom of the chloride anion which is more dissolved in water than sticked to the supramolecular aggregates. However, the first peak of rdf appears at lower distances than for head-head pair, meaning that, on average, cation head stays closer to the anion than to the cation itself and this can be explained by the charge of each moiety. The shoulder appearing in head-chloride rdf is probably due to more than one orientation of approaching of these two moieties. At low concentrations, the water molecules have strong interactions with chloride and this organizes the head and chloride in a more structured way and gives high values of rdf, but with the increase in concentration, water molecules decreases and the chloride anion shows more interactions with the hydrogen atoms of the imidazolium head and gives low rdf values due to micelle formation. At very high concentrations, the RDF peak intensity suddenly increases because the molecules self-assemble into more complex micelles, forming a denser head–Cl^- system with less water solvation.

The head-tail rdf [figure 3.23 c)] presents higher peaks than head-head rdf and also a considerable number of shoulders, which is an indication of a more intense interactions (because heads have the same charge sign) and the existence of aggregates with some disordered character.

In the case of head-water pair, the intensity of rdf peaks increase with the increasing concentration because the micelle becomes more densely packed with the hydrophobic tail inside and hydrophilic head outside shows more interaction with the water and the probability of water interaction with the head increases.

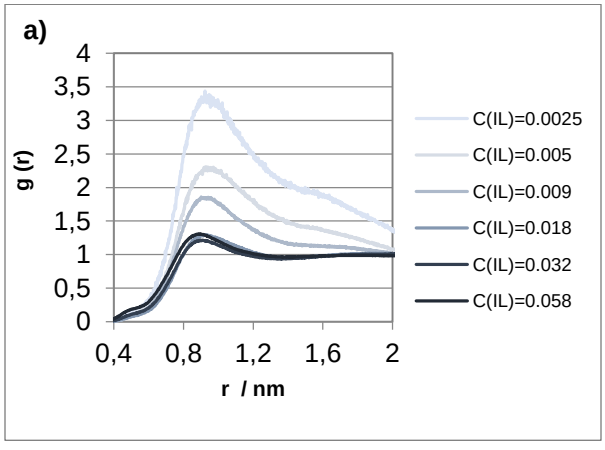

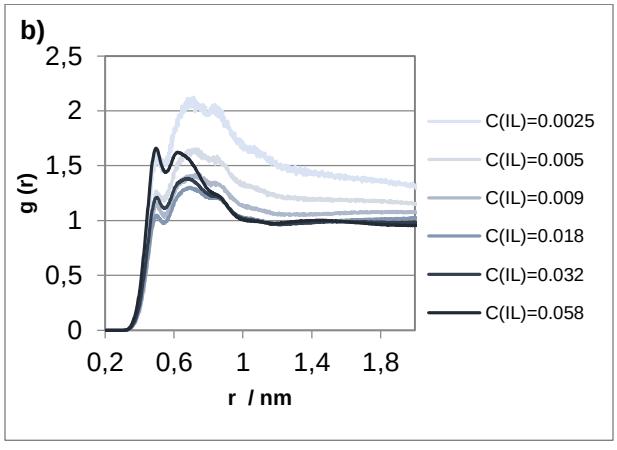

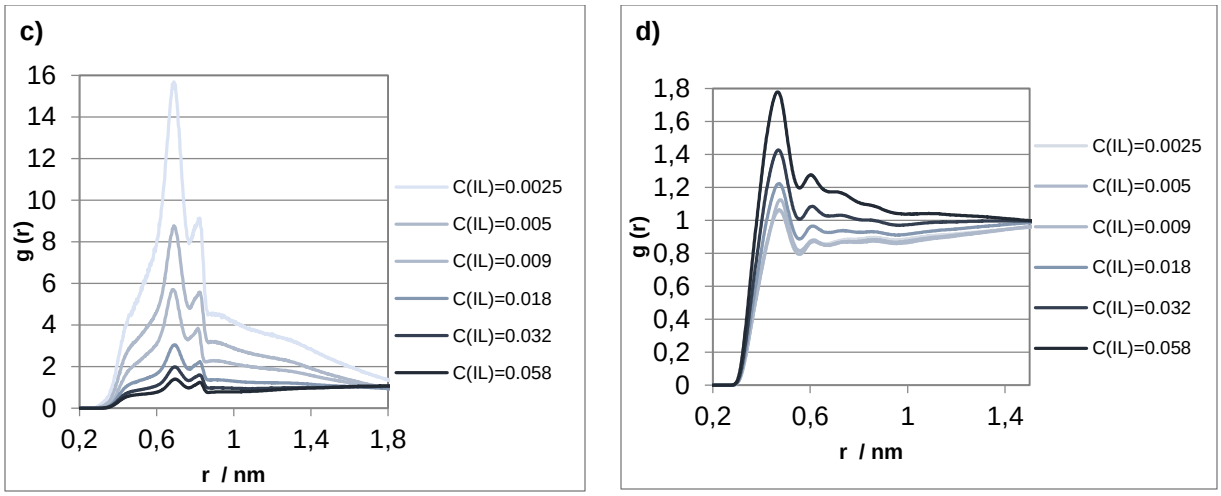

Fig 3.23. RDF for the system of C_{10}mimCl +H_2O with (a) Head-Head (b) Head-Cl (c) Head-Tail (d) Head-Water

The Cl^- - water (figure 3.24) interaction is much more intense and exerted at lower distances than Cl^- - Cl^- interaction, which means that chloride ions are mainly dissolved in water. The intensity of the peaks for both pairs increases as the concentration increases, especially Cl^- - Cl^-, which is a further indication of the affinity between chloride and water. The average distance between Cl^- and the hydrogen bonded to the ring carbon between the two nitrogen atoms (code HAR), which is less than 0.3 nm, is an indication of the existence of a hydrogen between these two atoms.

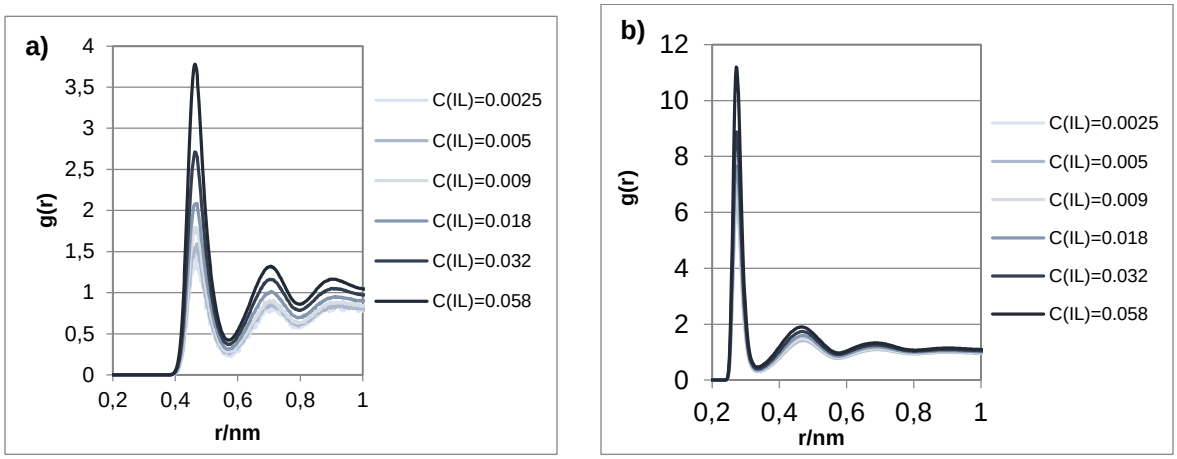

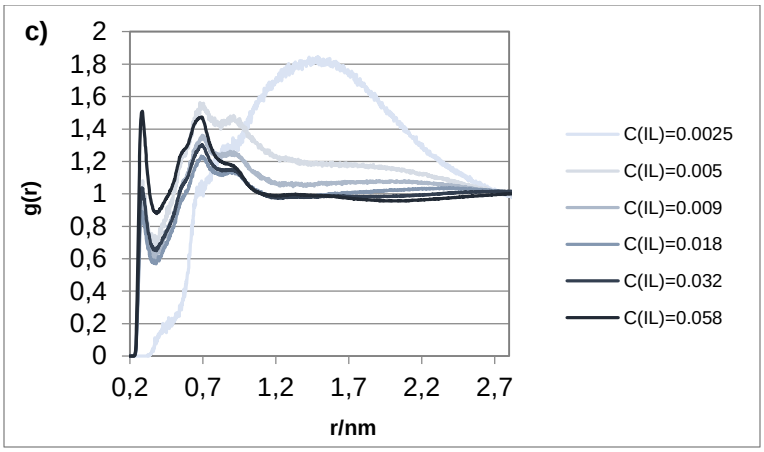

Fig 3.24. RDF for the system of C_{10}mimCl +H_2O with (a) Cl-Cl (b) Cl-Water (c) Cl-HAR

The high intensity of the first peak for the tail-tail pair (figure 3.25), together with its concentration dependence (again the intensity decreasing with the increasing concentration) and the fact the intensity of the tail-water rdf is below 1 is an indication of the mutual antipathy between the tail of the cation and water, being the driving force for the formation of micelles.

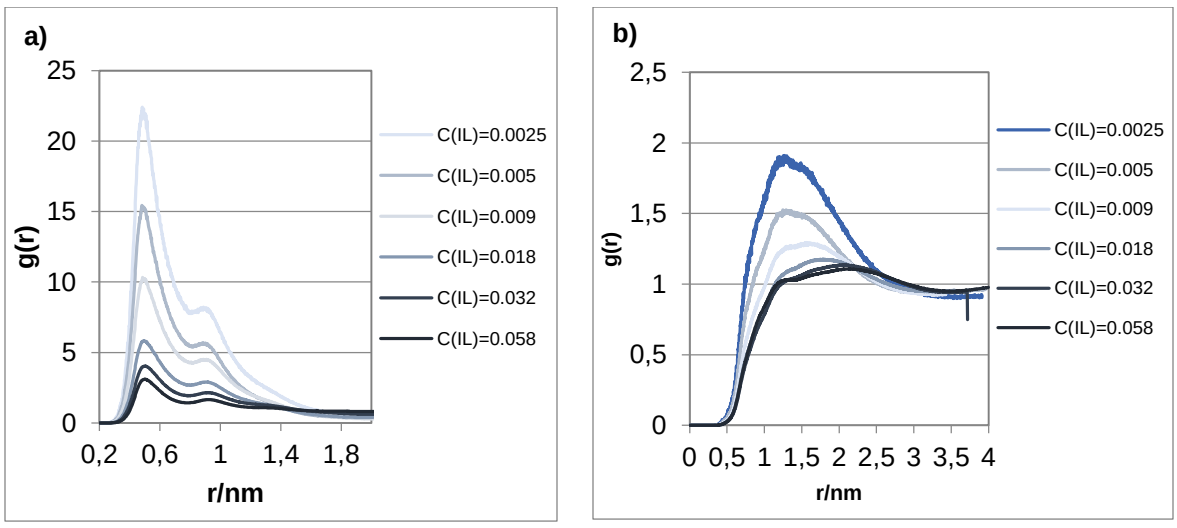

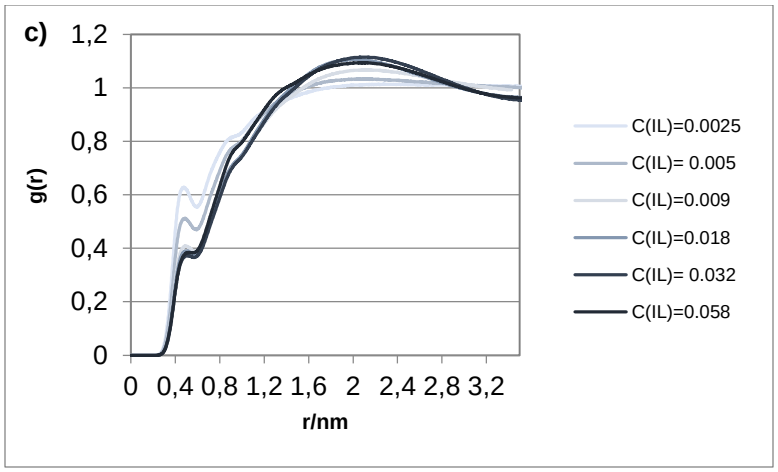

Fig 3.25 RDF for the system of C_{10}mimCl +H_2O with (a) Tail-Tail (b) Tail-Cl (c) Tail-Water

The rdf graphs for C_{10}mimBr+H_2O are shown in figures 3.26, 3.27, and 3.28.

The peaks of the head-head rdf for C_{10}mimBr+H_2O [figure 3.26 a)] are less intense than those for C_{10}mimCl+H_2O (which may indicate the prevalence of more loose aggregate), but the average distance of this interaction is nearly the same, around 0.8nm. On the other hand, the rdf peaks for head-Br^- interaction [figure 3.26 b)] are sharper than those for head-Cl^- and also less insensitive to the solute concentration. The looser character of the C_{10}mimBr aggregates is confirmed by the lower intensity of the respective rdf peaks for head-tail interaction, compared to the previous system.

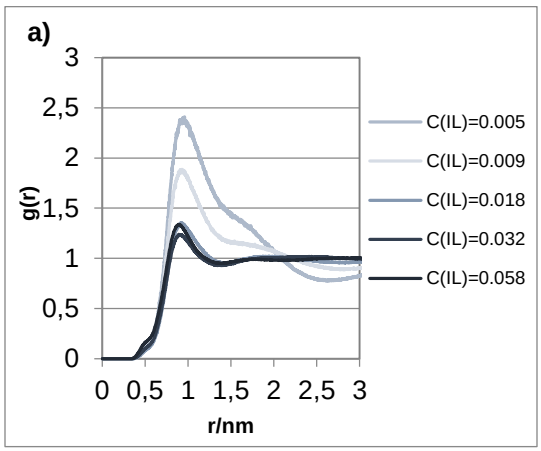

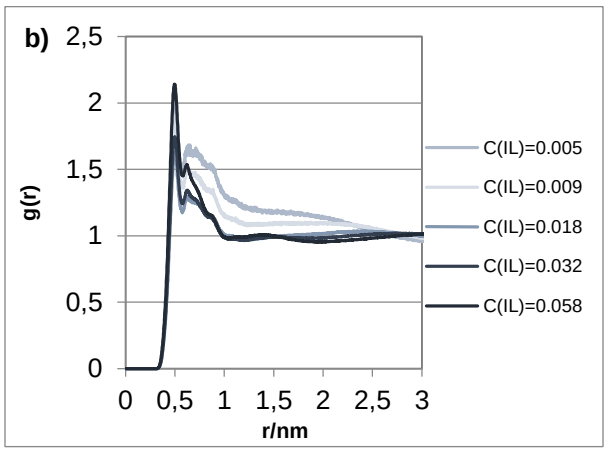

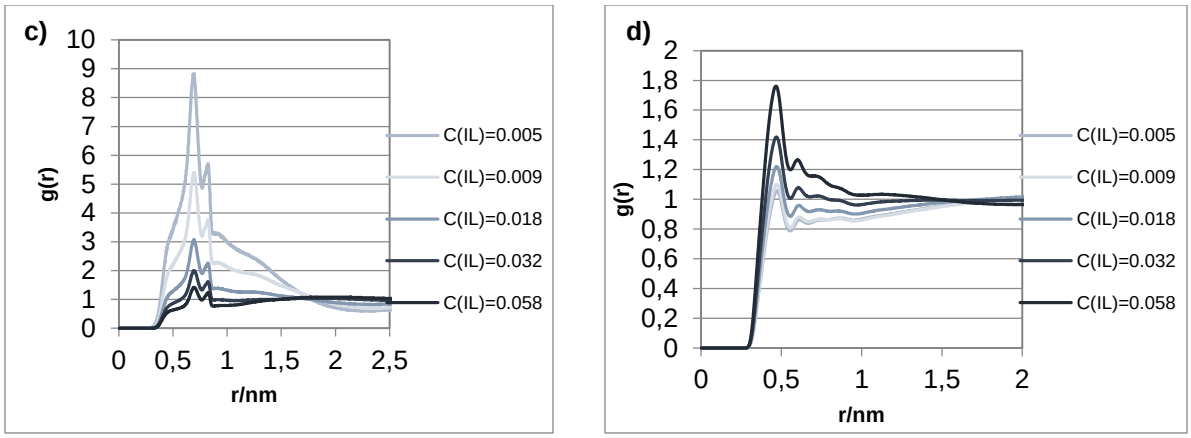

Fig 3.26. RDF for the system of C_{10}mimBr +H_2O with (a) Head-Head (b) Head-Br (c) Head-Tail (d) Head-Water

The rdf involving bromide (figure 3.27) confirm the affinity of halide anion for water in this kind of systems. However, both Br⁻Br⁻ and Br⁻water pairs present less intense peaks in their rdfs than in the case of Cl^-, which is probably due to the higher charge density of the chloride anion. Interestingly, the interaction Br^--HAR seems to be stronger than the Cl^--HAR (and exerted at almost the same distance). This is possibly because of the larger size of bromide and its more polarizability and at high concentration more number of atoms of bromide surrounds the HAR showing more than one peak.

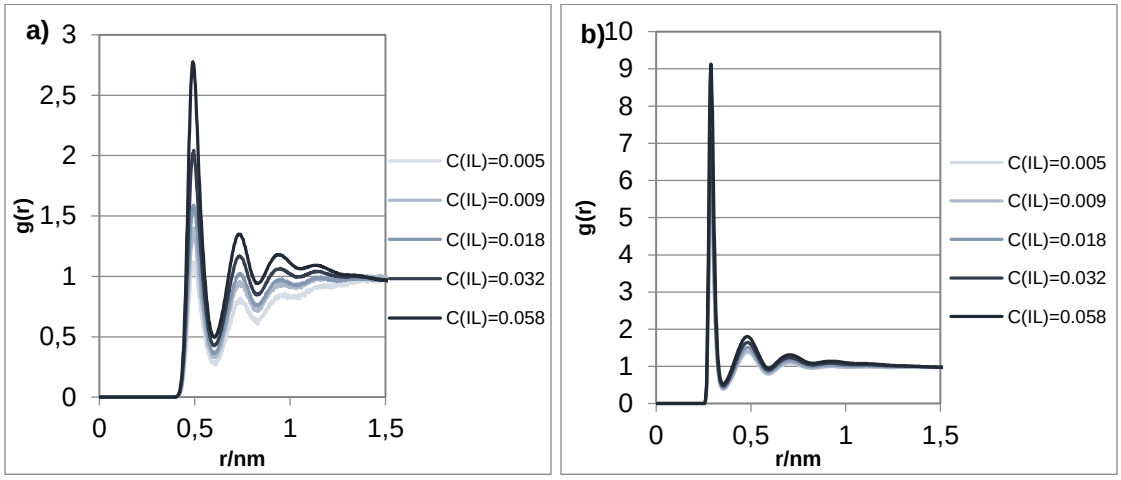

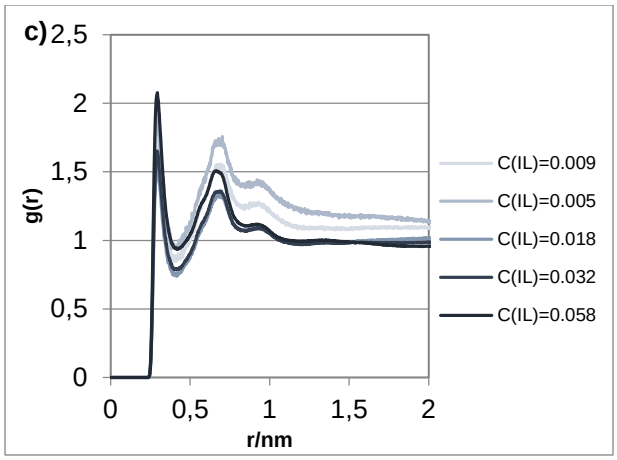

Fig 3.27. RDF for the system of C_{10}mimBr +H_2O with (a) Br-Br (b) Br-Water (c) Br-HAR

A second confirmation of the looser character of the aggregates with C_{10}mimBr is the less intense peaks of the tail-tail rdf compared to C_{10}mimCl (figure 3.28). And the Br^- tail rdf seems to indicate a repulsion between bromide and the alkyl chain of the cation, unlike it is observed for C_{10}mimCl +H_2O system. Bromide seems to be more connected to the cation contributing to the disorder of the aggregates, while chloride seems to be more connected to the water, being also around the alkyl part of the cation.

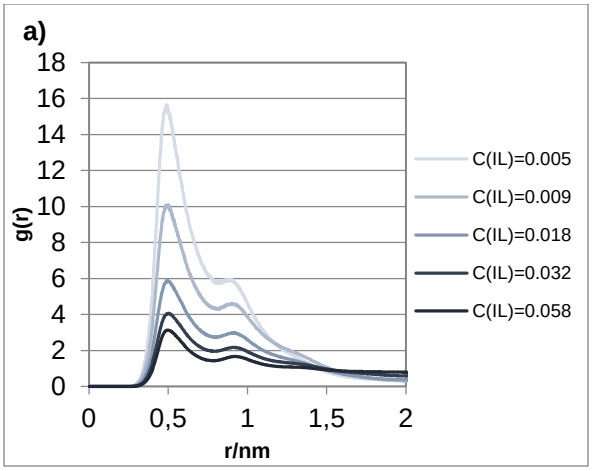

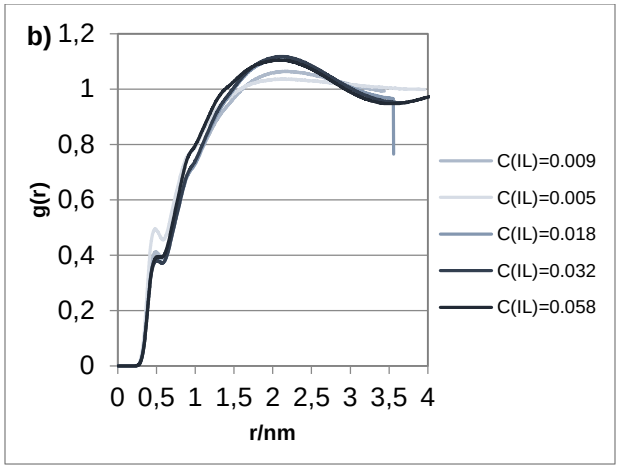

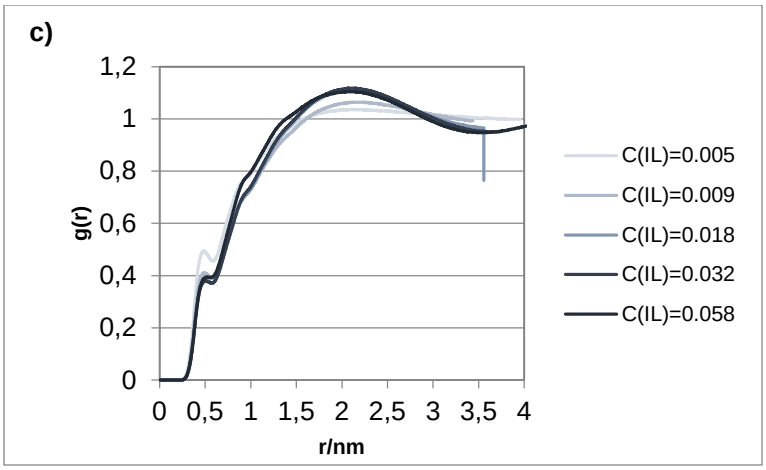

Fig 3.28. RDF for the system of C_{10}mimBr +H_2O with (a) Tail-Tail (b) Tail-Br(c) Tail-Water

RDFs for the C_8mimCl +H_2O system are shown in figures 3.29, 3.30 and 3.31. The head-head rdf [figure 3.29 a)] presents less intense peaks than the system involving $C_{10}mim^+$ cation and failing to shown the same trend with solute concentration. This can be due to the fact that C_8mimCl is not so prone to form micelles as C_{10}mimCl, given its shorter alkyl chain. This fact can be also the reason for the less intensity of peaks from the head-tail interaction [figure 3.29 c)] and especially for the lower diversity of approaching orientations within the pair.

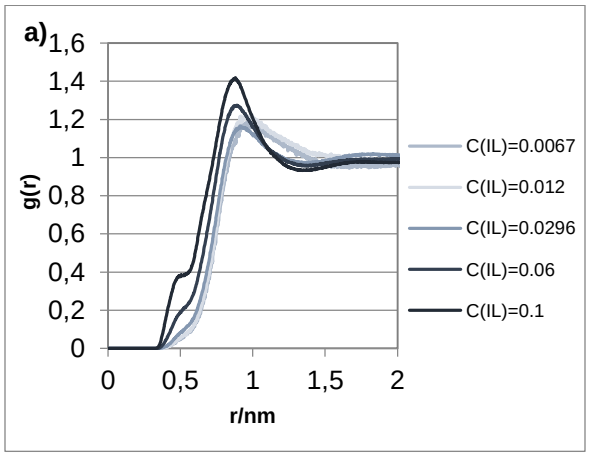

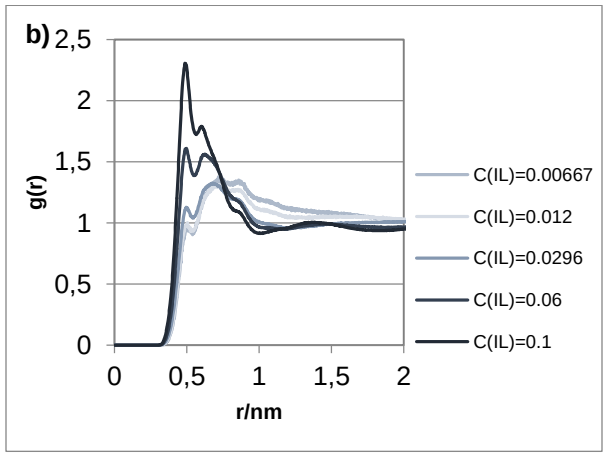

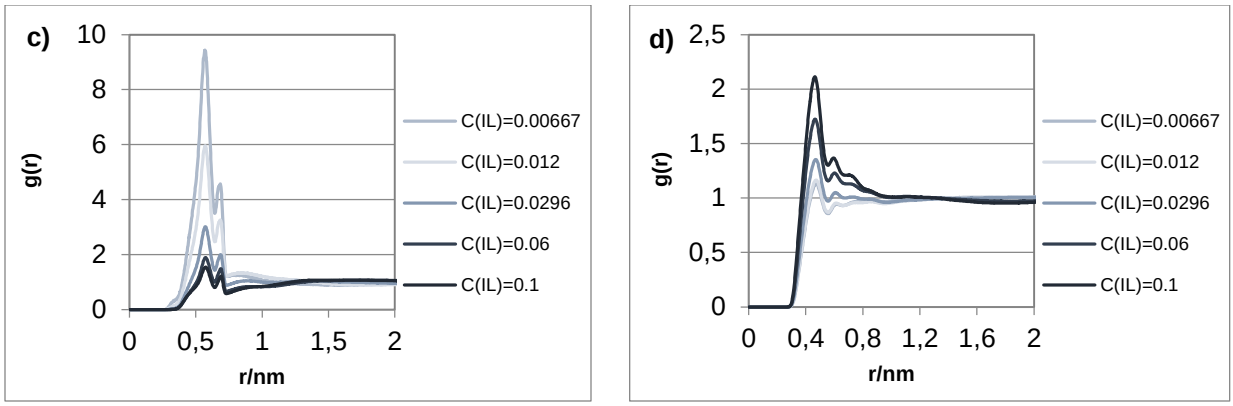

Fig 3.29. RDF for the system of C_8mimCl +H_2O with (a) Head-Head (b) Head-Cl (c) Head-Tail (d) Head-Water

Interestingly, both the Cl^-Cl^- and Cl^-water interaction (figure 3.30) seems to be stronger for C_8mimCl +H_2O system than for C_{10}mimCl +H_2O. Being shorter, the C_8mim^+ alkyl chain allows all the components of the mixture to be more soluble in water instead of being stuck at the surface of the aggregates. Under these conditions, isolated molecules and ionic pairs are more probable to occur, allowing an enhanced interaction between chloride and HAR hydrogen of the cation, as it is visible in figure 3.30 c).

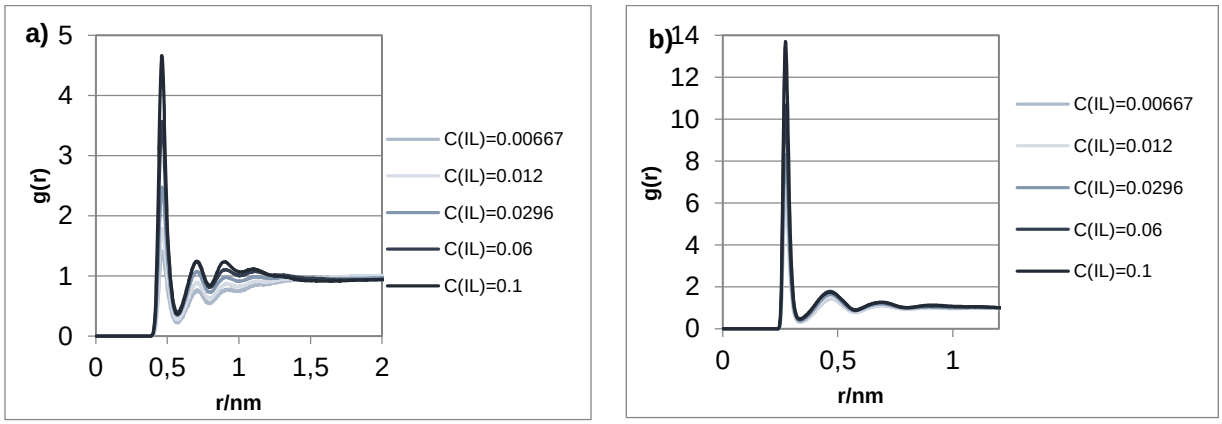

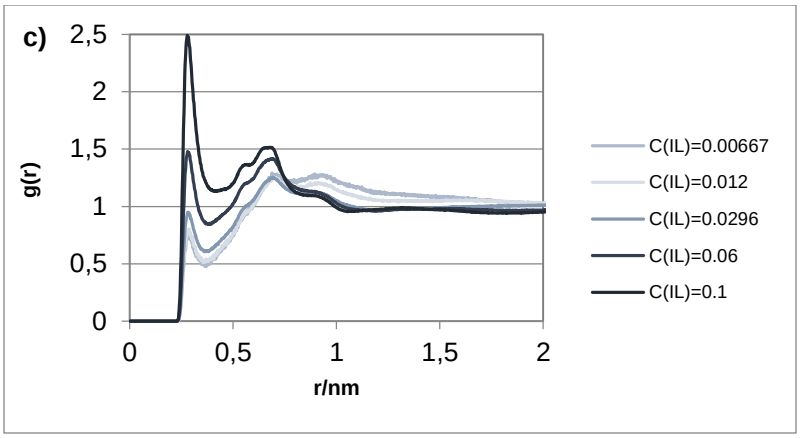

Fig 3.30. RDF for the system of C_8mimCl +H_2O with (a) Cl-Cl (b) Cl-Water (c) Cl-HAR

The low probability of the occurrence of large aggregates in the C_8mimCl +H_2O is confirmed by the less intense peaks in the tail-tail pair [figure 3.31 a)] compared with C_{10}mimCl +H_2O system.

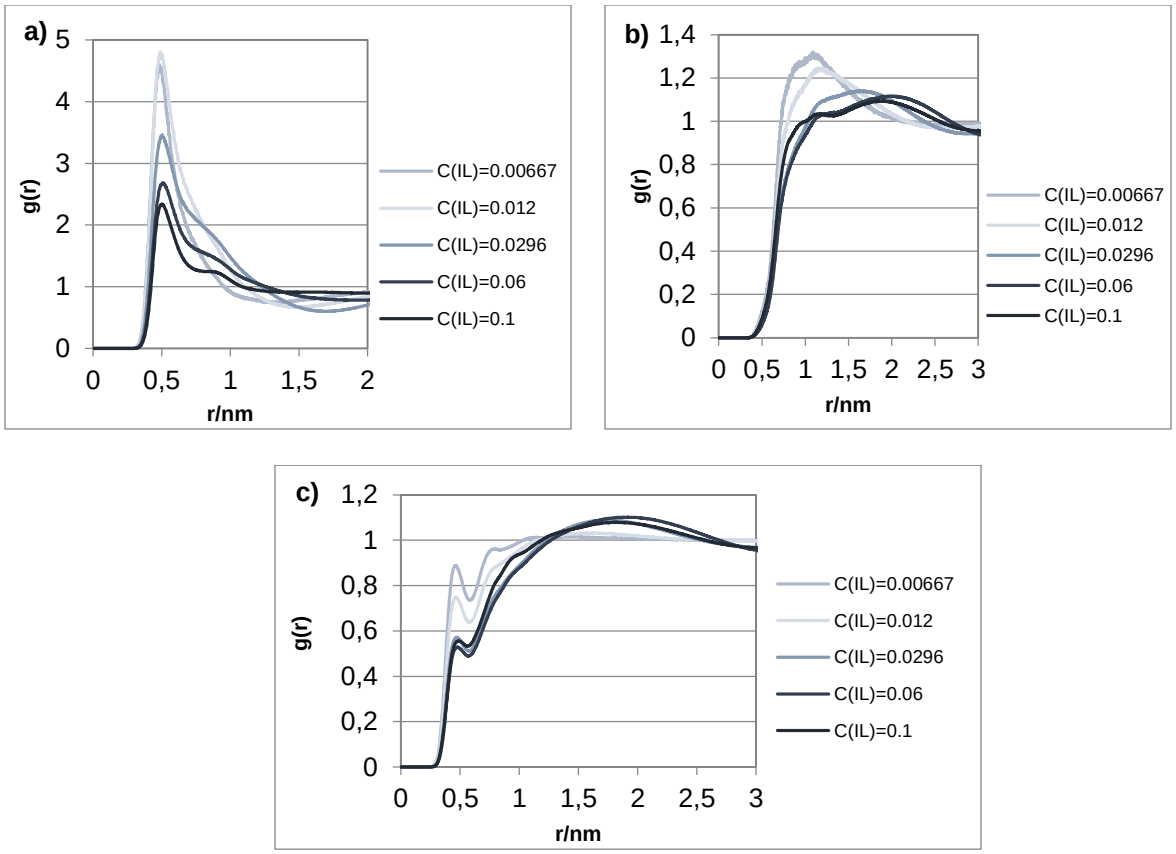

Fig 3.31. RDF for the system of C_8mimCl +H_2O with (a) Tail-Tail (b) Tail-Cl (c) Tail-Water

The rdfs for the C_8mimBr +H_2O are shown in the figures 3.32, 3.33 and 3.34. They resemble, in general, those for C_{10}mimBr. The most interesting characteristic is the fact that the halide-HAR is even stronger than for the systems C_8mimCl and C_{10}mimBr because the joint effect of a shorter alkyl chain and a larger anion.

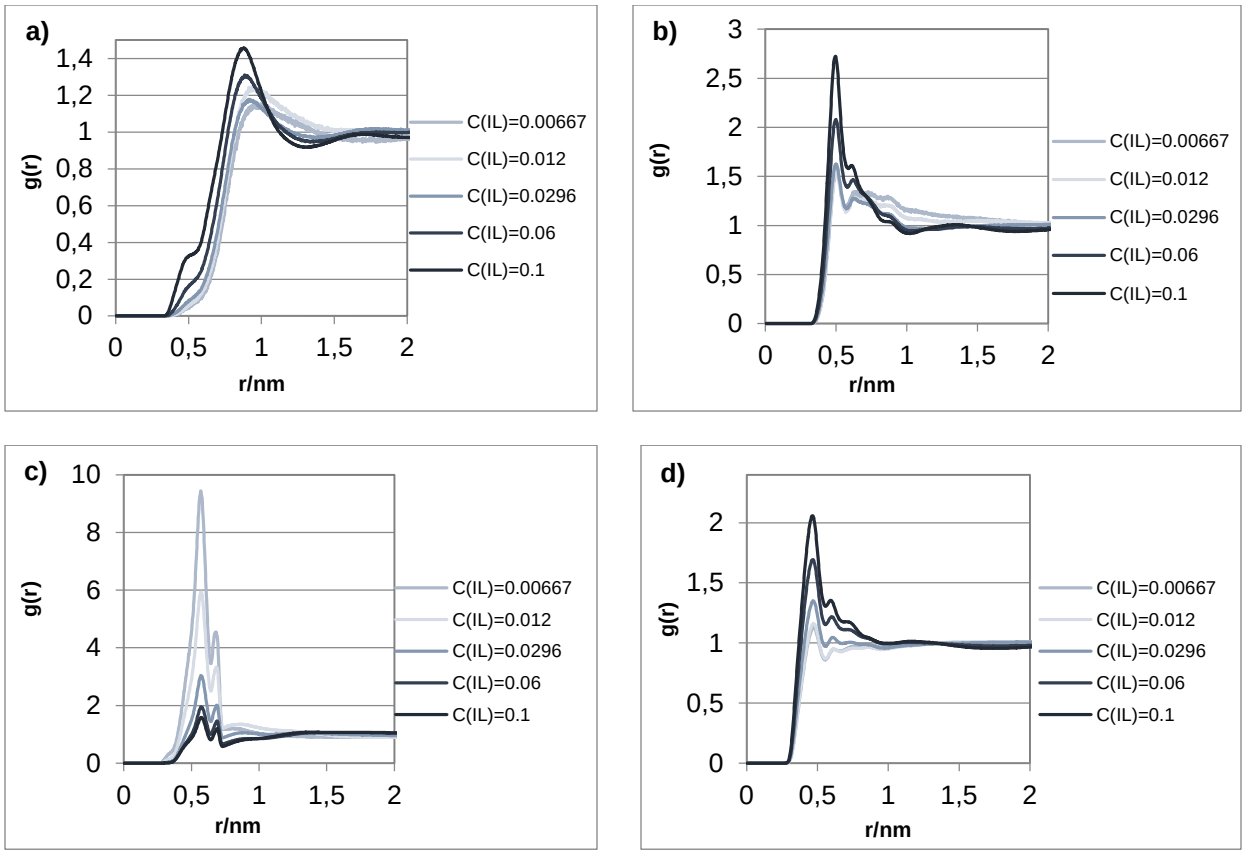

Fig 3.32. RDF for the system of C_8mimBr +H_2O with (a) Head-Head (b) Head-Br (c) Head-Tail (d) Head-Water

The bromide shows the clear and sharper peaks in fig 3.33 with different molecules but comparing it with C_8mimCl its rdf values are lower with relatively same reason of size and polarizability.

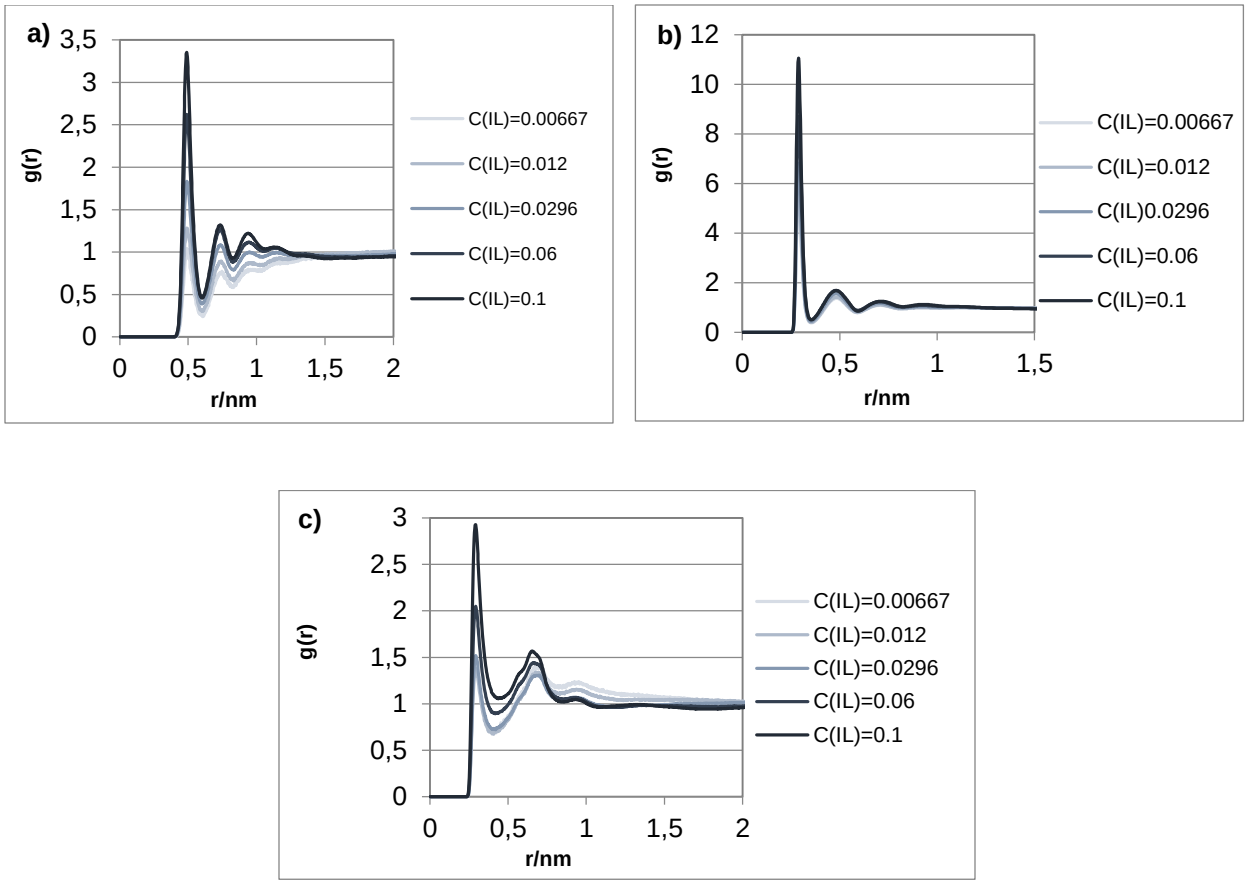

Fig 3.33. RDF for the system of C_8mimBr +H_2O with (a) Br-Br (b) Br-Water (c) Br-HAR

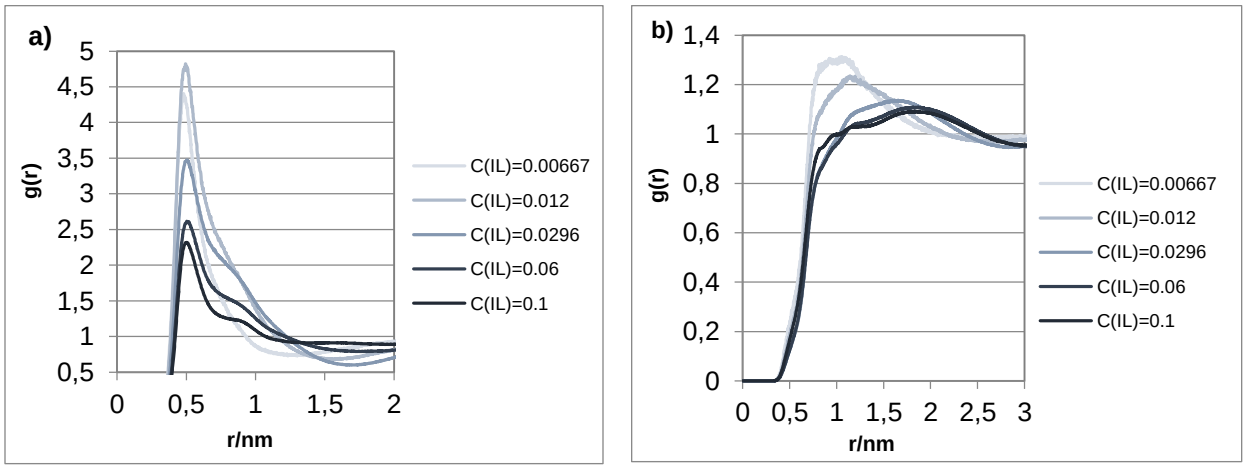

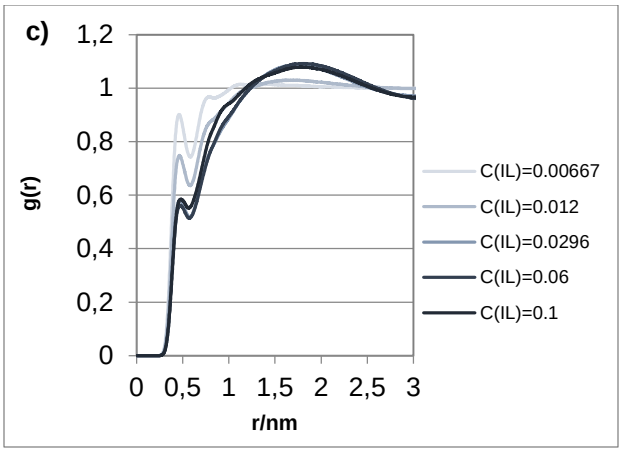

Fig 3.34. RDF for the system of C_8mimBr +H_2O with (a) Tail-Tail (b) Tail-Br(c) Tail-Water

Rdfs for the C_{10}mimNO_3+H_2O system are shown in figures 3.35, 3.36 and 3.37. A concentration effect in the head-head, head-anion and head-tail pairs similar to the C_{10}mimCl system was found (figure 3.35).

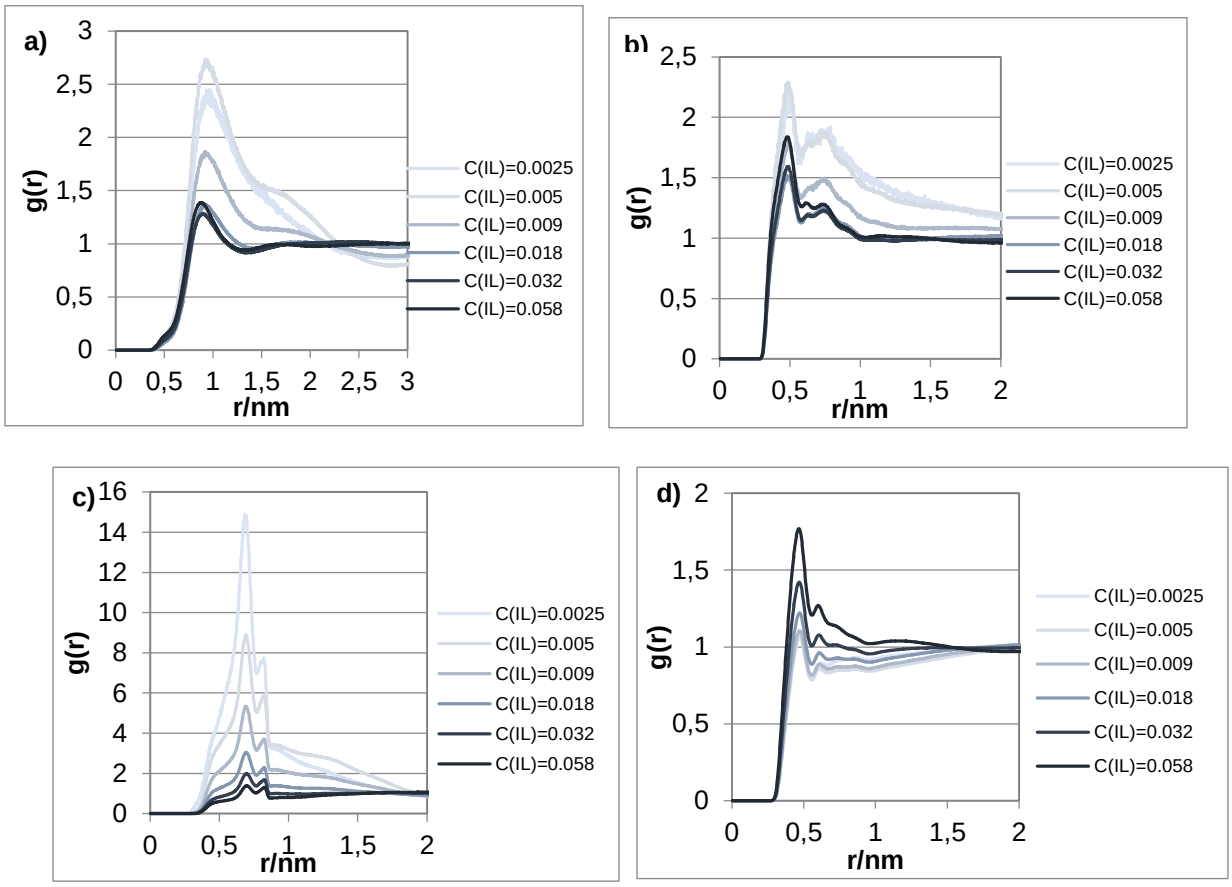

Fig 3.35. RDF for the system of C_{10}mimNO_3 +H_2O with (a) Head-Head (b) Head-NO_3 (c) Head-Tail (d) Head-Water

In fact, the rdfs involving the anion (figure 3.36) are quite different from C_{10}mimCl+H_2O system. Anion-anion and anion-water peaks are much less intense and the former rdf is more structured, revealing the increased diversity of orientations provided by the more complex nitrate anion. The concentration effect is the same as C_{10}mimCl. The anion-HAR rdf also shows a more structure profile, comprising more intense and broader peaks than C_{10}mimCl, which indicates a more probable interaction, exerted at longer distances and using a more diverse ways of interaction. It seems that in C_{10}mimNO_3+H_2O system, the anion is more connected to the cation (especially at low concentrations), using their different ways to interact and less dissolved in water, leading to larger aggregates per molecule, as expressed in the volumetric analysis of Aggregate program. This trend confirms the favorable interaction between anion and the cation tail [figure 3.37 b)], particularly at low concentrations and exhibiting a strong concentration effect.

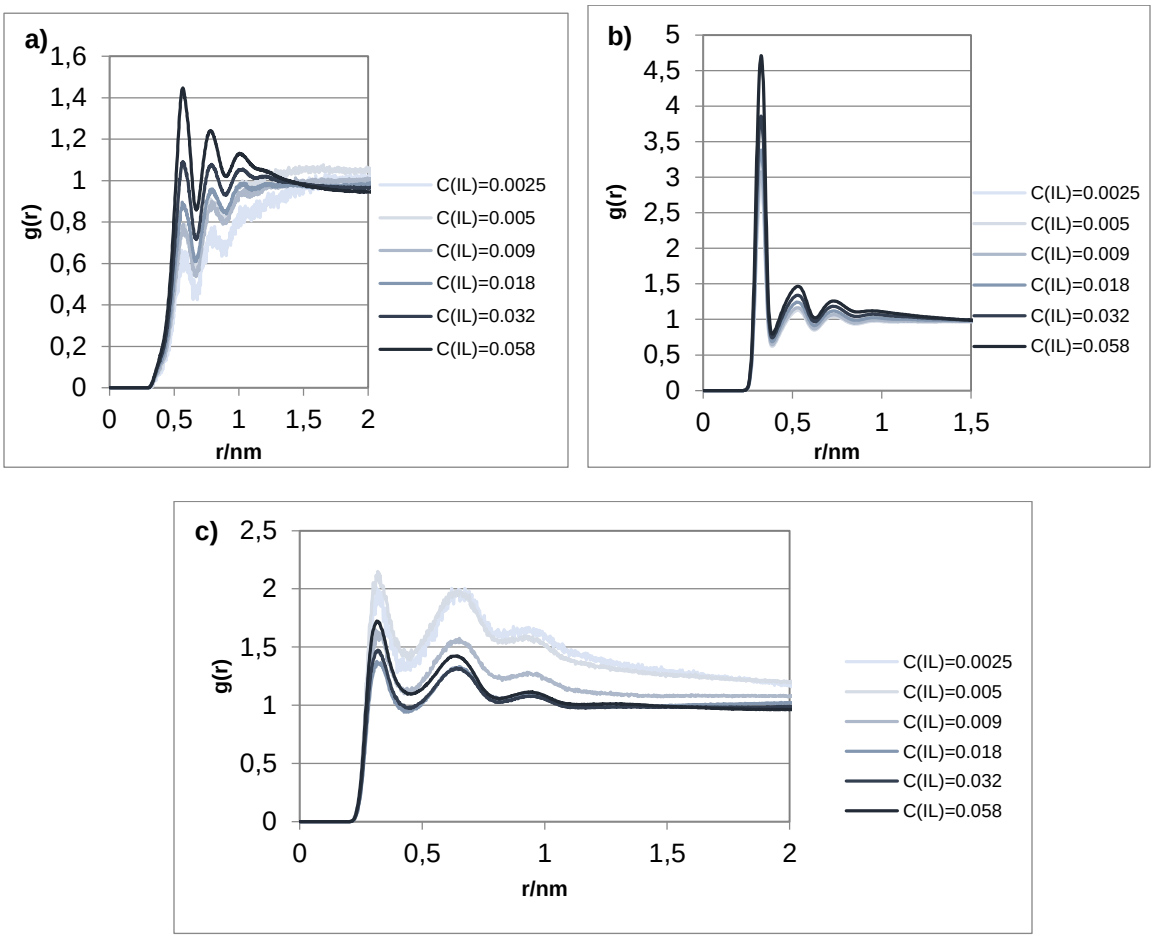

Fig 3.36. RDF for the system of C_{10}mimNO_3 +H_2O with (a) NO_3- NO_3 (b) NO_3-Water (c) NO_3-HAR

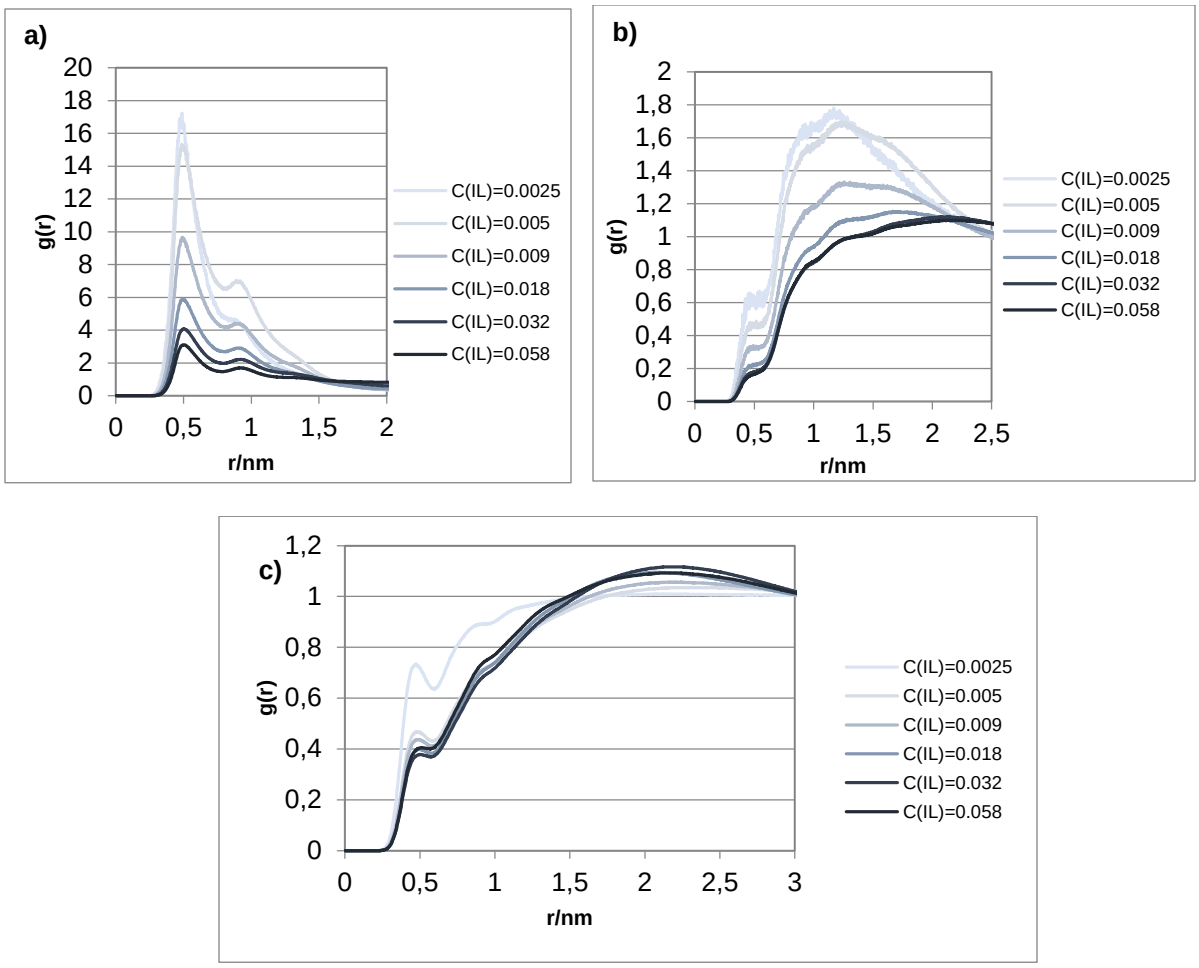

Fig 3.37. RDF for the system of $C_{10}mimNO_3$ +H_2O with (a) Tail-Tail (b) Tail-NO_3(c) Tail-Water

Rdfs for the system $C_{12}mimCl+H_2O$ are shown in figures 3.38, 3.39 and 3.40. As can be seen in figure 3.38, rdfs involving head are very similar with $C_{10}mimCl+H_2O$ system, with a clearer small shoulder in head-head of $C_{12}mimCl$ because of disordered aggregation. The rdf values in head-tail of $C_{12}mimCl+H_2O$ are lower than those $C_{10}mimCl$, revealing also a higher diversity of orientations due to its longer alkyl chain.

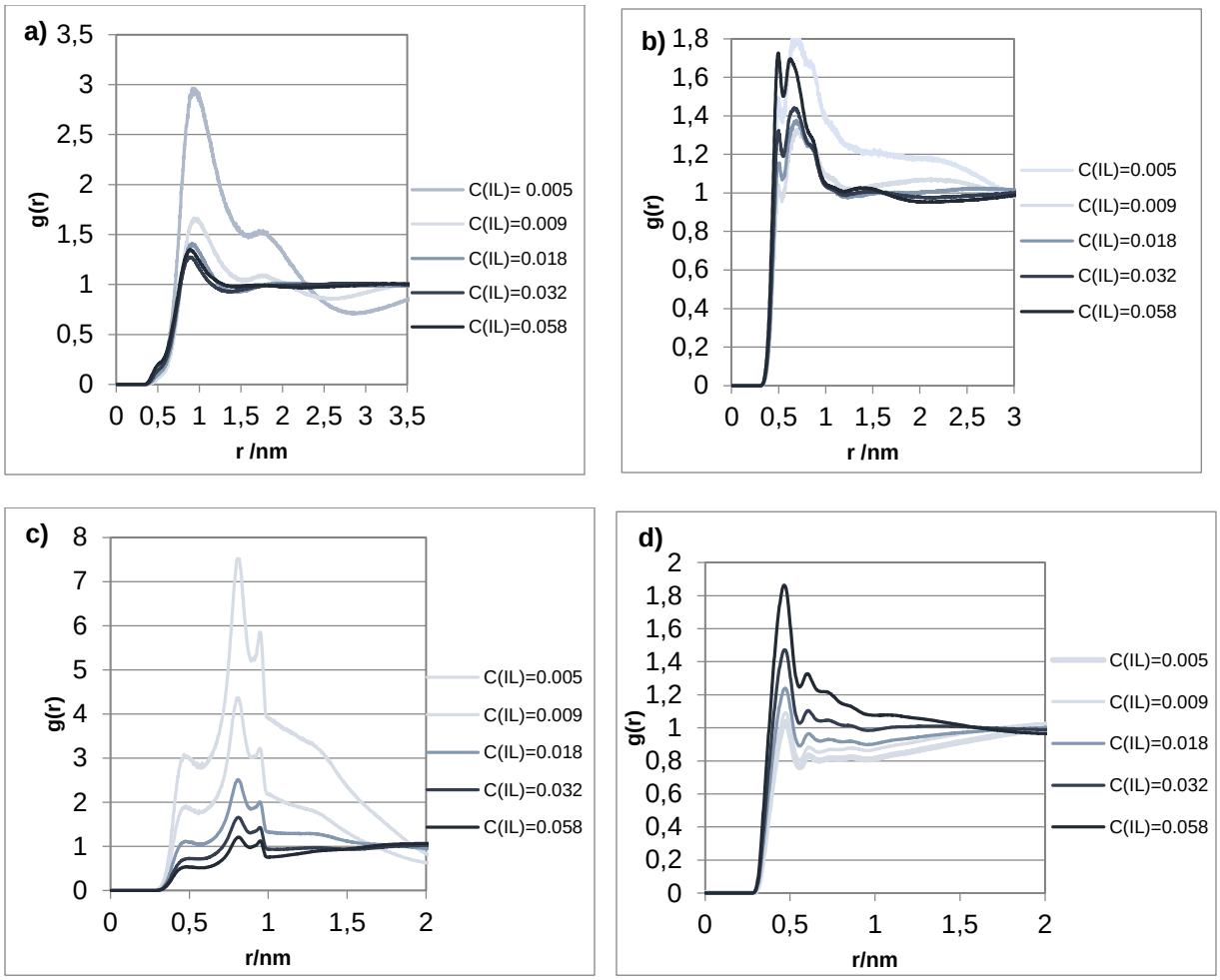

Fig 3.38. RDF for the system of C_{12}mimCl +H_2O with (a) Head-Head (b) Head-Cl (c) Head-Tail (d) Head-Water

Chloride results of $C1_2$mimCl+H_2O in fig 3.39 are exactly same to C_{10}mimCl+H_2O with just higher intensity values of rdf in Cl^- - Cl^- interaction than in C_{10}mimCl+H_2O, which indicated that in this system, chloride seems to be more dissolved in water than in C_{10}mimCl.

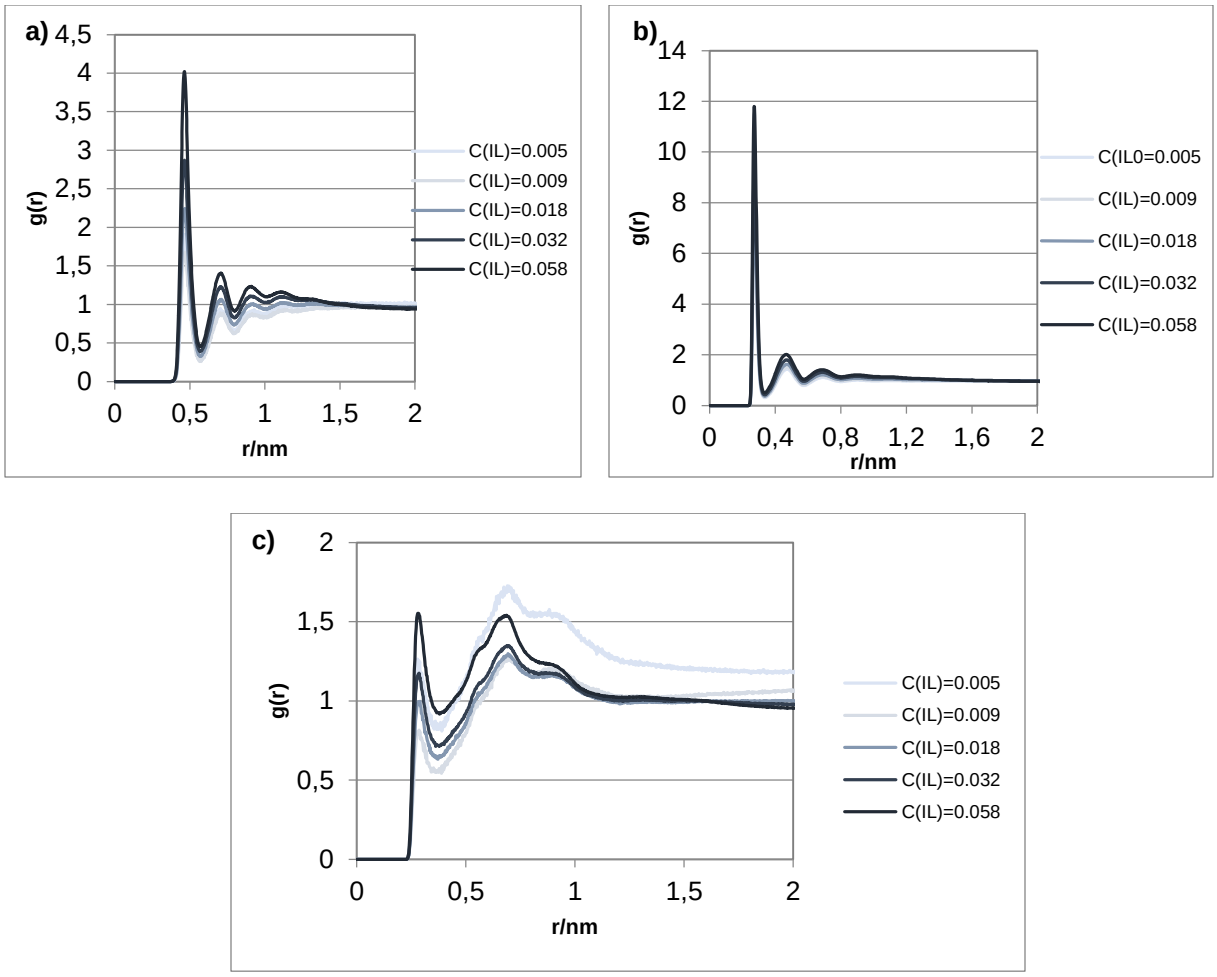

Fig 3.39 RDF for the system of C_{12}mimCl +H_2O with (a) Cl-Cl (b) Cl-Water (c) Cl-HAR

The tail results in fig 3.40 are also quite similar to C_{10}mimCl+H_2O, with the same concentration effect. However, the tail-tail rdf presents more intense peaks than for C_{10}mimCl, meaning that this system forms more compact aggregates because of the enhanced hydrophobicity of the alkyl chain.

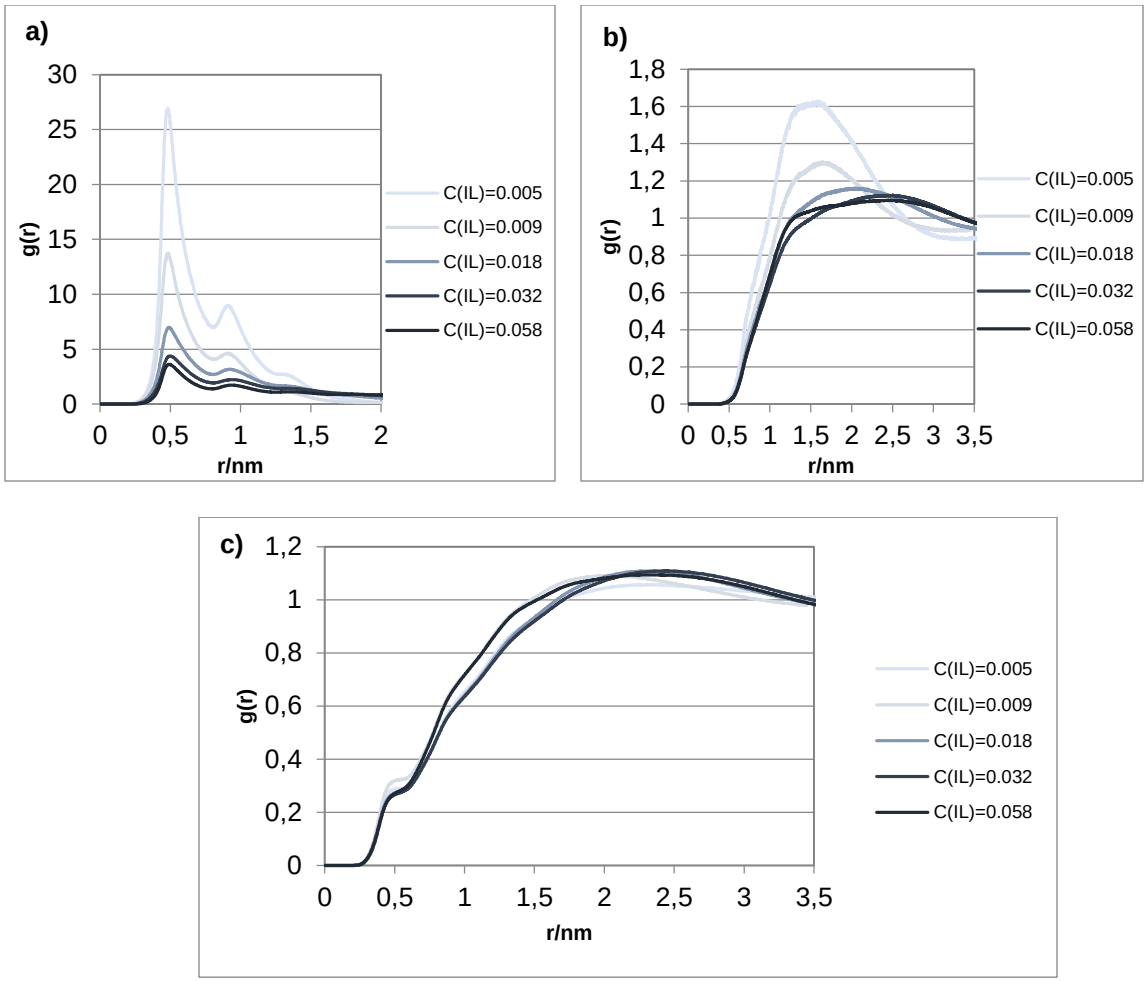

Fig 3.40 .RDF for the system of C_{12}mimCl +H_2O with (a) Tail-Tail (b) Tail-Cl (c) Tail-Water

4. Conclusion

This work (involving experimental and simulation approaches) allows to draw some important conclusions on this type of systems.

All the mixtures studied by DLS are polydisperse, but present main types of aggregates with diameters consistently between 1 and 3 nm. There is no indication of an increase in diameter or change of aggregate shape with increasing concentration when approaching the gel limit, at least within the concentration range studied. In fact, the aggregate sizes obtained by DLS remain almost constant with concentration for each system.

The aggregate sizes seem to be influenced by the size of the anion, which suggests that the anion is somehow inserted into the aggregates, while the effect of the alkyl side chain length is not so clear.

The rheological properties of the gel phase of the C10mimCl + H_2O system are typical of gels, showing an appreciable stability of the elastic modulus as a function of shear strain until the breakdown of its structure, and as a function of oscillation frequency for values above a certain limit. The C10mimCl + H_2O gel is a viscoelastic sample with a predominant elastic component, and it is found to be highly shear-thinning.

A marked concentration effect is observed in the rheological behavior of the C10mimCl + H_2O gel. The gel with the lowest IL concentration is found to be stronger, more stable, and more rigid than that with the higher concentration.

The simulation results qualitatively capture the tendency to form aggregates of particular sizes and also reproduce, at least in part, the differences between systems regarding the concentration at which aggregation begins (CMC). On the other hand, simulation results indicate an increase in polydispersivity with increasing concentration and an increase in the average aggregate size, but they do not predict any percolation phenomenon.

Furthermore, the simulation results show that the chloride anion is more prone to be dissolved in water than bromide and nitrate. The bromide-based ILs tend to form looser aggregates in water, while the bromide and nitrate anions interact more strongly with the most acidic hydrogen of the imidazolium ring than chloride does.

5. References

1. Lei, Z., Chen, B., Koo, Y. M., & MacFarlane, D. R. (2017). Introduction: ionic liquids. Chemical Reviews, 117(10), 6633-6635.
2. Ionic Liquids: Properties and Applications. (n.d.). Frontiersin.Org. Retrieved May 22, 2025, from https://www.frontiersin.org/research-topics/7972/ionic-liquids-properties-and-applications/magazine
3. Hayes, R., Warr, G. G., & Atkin, R. (2015). Structure and nanostructure in ionic liquids. Chemical Reviews, 115(13), 6357–6426. https://doi.org/10.1021/cr500411q
4. Sharma, P., Sharma, S., & Kumar, H. (2024). Introduction to ionic liquids, applications and micellization behaviour in presence of different additives. Journal of Molecular Liquids, 393(123447), 123447. https://doi.org/10.1016/j.molliq.2023.123447
5. Tiago, G. A. O., Matias, I. A. S., Ribeiro, A. P. C., & Martins, L. M. D. R. S. (2020). Application of Ionic Liquids in Electrochemistry—Recent Advances. Molecules, 25(24), 5812. https://doi.org/10.3390/molecules25245812
6. Puga, A. V. (2013). Alicyclic ammonium ionic liquids as lithium battery electrolytes: A review. Chimica Oggi – Chemistry Today, 31(2), 12–16. https://www.webofscience.com/wos/woscc/full-record/WOS:000319215200004
7. Han, D., & Row, K. H. (2010). Recent Applications of Ionic Liquids in Separation Technology. Molecules, 15(4),2405-2426.https://doi.org/10.3390/molecules15042405
8. Maciejewski, H. (2021). Ionic Liquids in Catalysis. Catalysts, 11(3), 367. https://doi.org/10.3390/catal11030367
9. Sangeetha, B., & Baskar, G. (2022). Biodiesel production using ionic liquid-based catalysts. In Biodiesel Production (pp. 249–267). Wiley. https://doi.org/10.1002/9781119771364.ch13
10. Pinto, A. M., Rodríguez, H., Arce, A., & Soto, A. (2014). Combined physical and chemical absorption of carbon dioxide in a mixture of ionic liquids. The Journal of Chemical Thermodynamics, 77, 197–205. https://doi.org/10.1016/j.jct.2013.10.023
11. Liu, M., Ni, J., Zhang, C., Wang, R., Cheng, Q., Liang, W., & Liu, Z. (2024). The Application of Ionic Liquids in the Lubrication Field: Their Design, Mechanisms, and Behaviors. Lubricants, 12(1), 24. https://doi.org/10.3390/lubricants12010024
12. Weiss, R. G. (2018). Chapter 1. Introduction: An overview of the “what” and “why” of molecular gels. In Monographs in Supramolecular Chemistry (pp. 1–27). Royal Society of Chemistry.

13. Yang, D. (2022). Recent advances in hydrogels. Chemistry of Materials: A Publication of the American Chemical Society, 34(5), 1987–1989. https://doi.org/10.1021/acs.chemmater.2c00188
14. Le Bideau, J., Viau, L., & Vioux, A. (2011). Ionogels, ionic liquid based hybrid materials. Chemical Society Reviews , 40 (2), 907–925. https://doi.org/10.1039/c0cs00059k
15. Vioux, A., Viau, L., Volland, S., & Le Bideau, J. (2009). Use of ionic liquids in sol-gel; ionogels and applications. Reports. Chemistry , 13 (1–2), 242–255. https://doi.org/10.1016/j.crci.2009.07.002
16. Egorova, K. S., Gordeev, E. G., & Ananikov, V. P. (2017). Biological activity of ionic liquids and their application in pharmaceutics and medicine. Chemical Reviews, 117(10), 7132–7189. https://doi.org/10.1021/acs.chemrev.6b00562
17. Yuan, J., & Antonietti, M. (2011). Poly(ionic liquid)s: Polymers expanding classical property profiles. Polymer, 52(7), 1469–1482. https://doi.org/10.1016/j.polymer.2011.01.043
18. Nebgen, B. T., Magurudeniya, H. D., Kwock, K. W. C., Ringstrand, B. S., Ahmed, T., Seifert, S., Zhu, J.-X., Tretiak, S., & Firestone, M. A. (2017). Design principles from multiscale simulations to predict nanostructure in self-assembling ionic liquids. Faraday Discussions, 206(0), 159–181. https://doi.org/10.1039/c7fd00154a
19. Canongia Lopes, J. N.; Deschamps, J.; Pádua, A. A. H., "Modeling Ionic Liquids Using a Systematic All-Atom Force Field", J. Phys. Chem. B, 2004, 108, 2038-2047; Canongia Lopes, J. N.; Pádua, A. A. H., "CL&P: A generic and systematic force field for ionic liquids modeling", Theor. Chem. Acc., 2012, 131:1129
20. Abascal, J. L. F.; Vega, C., "A General Purpose Model for the Condensed Phases of Water: TIP4P/2005", J. Chem. Phys.; 2005, 123, 234505-234512
21. Jorgensen, W. L.; Maxwell, D. S.; Tirado-Rives, J., "Development and Testing of the OPLS All-Atom Force Field on Conformational Energetics and Properties of Organic Liquids", J. Am. Chem. Soc., 1996, 118 (45), 11225-1123631
22. C. E. S. Bernardes, J. Comp. Chem. **2017**, 38, 753-765.
23. C. E. S. Bernardes, Zenodo. **2021**, DOI: 10.5281/zenodo.4450903
24. R. D. Shannon, "Revised Effective Ionic Radii and Systematic Studies of Interatomic Distances in Halides and Chalcogenides", *Acta Crystallographica*. (1976). A32, Pages 751-767
25. Dasent, p. 78; H.D.B. Jenkins and K.P. Thakur, J. Chem. Educ., 56, 576 (1979)

26. Chihiro Kikuchi, Hina Kurane, Takuma Watanabe, Makoto Demura, Takashi Kikukawa, Takashi Tsukamoto, “Preference of Proteomonas sulcata anion channel rhodopsin for nitrate revealed using a pH electrode method”, Scientic Reports, April 2021

Supporting Information

1. DLS Graphs for Intensity for all Compounds

A. C_{10}mimCl +H_2O

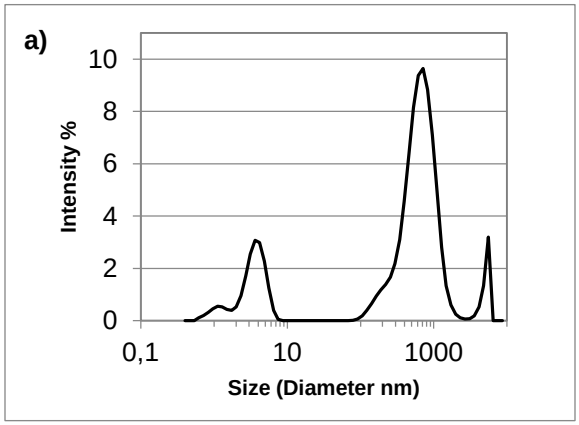

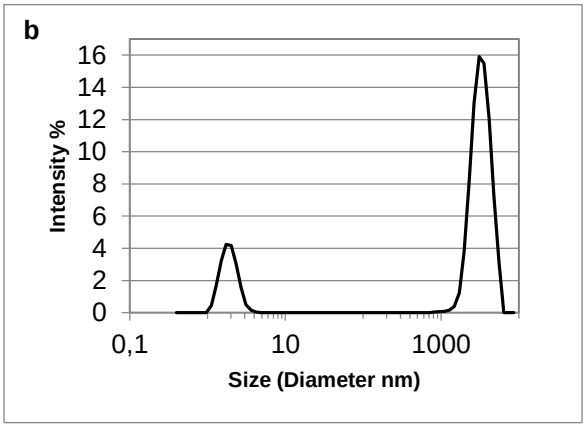

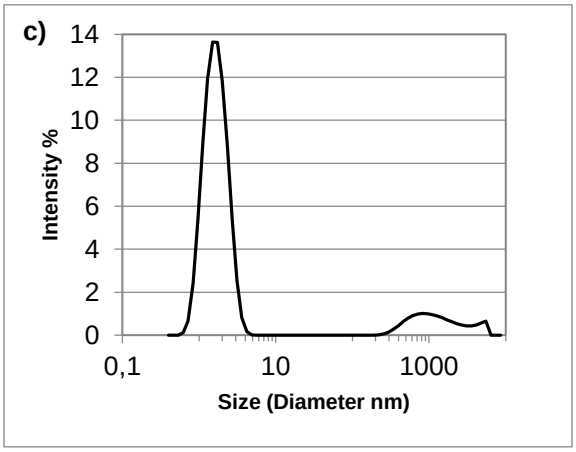

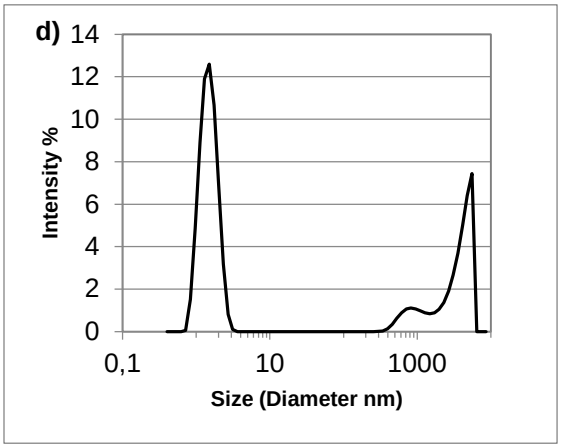

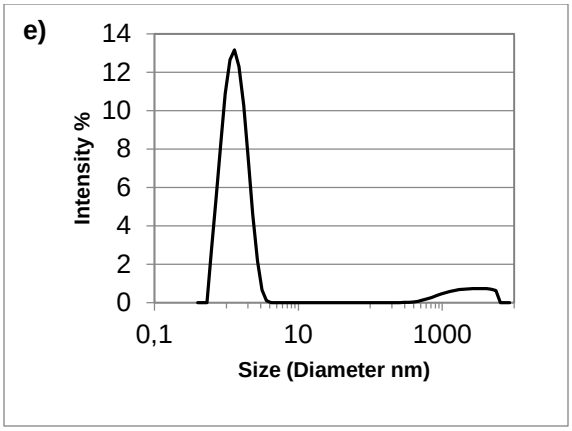

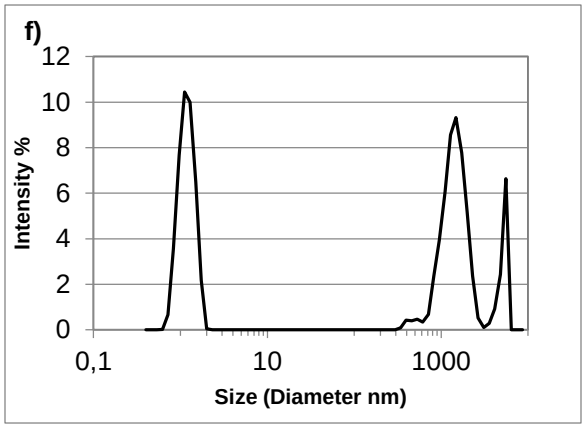

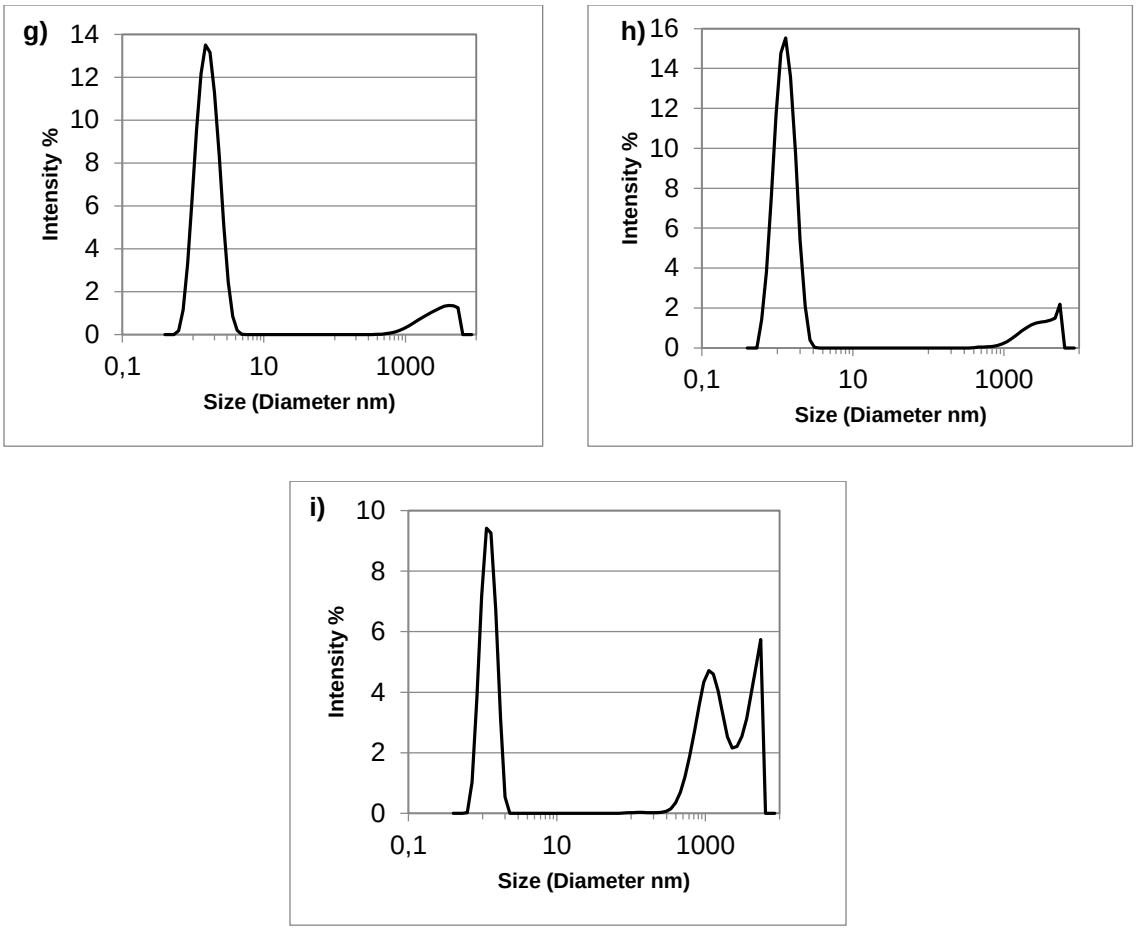

Fig 1. System of C_{10}mimCl+H_2O showing (a)70mM (b) 120mM (c) 250mM (d) 500mM (e) 750mM (f) 1000mM (g) 1013mM (h) 1241mM (i) 1250mM

B. C_{10}mimBr +H_2O

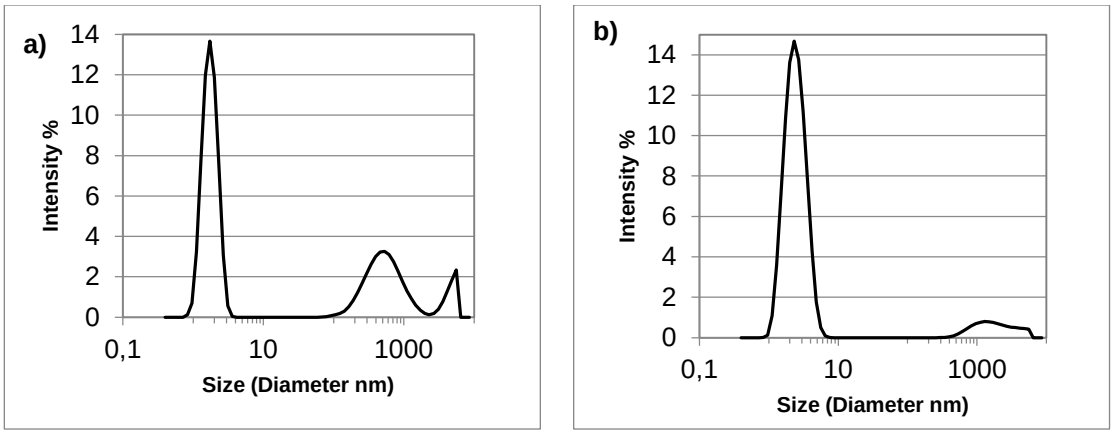

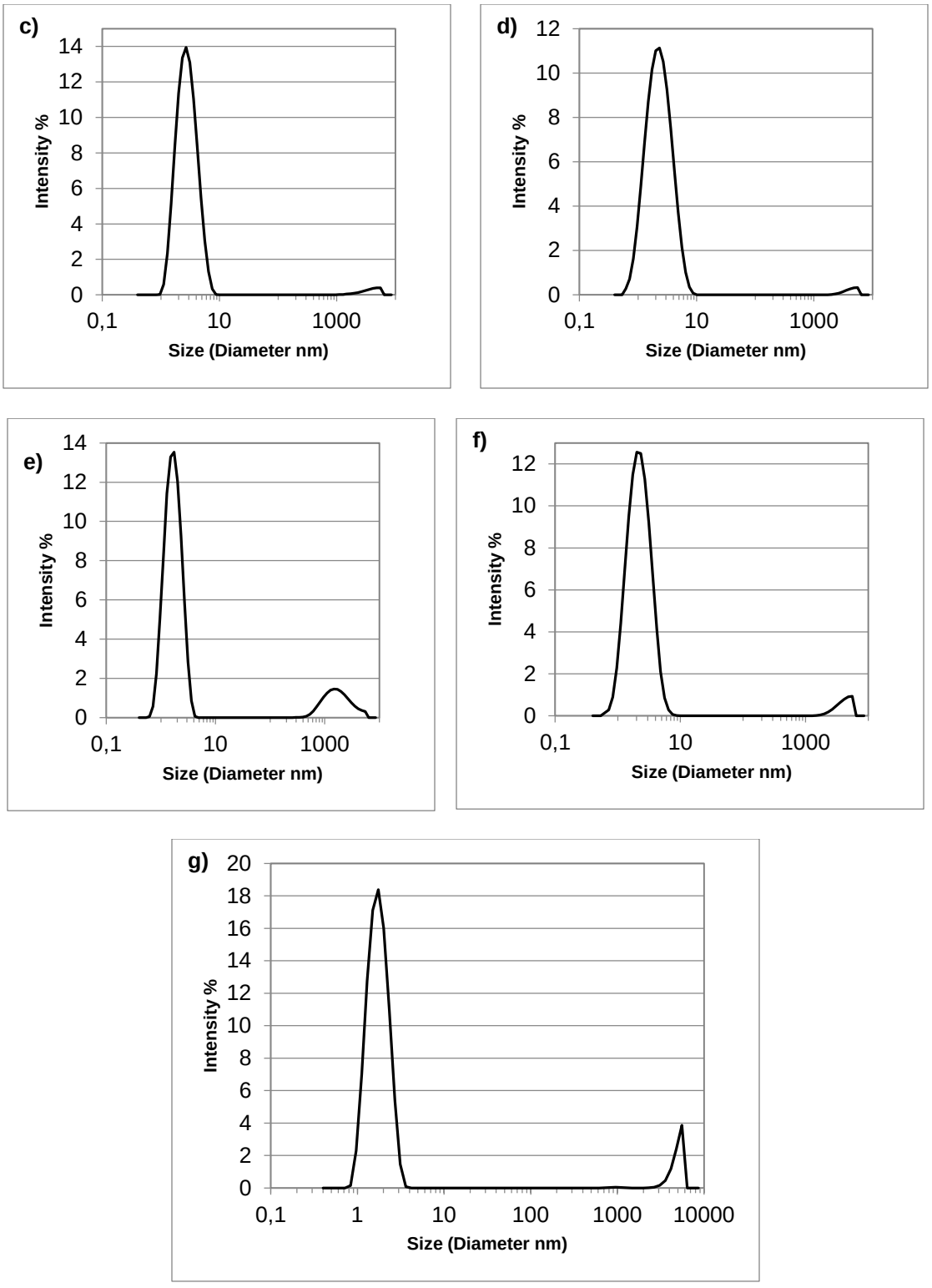

Fig 2. C_{10}mimBr+H_2O system with (a) 50mM (b) 90mM (c) 200mM (d) 500mmM (e) 690mM (f) 998mM (g) 1491mM

C. **C_8mimCl +H_2O**

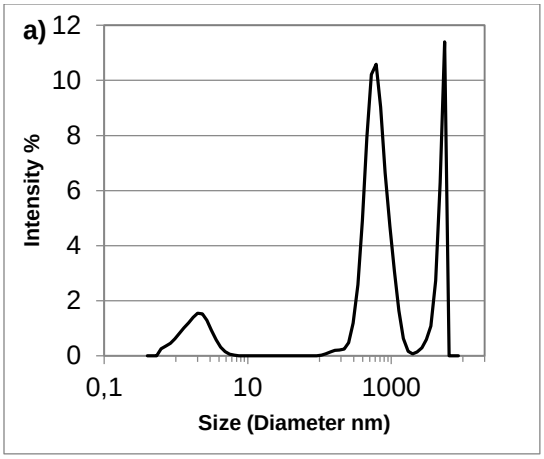

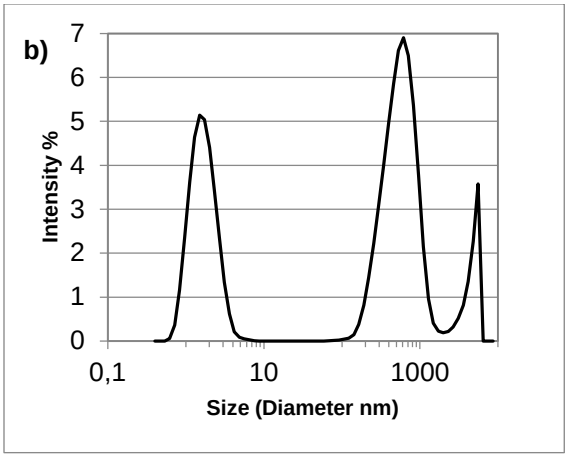

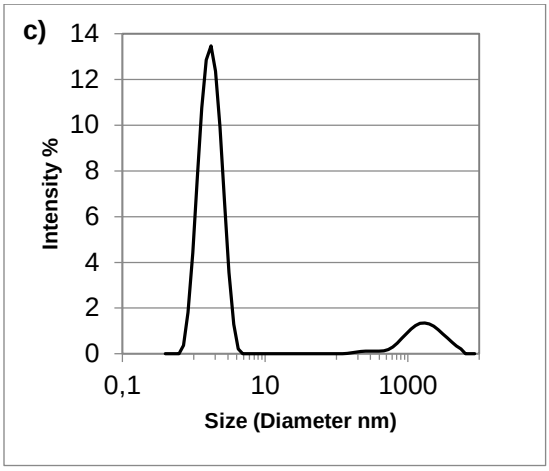

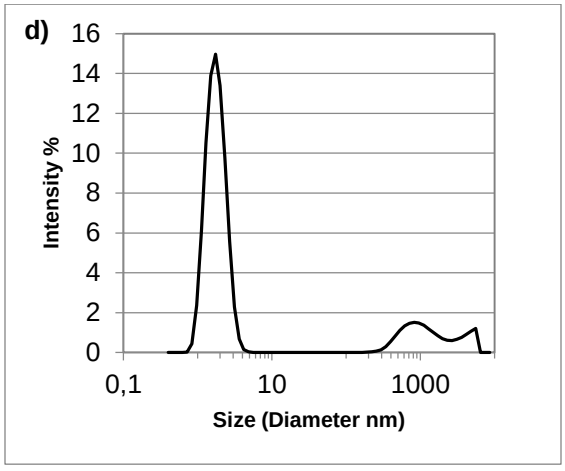

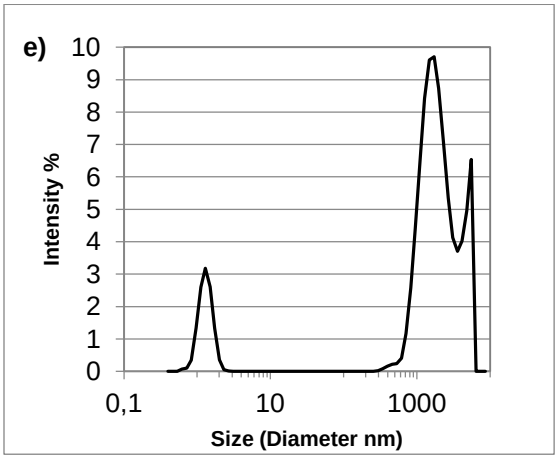

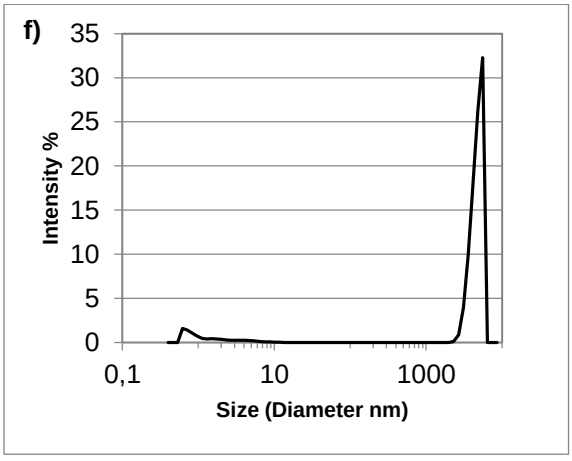

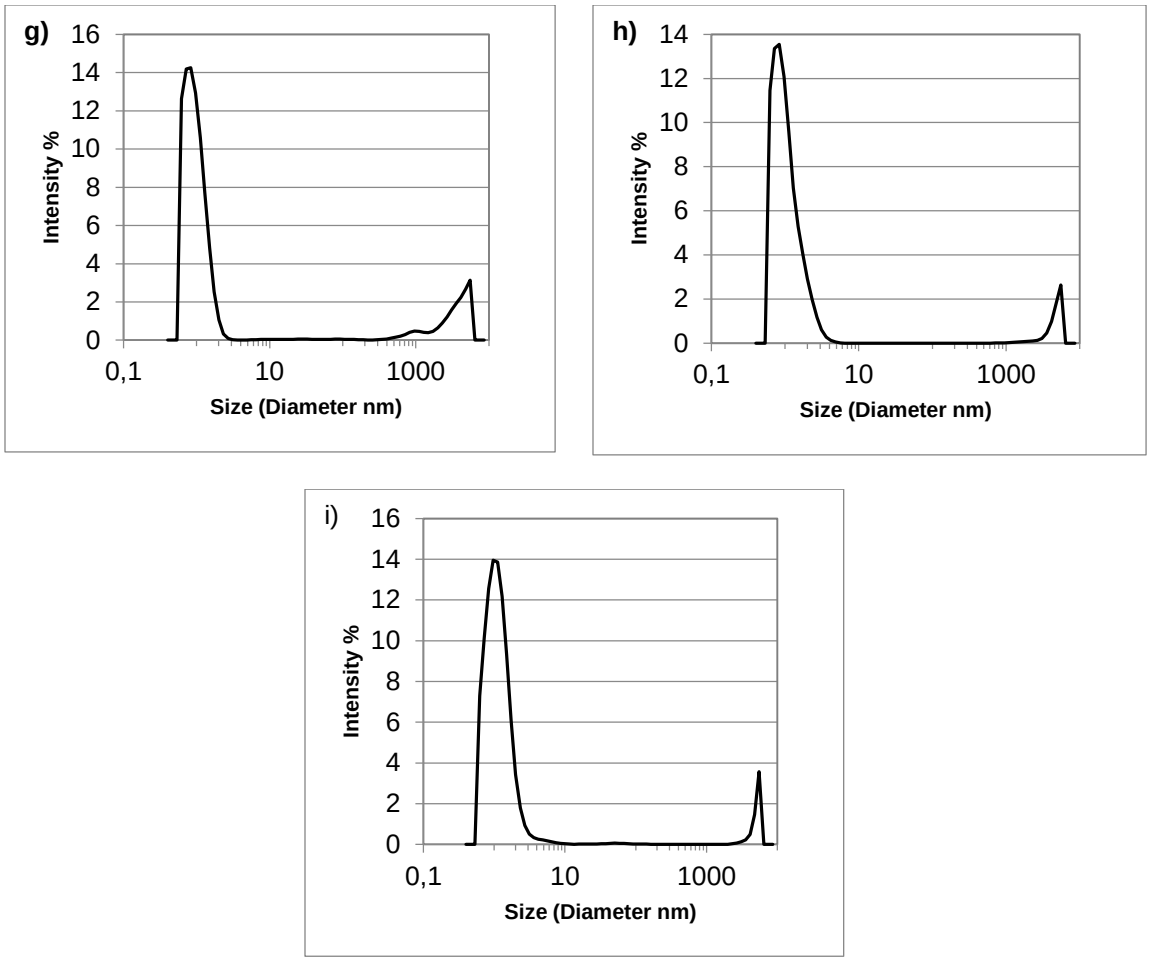

Fig 3: System of C_8mimCl+H_2O with (a) 298mM (b) 304mM (c) 500mM (d) 507mM (e) 1005mM (f) 1970mM (g) 2005mM (h) 3022Mm (j) 3236mM

D. C_8mimBr +H_2O

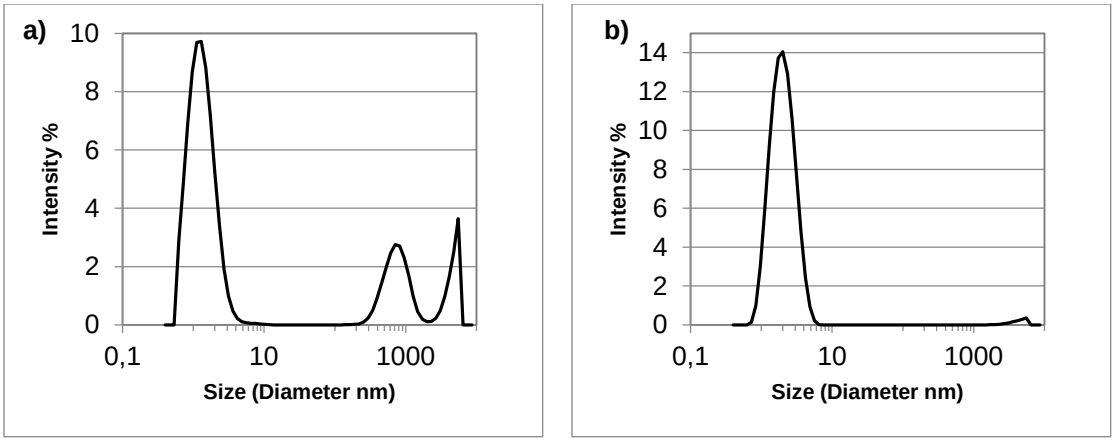

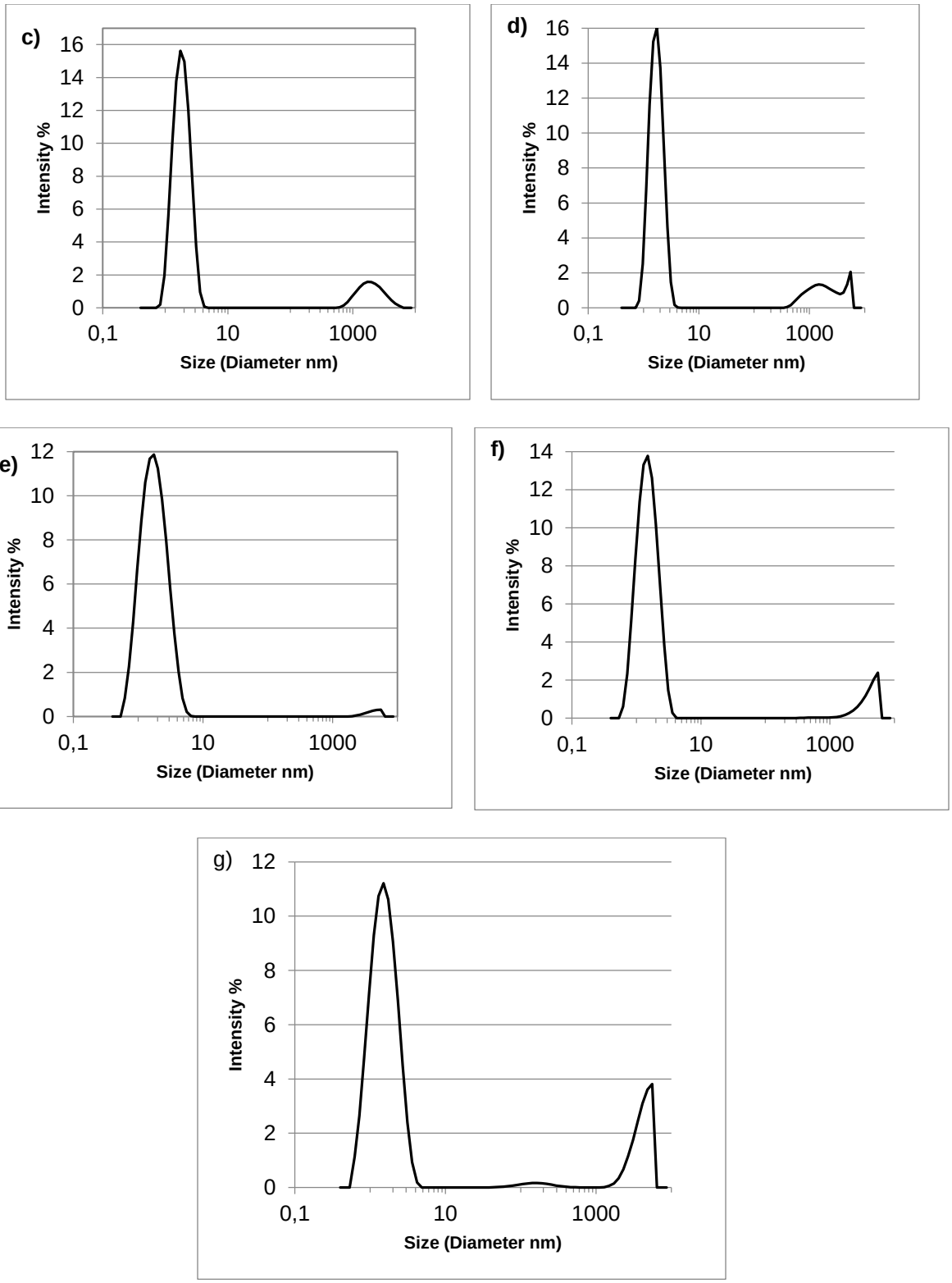

Fig 4. C_8mimBr +H_2O with (a) 200mM (b) 505mM (c) 751mM (d) 1000mM (e) 1503mM (f) 2000mM (g) 2993mM

E. C12mimCl +H_2O

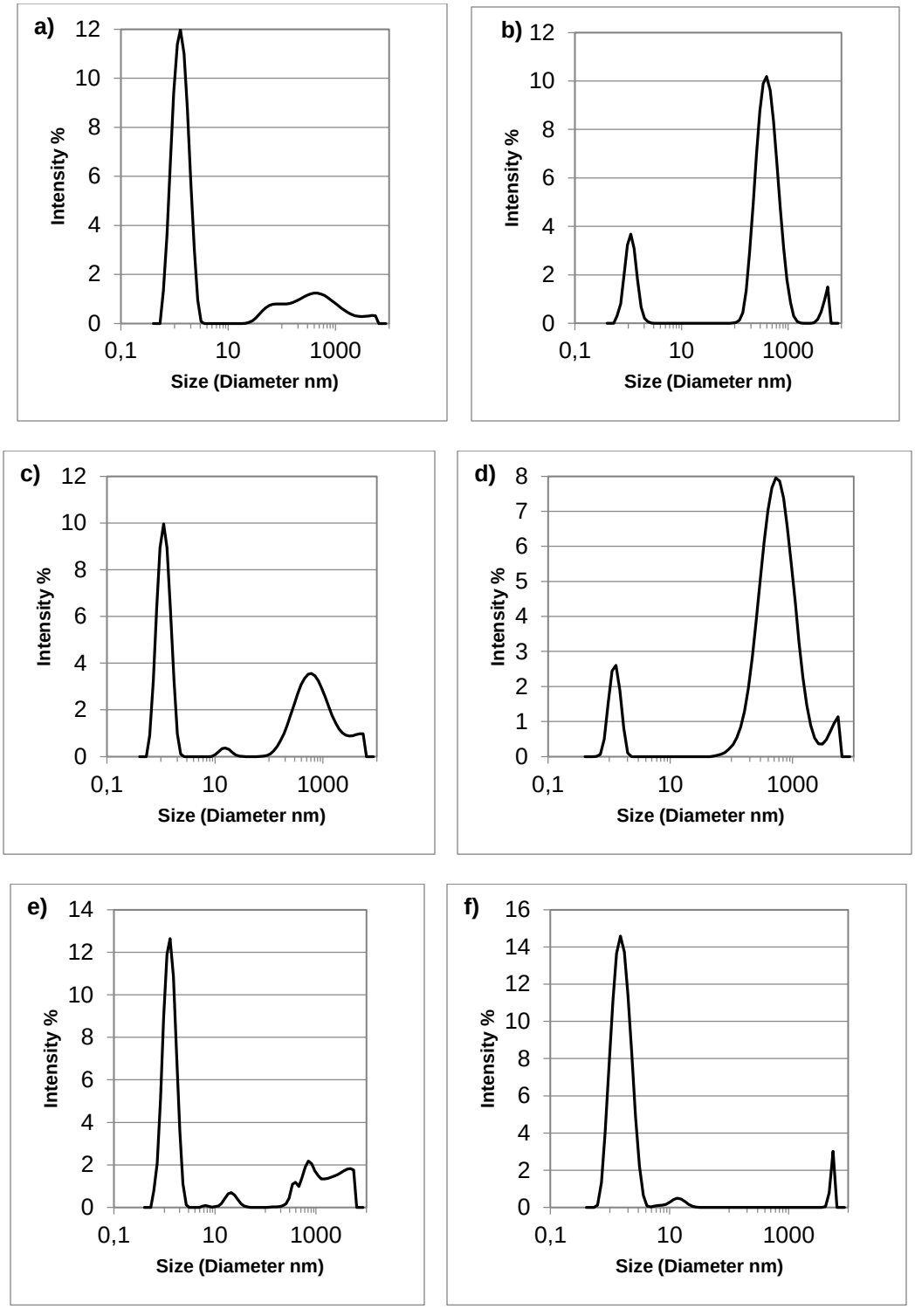

Fig 5. C_{12}mimCl+H_2O with (a) 103mM (b) 202mM (c) 505mM (d) 748mM (e) 1006mM (f) 1497mM

F. $C_{10}mimNO_3 + H_2O$

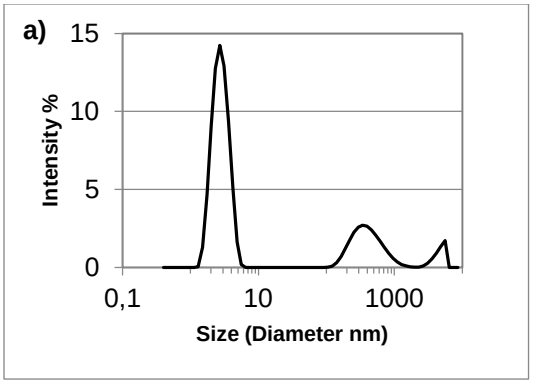

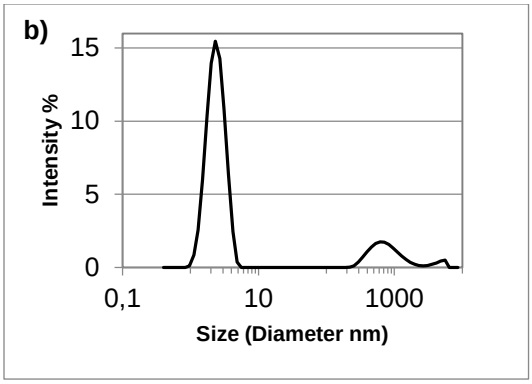

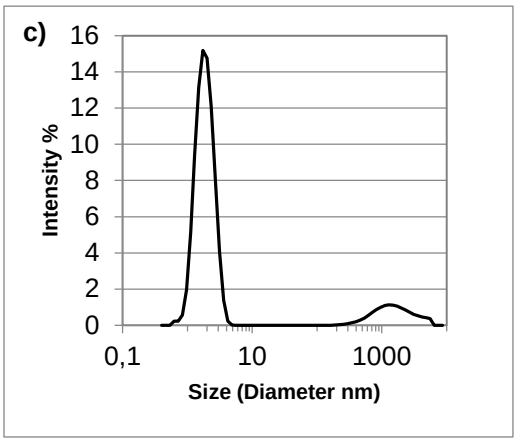

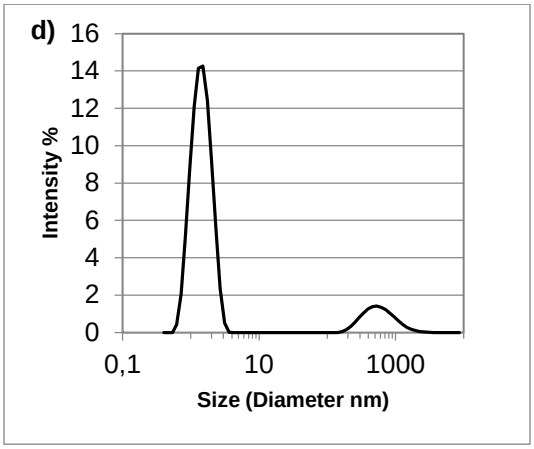

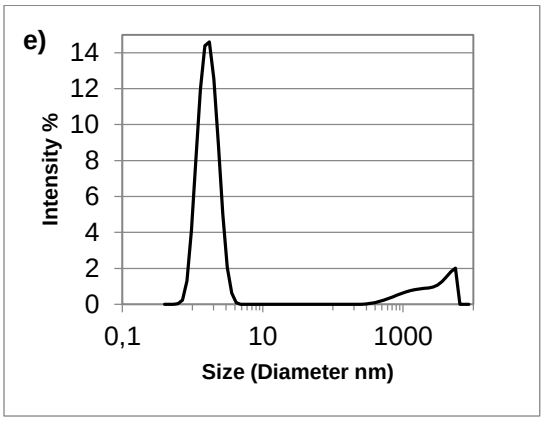

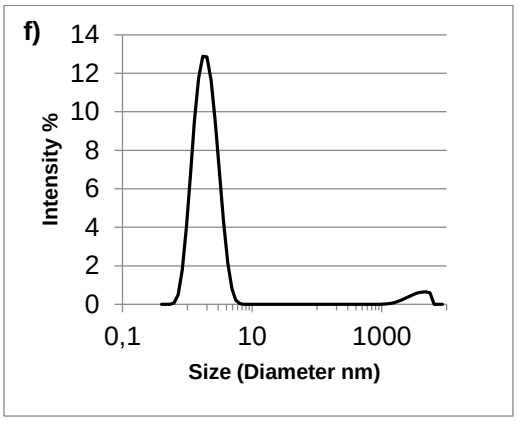

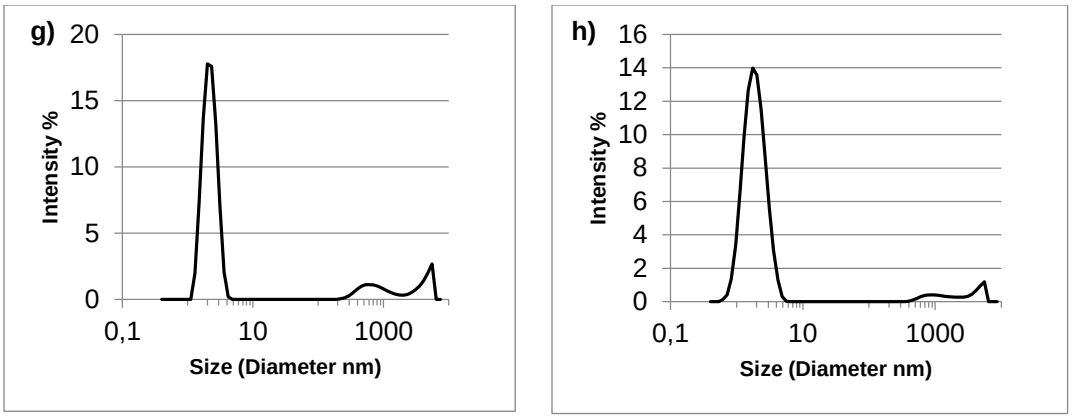

Fig 6. $C_{10}mimNO_3$ with (a) 70mM (b) 119mM (c) 247mM (d) 502mM (e) 744mM (f) 980mM (g) 1257mM (h) 1958mM

2. DLS Graphs For Volume For all Compounds

A. C_{10}mimCl +H_2O

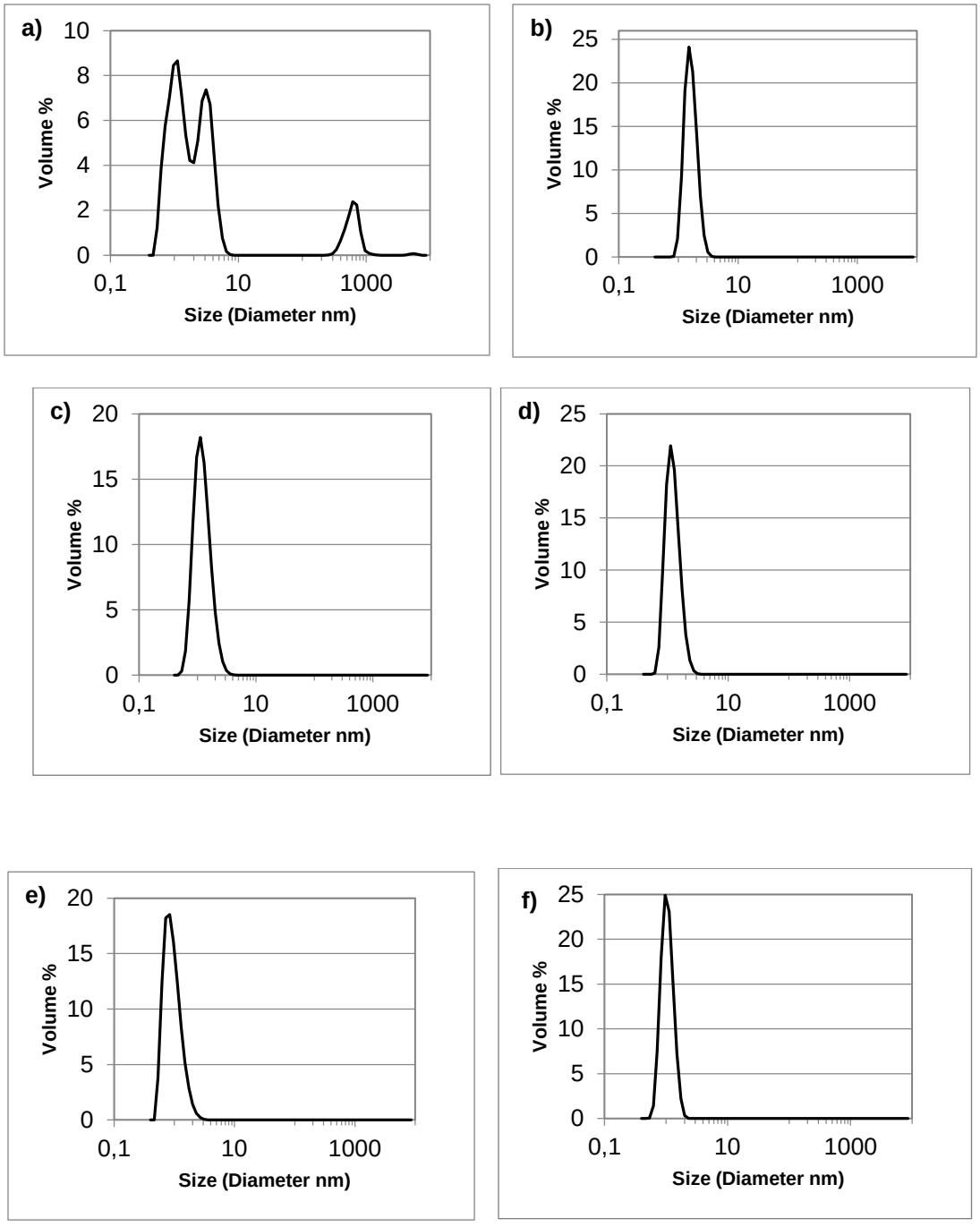

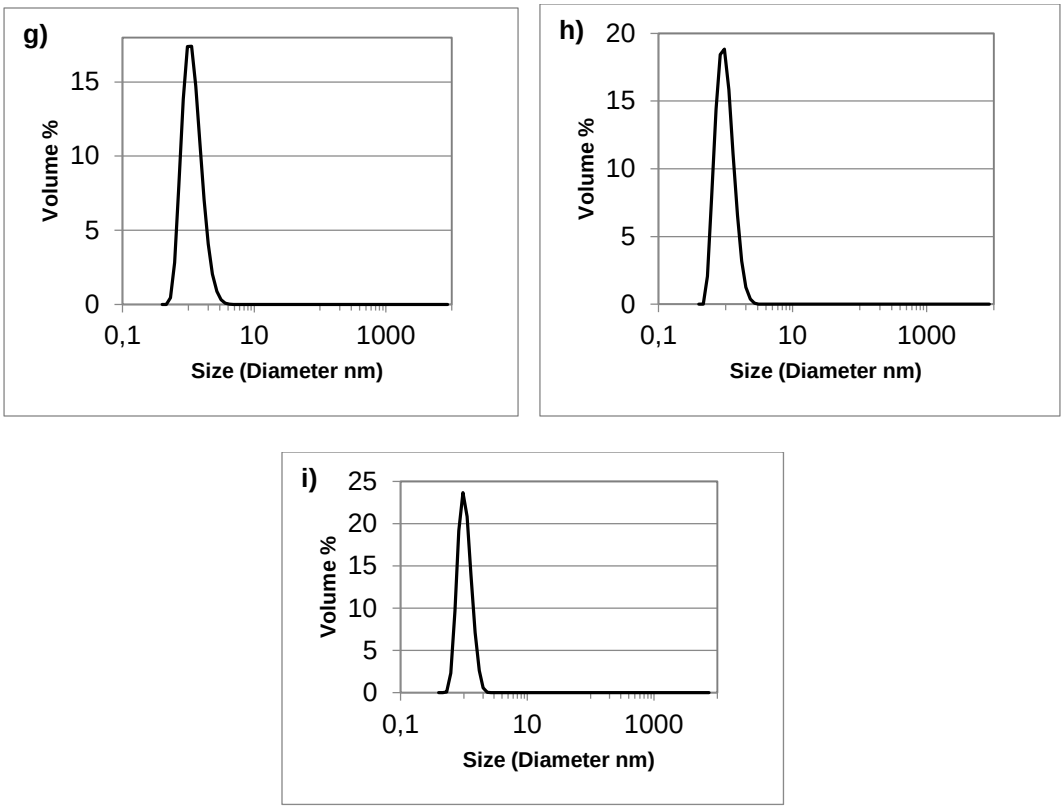

Fig 7. System of C_{10}mimCl+H_2O showing (a)70mM (b) 120mM (c) 250mM (d) 500mM (e) 750mM (f) 1000mM (g) 1013mM (h) 1241mM (i) 1250mM

B. C_{10}mimBr +H_2O

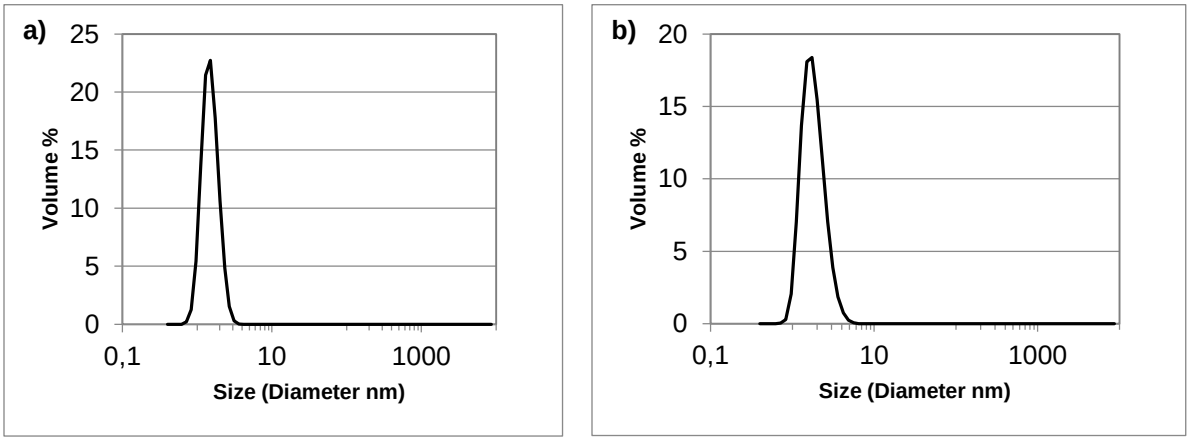

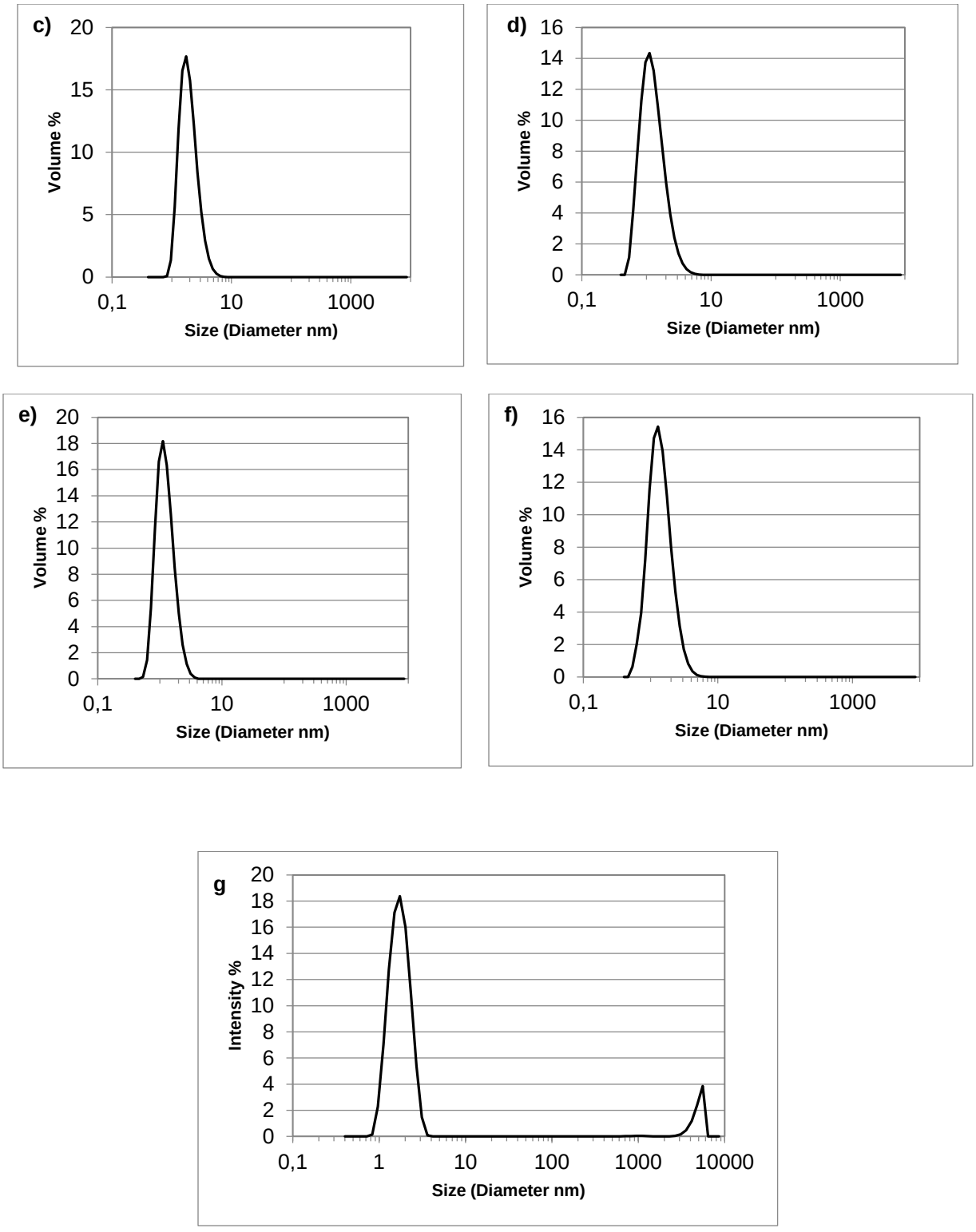

Fig 8. C_{10}mimBr+H_2O system with (a) 50mM (b) 90mM (c) 200mM (d) 500mmM (e) 690mM (f) 998mM (g) 1491mM

C. **C_8mimCl +H_2O**

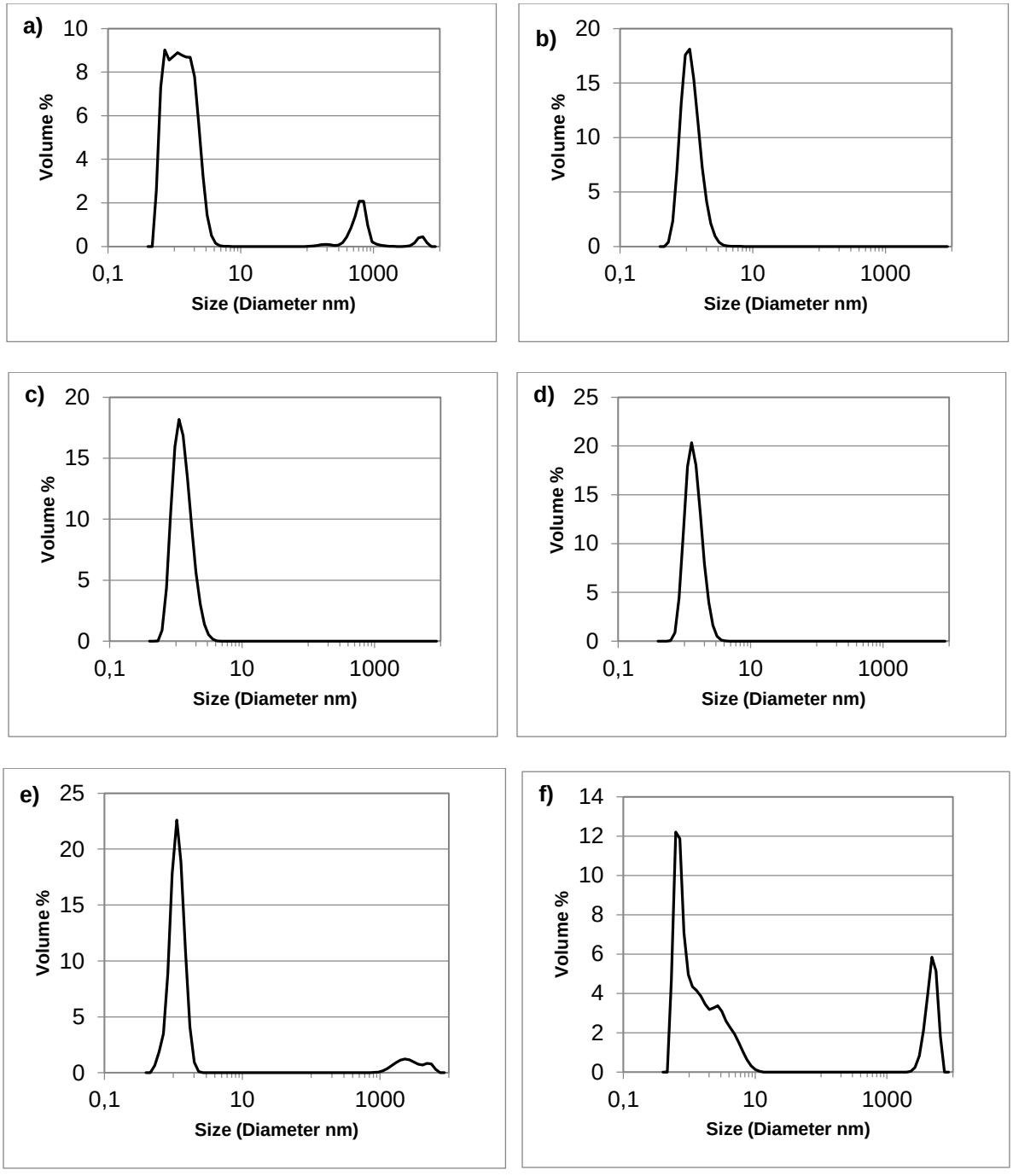

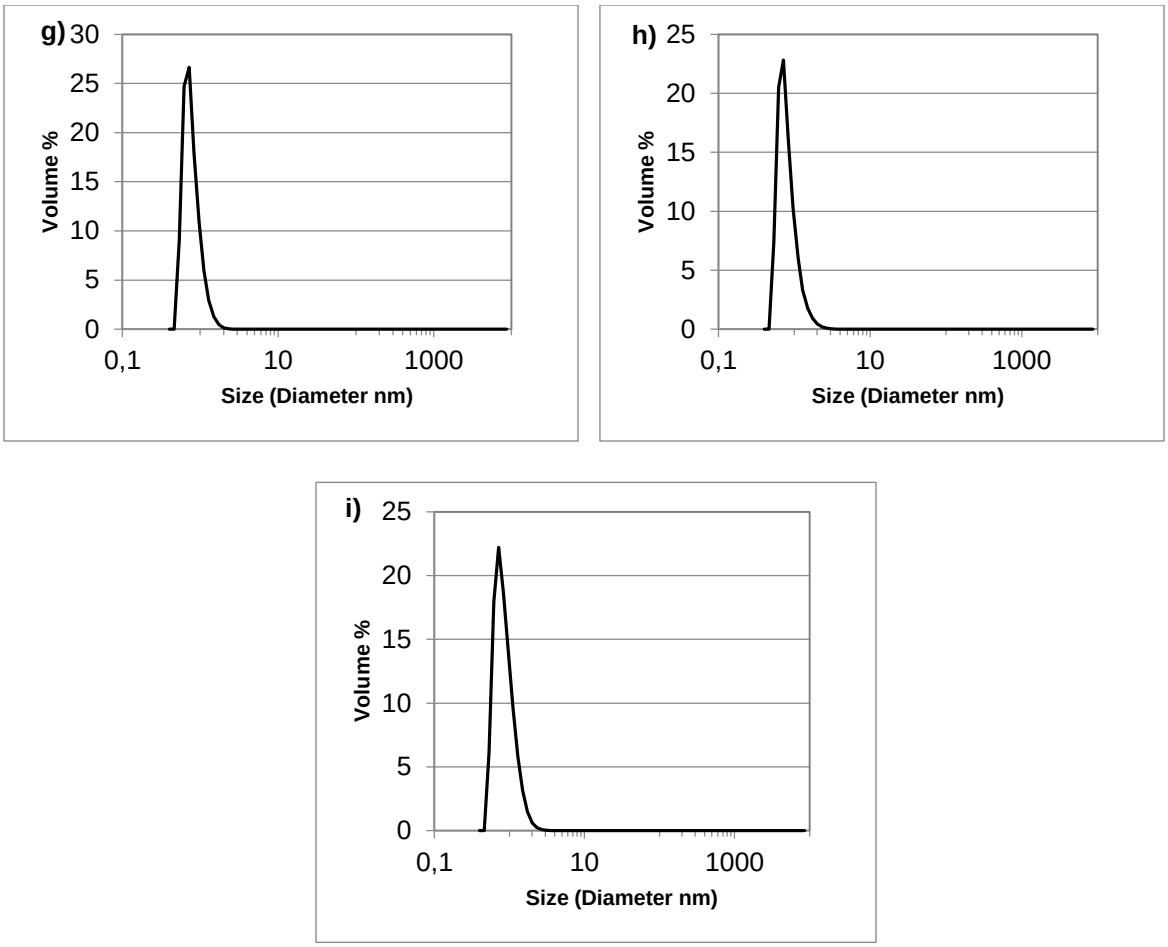

Fig 9. System of C_8mimCl+H_2O with (a) 298mM (b) 304mM (c) 500mM (d) 507mM (e) 1005mM (f) 1970mM (g) 2005mM (h) 3022mM(j) 3236mM

D. C_8mimBr +H_2O

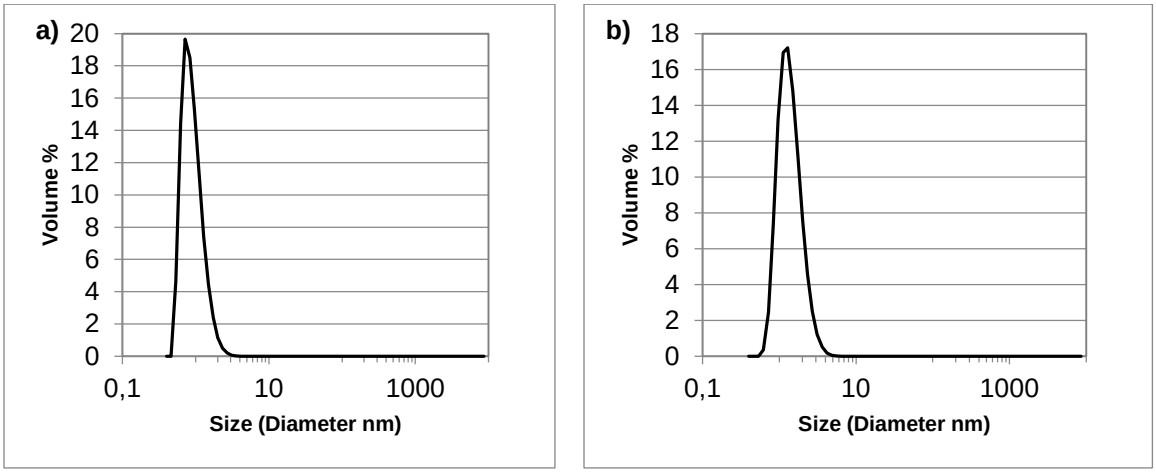

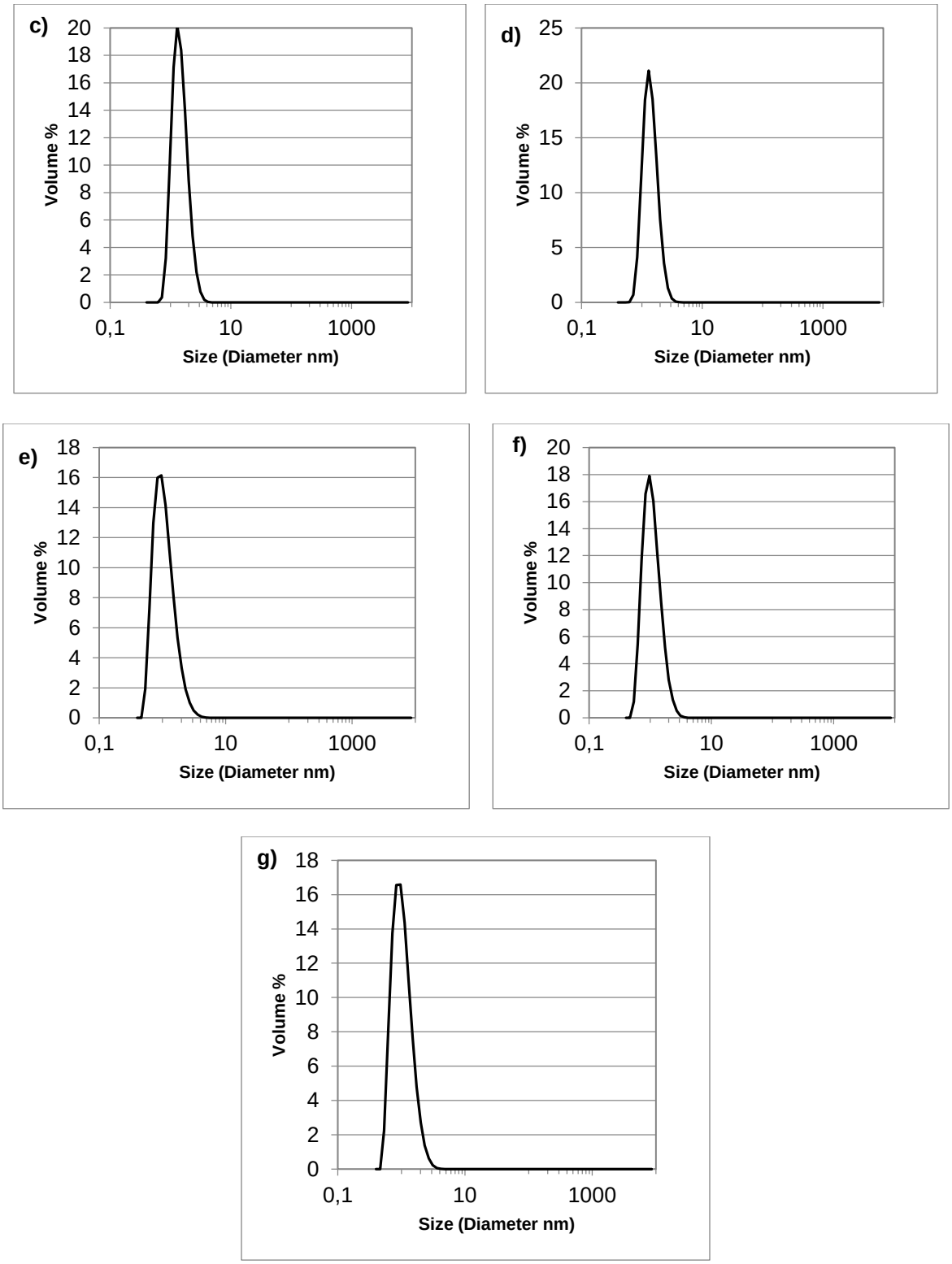

Fig 10. C_8mimBr +H_2O with (a) 200mM (b) 505mM (c) 751mM (d) 1000mM (e) 1503mM (f) 2000mM (g) 2993mM

E. C12mimCl +H_2O

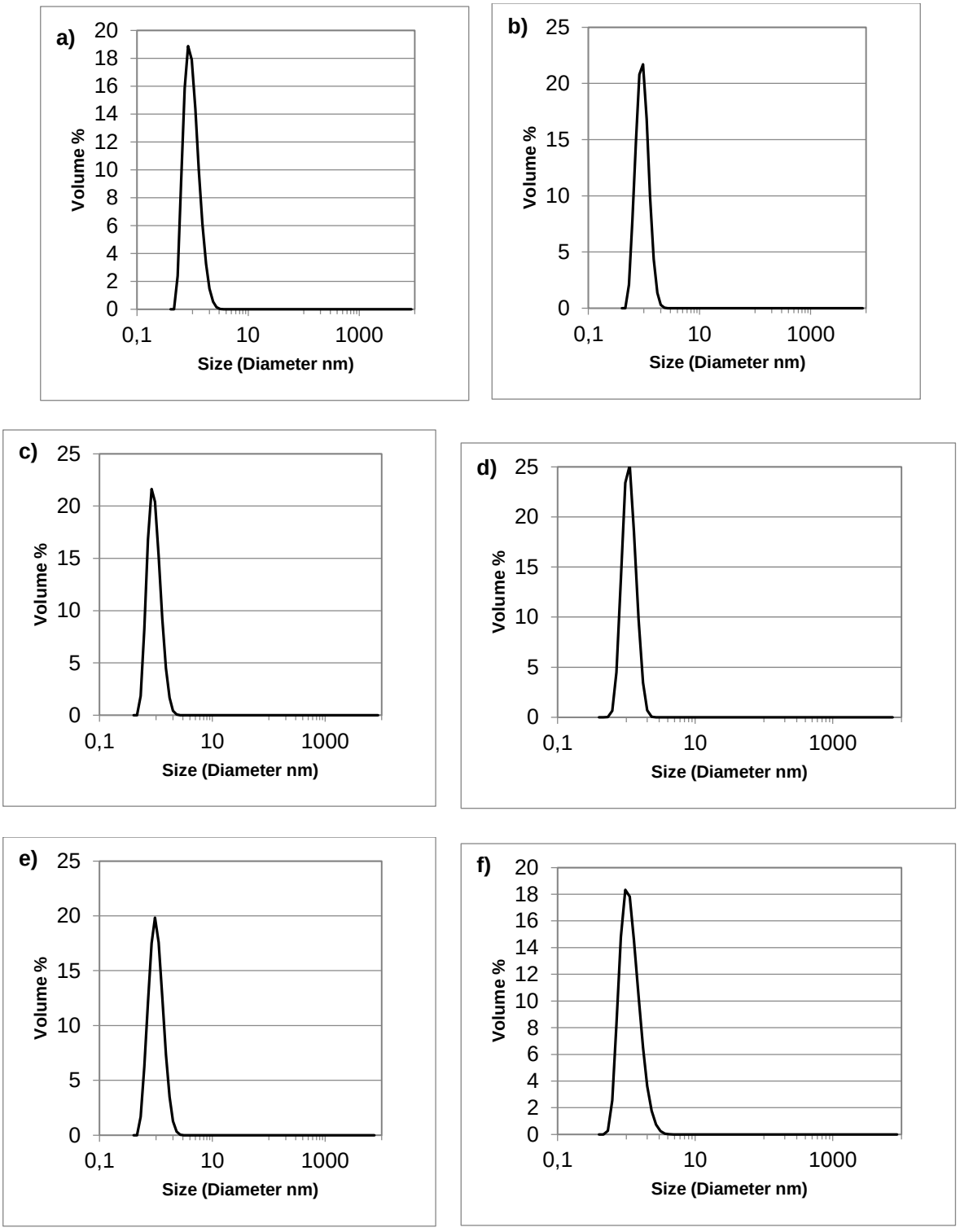

Fig 11. C_{12}mimCl+H_2O with (a) 103mM (b) 202mM (c) 505mM (d) 748mM (e) 1006mM (f) 1497mM

F. $C_{10}mimNO_3 + H_2O$

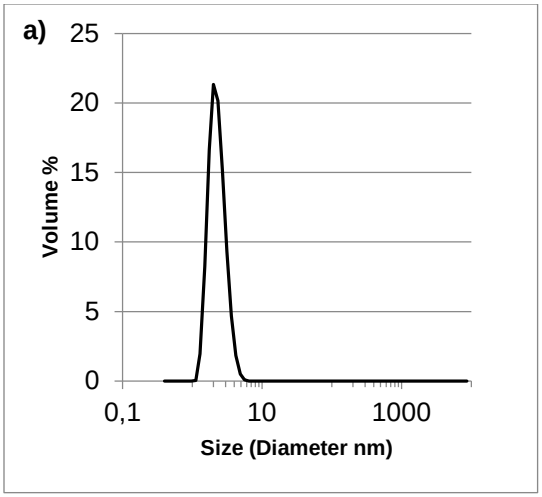

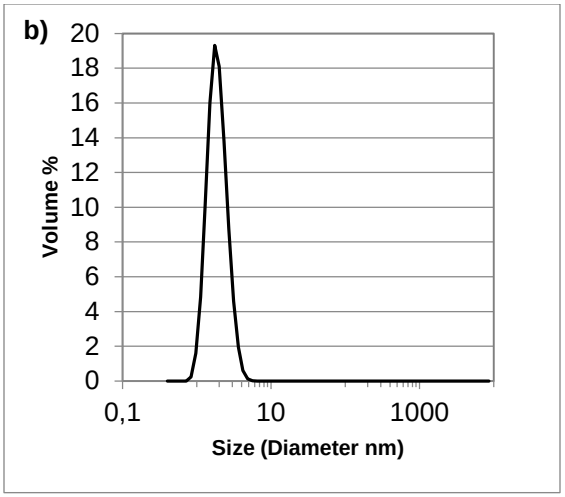

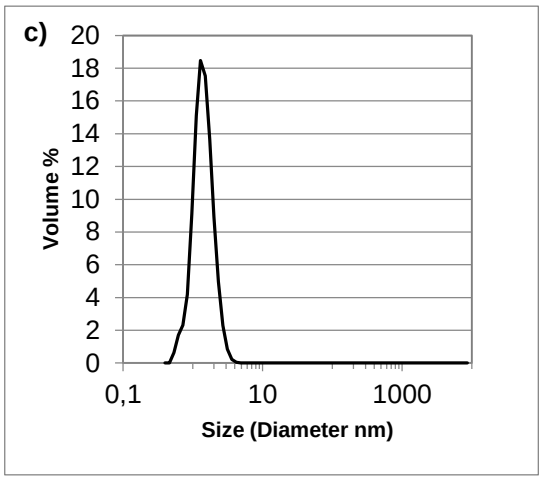

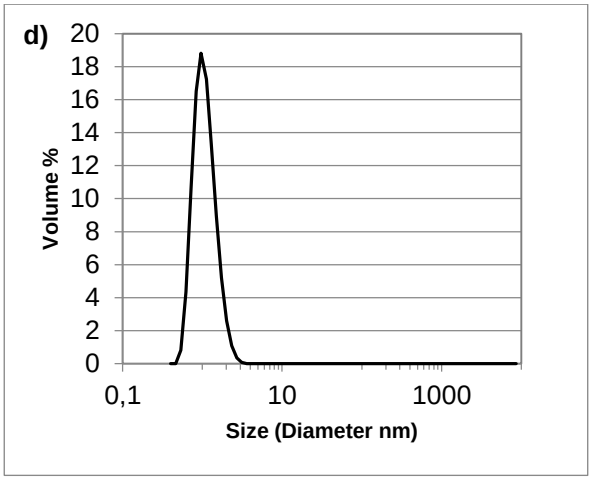

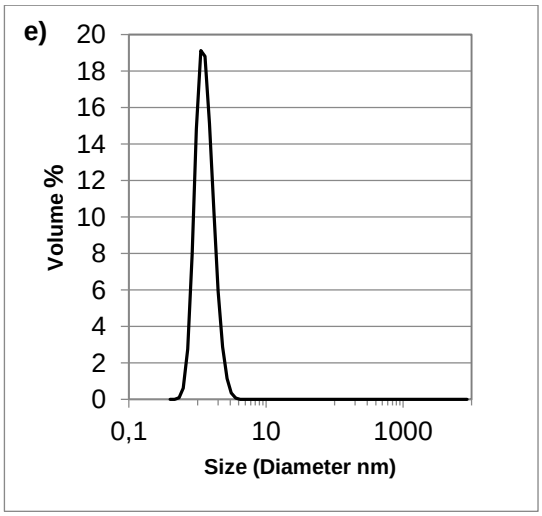

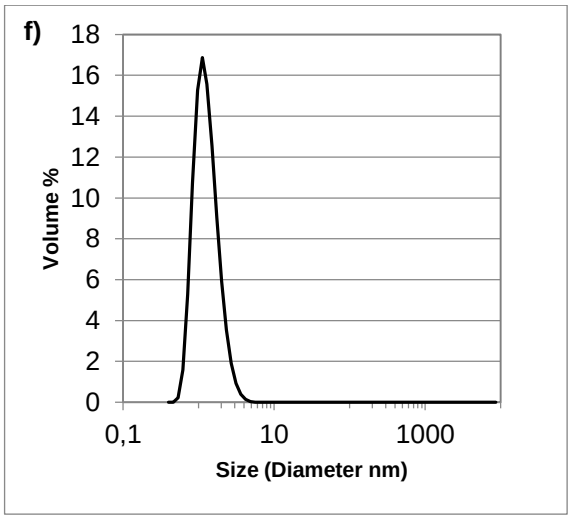

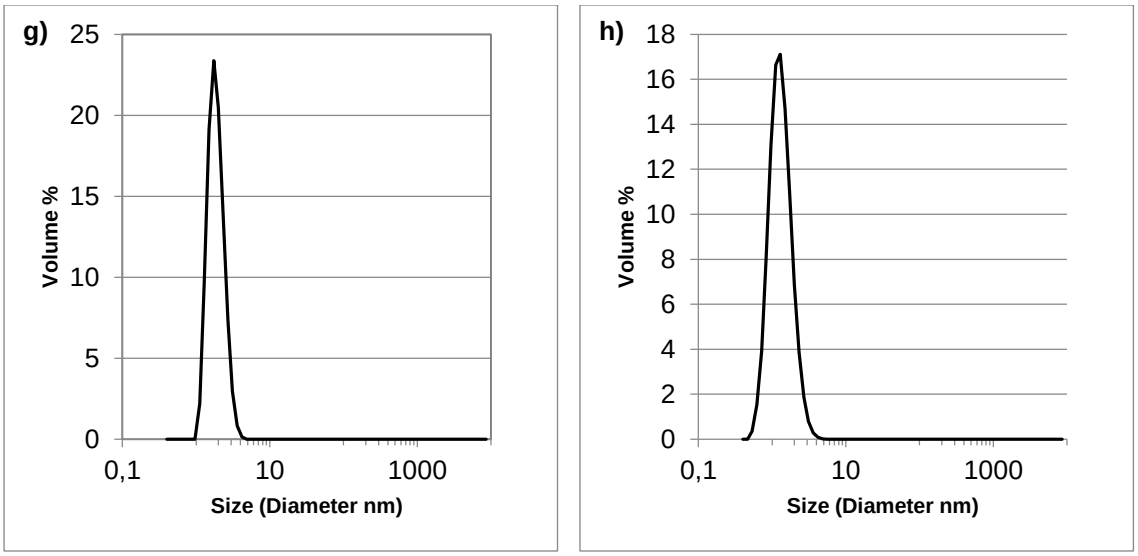

Fig 12. $C_{10}mimNO_3$ with (a) 70mM (b) 119mM (c) 247mM (d) 502mM (e) 744mM (f) 980mM (g) 1257mM (h) 1958mM

3. Aggregate Analysis Graphs

A. C_{10}mimBr+H_2O

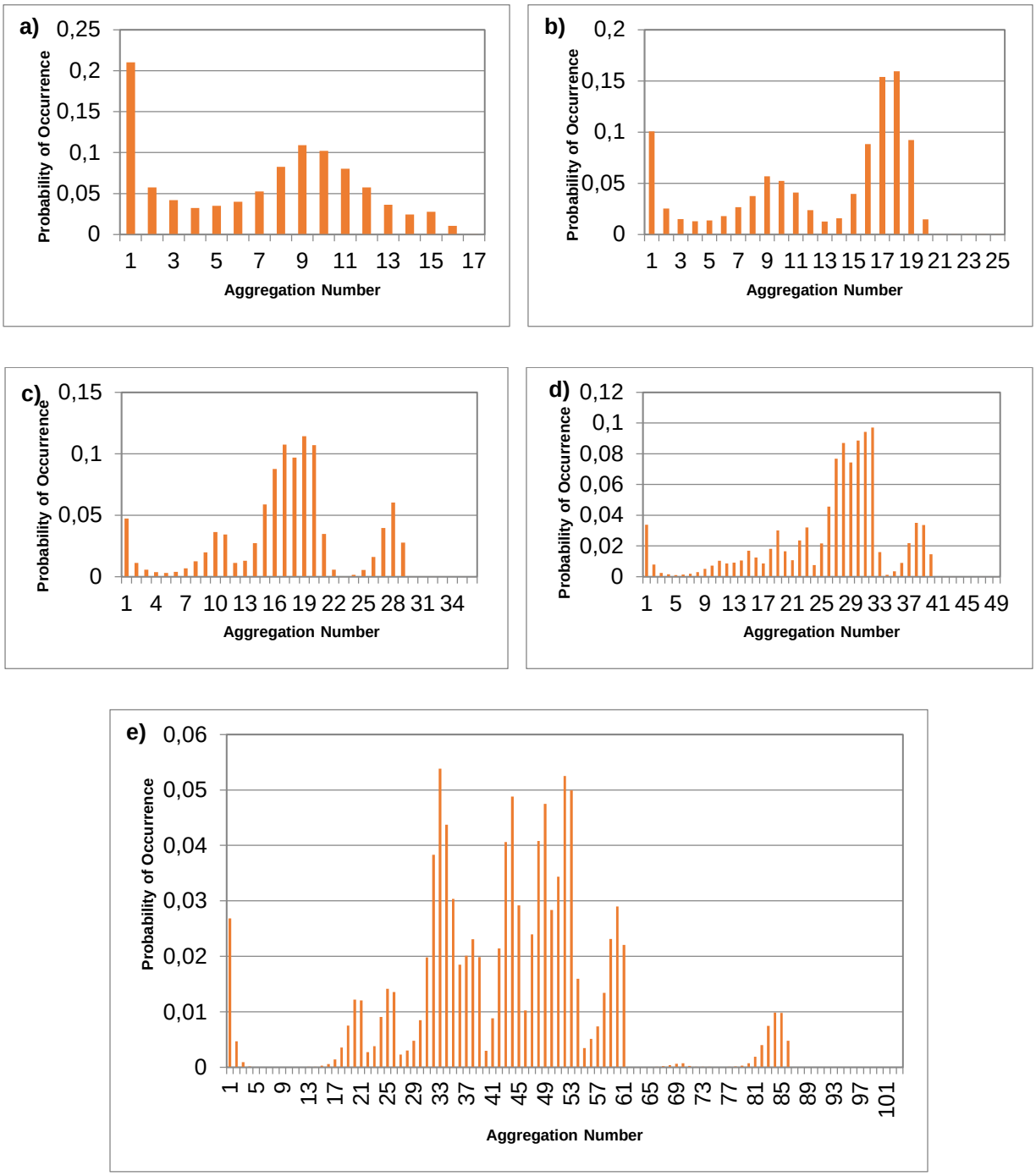

Fig 13: Aggregate analysis of C_{10}mimBr+H2O with all concentrations (a) 0.005, (b) 0.009, (c) 0.018, (d) 0.032, (e) 0.058

B. C_8mimBr+H_2O

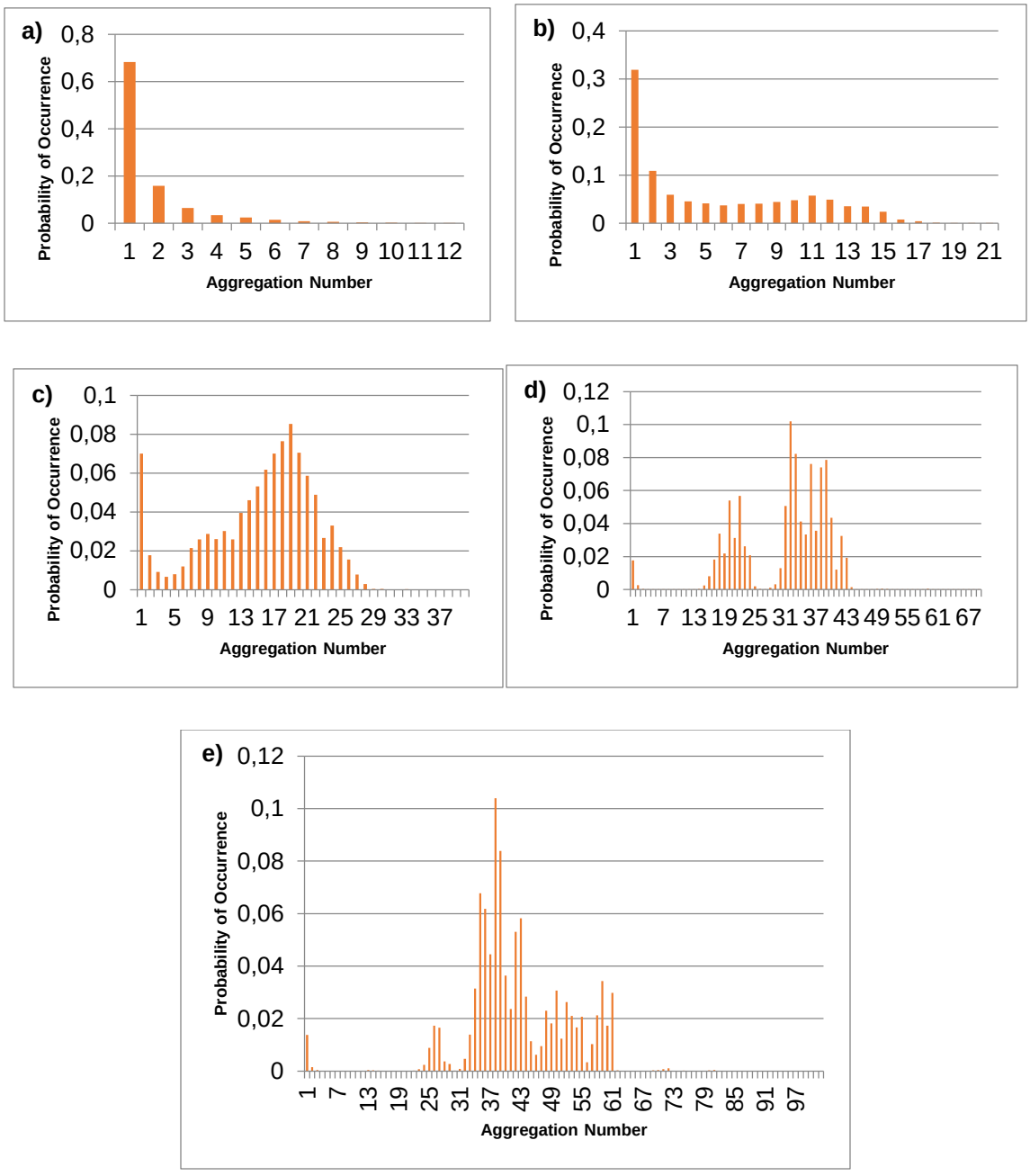

Fig 14: Aggregate analysis of C_8mimBr+H2O with all concentrations (a) 0.0067, (b) 0.012, (c) 0.0296, (d) 0.06, (e) 0.1

4. Tests to Check $C_{10}mimNO_3$ Formation Results

A. 1H Spectra

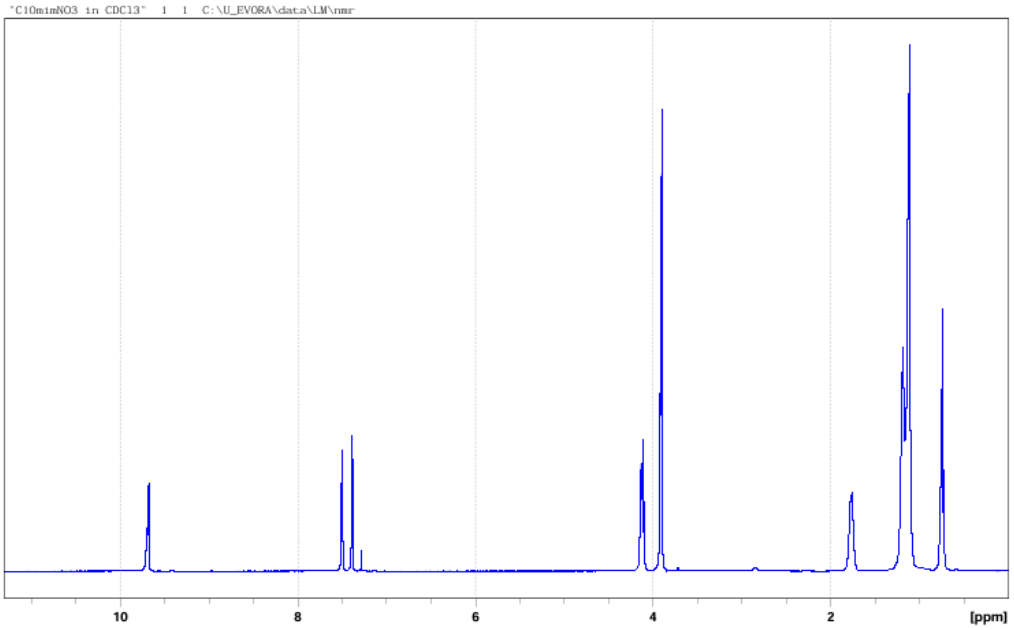

B. 13C Spectra

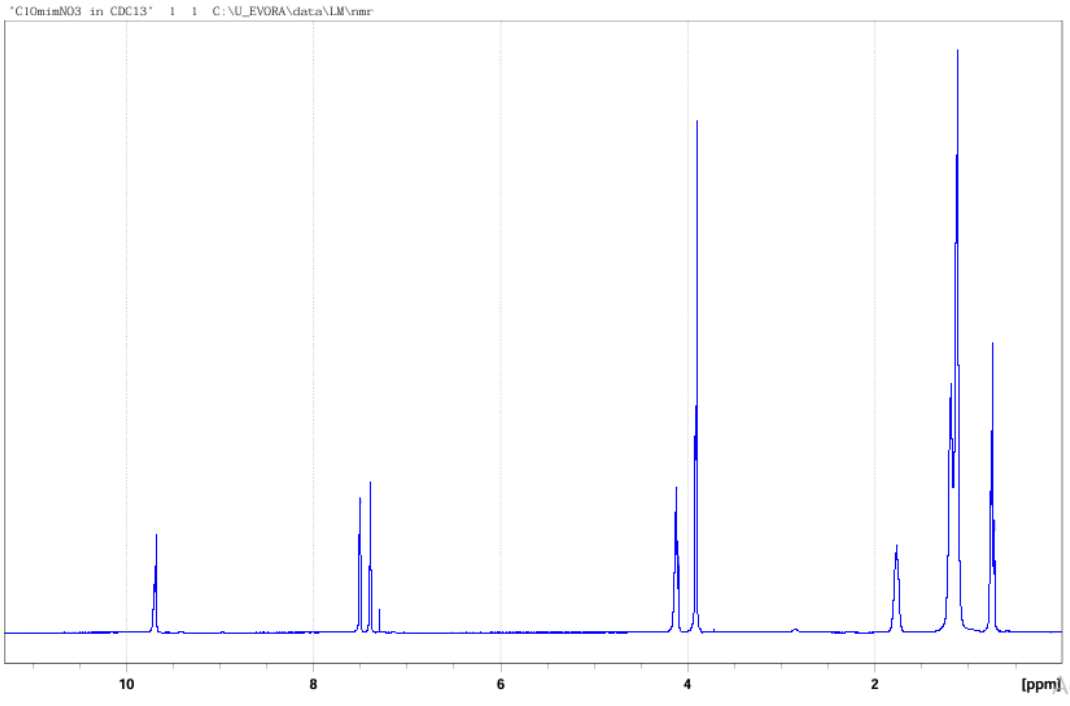

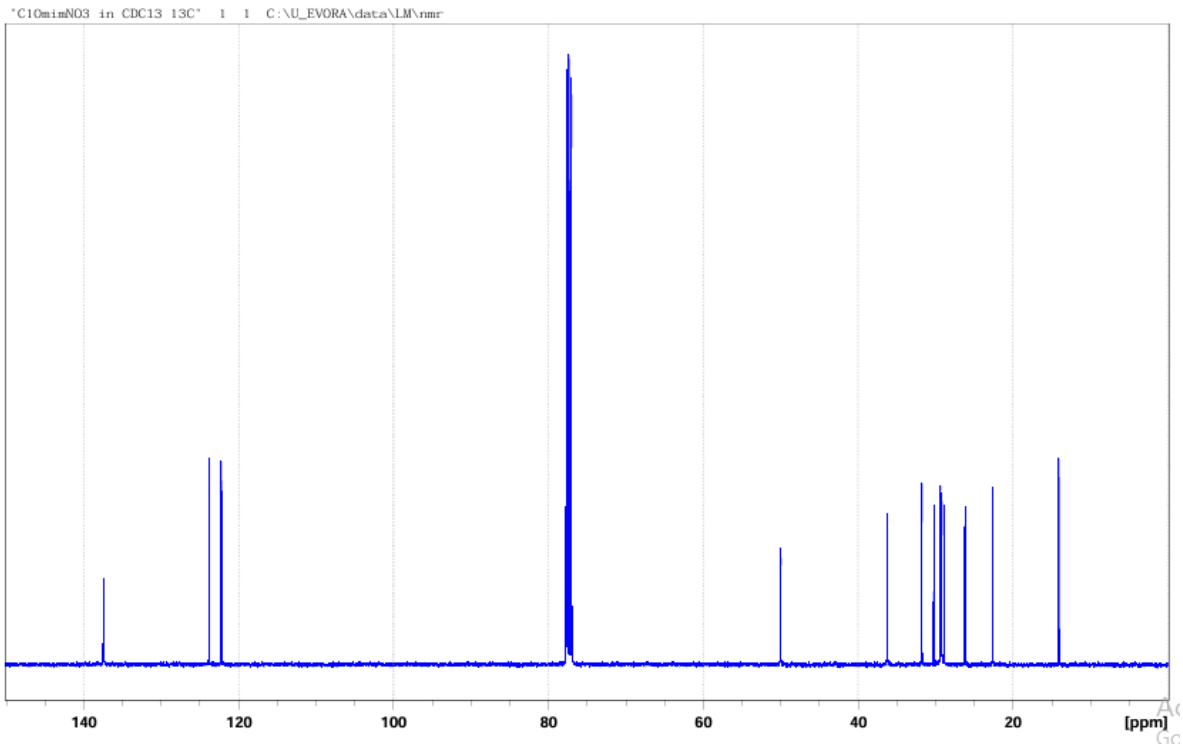
"C10mimNO3 in CDC13 13C" 1 1 C:\U_EVORA\data\LM\nmr
140
120
100
80
60
40
20
[ppm]

C. FTIR

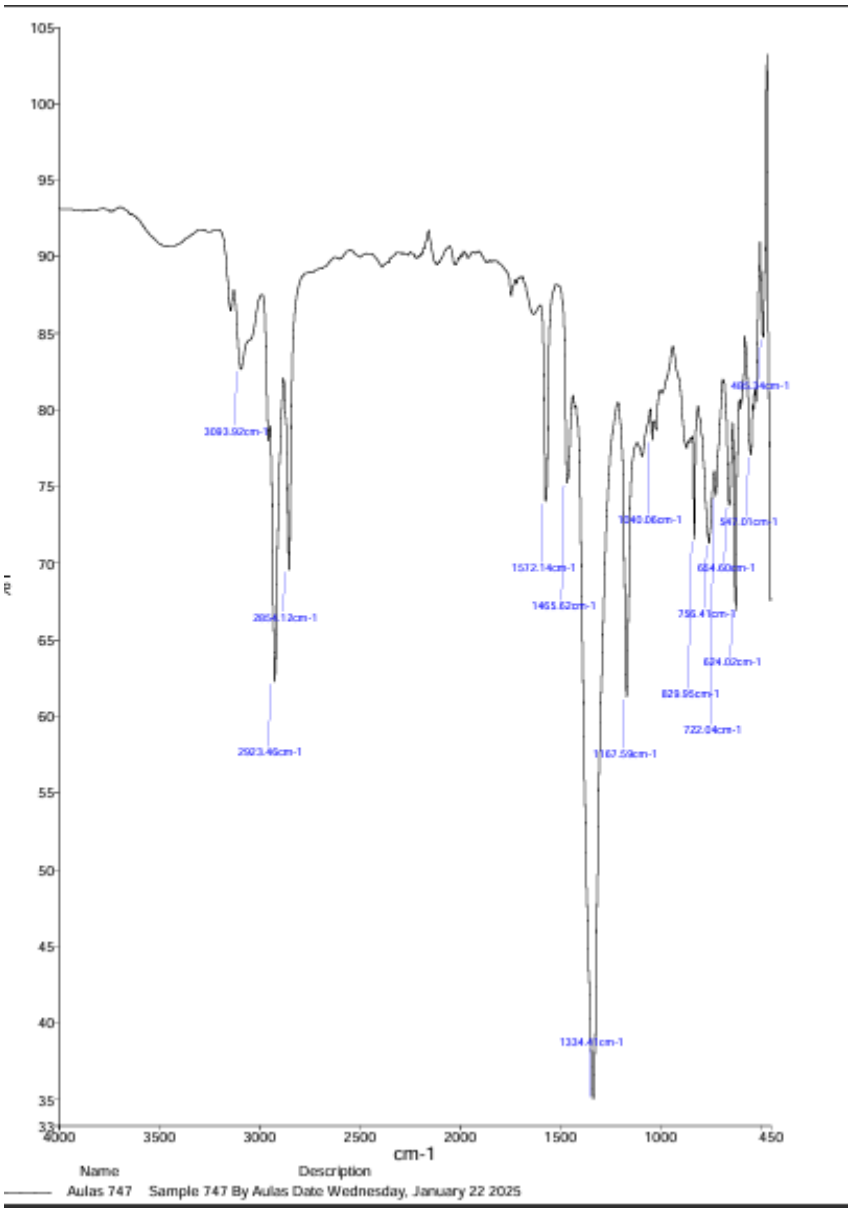
105
100
95
90
85
80
75
70
65
60
55
50
45
40
35
33
4000
3500
3000
2500
2000
1500
1000
450
cm-1
3083.92cm-1
2854.12cm-1
2923.46cm-1
1572.14cm-1
1465.62cm-1
1334.41cm-1
1167.59cm-1
1040.06cm-1
829.95cm-1
722.04cm-1
624.02cm-1
684.60cm-1
Name
Description
Aulas 747
Sample 747 By Aulas Date Wednesday, January 22 2025